NONLINEAR DYNAMICS OF A SPIRAL BEVEL GEAR PAIR

A THESIS SUBMITED TO
THE GRADUATE SCHOOL OF NATURAL AND APPLIED SCIENCES
OF
MIDDLE EAST TECHNICAL UNIVERSITY

BY

BİRKAN ÖNAL

IN PARTIAL FULFILLMENT OF THE REQUIREMENTS
FOR
THE DEGREE OF MASTER OF SCIENCE
IN
MECHANICAL ENGINEERING

JUNE 2018

Approval of the thesis:

NONLINEAR DYNAMICS OF A SPIRAL BEVEL GEAR PAIR

submitted by **Birkan ÖNAL** in partial fulfillment of the requirements for the degree of **Master of Science in Mechanical Engineering Department, Middle East Technical University** by,

Prof. Dr. Halil Kalıpçılar
Dean, Graduate School of **Natural and Applied Sciences** _____

Prof. Dr. M. A. Sahir Arıkan
Head of Department, **Mechanical Engineering** _____

Assoc. Prof. Dr. Ender Ciğeroğlu
Supervisor, **Mechanical Engineering Dept., METU** _____

Assoc. Prof. Dr. Zihni Burçay Sarıbay
Co-Supervisor, **MGAT Lab.** _____

Examining Committee Members:

Asst. Prof. Dr. M. Bülent Özer
Mechanical Engineering Dept., METU _____

Assoc. Prof. Dr. Ender Ciğeroğlu
Mechanical Engineering Dept., METU _____

Asst. Prof. Dr. Gökhan Özgen
Mechanical Engineering Dept., METU _____

Prof. Dr. F. Suat Kadıoğlu
Mechanical Engineering Dept., METU _____

Asst. Prof. Dr. Can Ulaş Doğruer
Mechanical Engineering Dept., Hacettepe University _____

Date: _____

I hereby declare that all information in this document has been obtained and presented in accordance with academic rules and ethical conduct. I also declare that, as required by these rules and conduct, I have fully cited and referenced all material and results that are not original to this work.

Name, Last name : Birkan ÖNAL

Signature :

ABSTRACT

NONLINEAR DYNAMICS OF SPIRAL BEVEL GEAR PAIR

Önal, Birkan
M.S., Department of Mechanical Engineering
Supervisor: Assoc. Prof. Dr. Ender Ciğeroğlu
Co-Supervisor: Assoc. Prof. Dr. Zihni Burçay Sarıbay
June 2018, 96 pages

Nonlinear dynamics of a generic spiral bevel gear pair used in high speed, high power gearboxes is studied in this thesis. Different tooth ease-off topographies are generated based on real machine settings. Tooth micro geometries are established in order to obtain profile crowning, lengthwise crowning and flank twist topographies. Details of macro and micro geometry and corresponding real machine settings are given in this study. Path of contact, contact stress, directional rotation radius, load share, unloaded and loaded static translational transmission error, and mesh stiffness are presented for drive and coast sides of gear tooth. Loaded analyses are conducted at 100Nm, 200Nm and 400Nm torque loads. These ease-off topographies are compared for many advantages on the stability of path of contact, lowest contact stress, lowest unloaded and loaded transmission errors, and highest mesh stiffness. The accumulated results are used in nonlinear dynamic analysis of a spiral bevel gear pair. Dynamic model includes gear backlash in the form of clearance-type displacement function, time variation of mesh parameters, which are gear mesh stiffness, directional rotation radius and mesh damping. The mesh parameters are also asymmetric due to difference between drive and coast sides of gear tooth. The

system is reduced to a single-degree-of-freedom definite model by using the relative gear mesh displacement as the generalized coordinate. The equation of motion is solved for periodic steady-state response by using Harmonic Balance Method. A set of parametric studies are performed to determine the effects of different tooth flank modifications on dynamic response of a helicopter transmission drive system.

Keywords: Static transmission error, real machine settings, time-varying mesh stiffness, flank twist, profile crowning, lengthwise crowning, nonlinear gear dynamics, gear backlash nonlinearity, multi-term Harmonic Balance Method,

ÖZ

SPİRAL BİR KONİK DİŞLİ ÇİFTİNİN DOĞRUSAL OLMAYAN DİNAMİĞİ

Önal, Birkan
M.S., Makina Mühendisliği Bölümü
Tez Yöneticisi: Doç. Dr. Ender Ciğeroğlu
Ortak Tez Yöneticisi: Doç. Dr. Zihni Burçay Sarıbay
Haziran 2018, 96 sayfa

Bu tezde, yüksek hızlı ve güçlü dişli kutularında kullanılan genel bir spiral konik dişli çiftinin doğrusal olmayan dinamiği çalışılmıştır. Gerçek makina ayarlarına dayanan farklı diş topografyaları oluşturulmuştur. Profil yönünde bombeyi, diş boyunca bombeyi ve yanak kıvrımını elde edebilmek için diş mikro geometrileri oluşturulmuştur. Bu çalışmada, makro ve mikro geometri ve onlarla ilgili gerçek makina ayarları verilmiştir. Dişlerin çalışan ve çalışmayan tarafları için bası izleri, bası gerilmesi, yönlü dönme yarıçapı, yük paylaşımı, yüksüz ve yüklü statik ötelenen aktarım hatası ve kavrama sıkılığı sunulmuştur. Yük analizleri 100 Nm, 200 Nm ve 400 Nm tork yüklerinde yapılmıştır. Diş topografyaları kararlı bası izleri, en düşük bası gerilmeleri, en düşük yüksüz ve yüklü aktarım hataları ve en yüksek kavrama sıkılığı gibi birçok avantaj için karşılaştırılmıştır. Toplanan sonuçlar bir spiral konik dişli çiftinin doğrusal olmayan dinamik analizinde kullanılmıştır. Dinamik model aralık tipi deplasman fonksiyonu formunda diş boşluğu, dişli kavrama sıkılığı, yönlü dönme yarıçapı ve kavrama sönümü gibi kavrama parametrelerin zamanla değişimini içermektedir. Bu kavrama parametreleri dişin

çalışan ve çalışmayan tarafları arasındaki fark yüzünden aynı zamanda asimetriktir. Sistem, bağıl dişli kavrama deplasmanını genelleştirilmiş koordinat gibi kullanarak tek derece serbest belirli modele indirgenmiştir. Hareket denklemi, Harmonik Denge Yöntemi kullanarak periyodik kararlı durum tepkisi için çözülmüştür. Farklı diş yanak modifikasyonlarının helikopter güç aktarım sisteminin dinamik tepkisi üzerindeki etkilerini belirlemek için parametrik çalışmalar gerçekleştirilmiştir.

Anahtar Kelimeler: Statik aktarım hatası, gerçek makina ayarları, zamanla değişen kavrama sıkılığı, yanak kıvrımı, profil yönünde bombe, dişli boyunca bombe, doğrusal olmayan dişli dinamiği, doğrusal olmayan dişli boşluğu, çok harmonikli Harmonik Denge Yöntemi,

ACKNOWLEDGEMENTS

I would like to thank my supervisor Assoc. Prof. Dr. Ender Ciğeroğlu and my co-supervisor Assoc. Prof. Dr. Zihni Burçay Sarıbay for their supervision, help and guidance from the beginning to end of this dissertation.

I want to thank my colleague and friend Dr. Şiar Deniz Yavuz for her endless support and encouragement throughout this study.

I would like to express my thanks to my family for their patience when I was studying instead of having time with together.

TABLE OF CONTENTS

LIST OF TABLES

TABLES

LIST OF FIGURES

FIGURES

LIST OF SYMBOLS

b	half of gear backlash
c	mesh damping coefficient
e	static transmission error
f	nonlinear displacement function
J	Jacobian matrix
n_l	line of action (LOA) directional cosine vector
r_l	position vector of the effective mesh point
r	harmonic index
S	nonlinear algebraic equations in vector form
T_p, T_g	Pinion & gear torque
t	time
x	displacement vector
δ	dynamic transmission error
λ_l	directional rotational radius
m_e	equivalent mass
h	discrete time interval
θ	rotational displacement
ω	frequency
FT	flank twist
LW	lengthwise
PF	profile

Subscripts

l	pinion $l = p$ and gear $l = g$
m	pinion $m = d$ and gear $m = c$

Superscripts

$\dot{}$	derivative with respect time
$'$	derivative with respect dimensionless time
$\sim$	dimensionless quantities

CHAPTER 1

INTRODUCTION

1.1 Introduction

In aerospace applications, bevel gears transmit motion and power from one shaft to another intersecting shaft. Straight, spiral bevel and hypoid gears are the three main types and the spiral bevel gears are the ones widely used in helicopter transmission drive system. Straight bevel gears are the simplest and oldest type and their teeth are straight and tapered. The relationship between spiral and straight bevel gears is analogous to that between helical and spur gears. Therefore, Fig. 1.1 illustrates a spiral bevel gear would be obtained by adding infinite numbers of short-face sections of straight bevel gear and each of these sections displaced angularly relative to another.

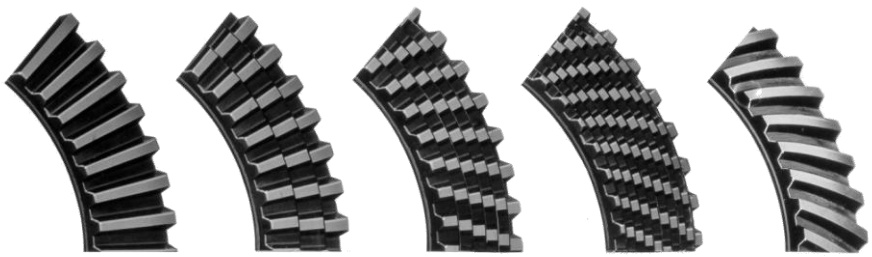

Fig. 1.1 Straight to spiral bevel gear pair [1]

The teeth of bevel gears are located on a surface of cone and lengthwise shaped is curved and oblique to this cone, see Fig. 1.2. Well-designed spiral bevel gears have considerable reasons why they are superseding other bevel gear types in many areas.

Fig. 1.2 Spiral bevel gear pair [1]

There are some design considerations of spiral bevel gears used in helicopter transmission drive system in terms of reduction ratio and speed, load carrying capacity, noise and vibration level and some special operating conditions. The ratio of bevel gear pairs is generally between 1 and 8. Spiral bevel gears without grinding works with peripheral speeds up to 8000 ft/min. If peripheral speeds in excess of 8000 ft/min, ground teeth of gears (precision finished gear) are used up to 25000 ft/min. Load carrying capacity of spiral bevel gears is relatively larger than that of other bevel gear types, because; tooth loads are more evenly distributed thanks to that two or more teeth are in contact during operation. In order to have less noise and vibration, this high contact ratio and ground teeth of gears make teeth mesh smoother and quieter. Any special or adverse operating condition such as high ambient temperature, presence of corrosive elements and inadequate lubrication and cooling are to be compensated.

Therefore, all failure modes are to be known in details to have a well-design of a spiral bevel gears for a helicopter gearbox. For the strength analysis of a gear-pair, the following failure modes as shown in Fig. 1.3 are taken into account;

- tooth breakage (due to bending),
- Surface pitting (due to contact),

- Wear (due to insufficient lubrication),
- Scuffing (due to high temperature of the lubricant).

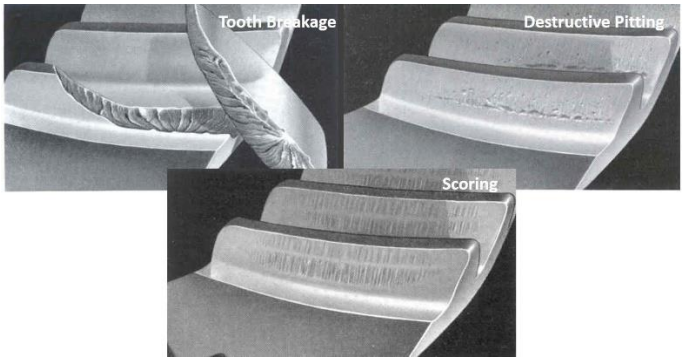

Fig. 1.3 Failure modes[1]

For these failure modes,

- Bending stress at the root fillet area of the tooth is calculated.
- Contact stress at the tooth surface, where the conjugate action takes place at any instant of time, is calculated.
- The elastohydrodynamic lubrication (EHL) film thickness is estimated and compared to the surface roughness.
- Critical temperature in a pair of bevel gear is analyzed.

A gear and pinion roll through mesh, strain values in the fillets of the gear and pinion teeth vary in magnitude from compressive to tensile strains. The determination of the maximum values of strain is also complicated by the fact that the location of maximum strain varies both along the face-width direction of the tooth and in the profile direction perpendicular to the root of the tooth. These strain values gives the fillet stress distribution, which represent the maximum value of principal stress occurring in the fillet area and are most useful for obtaining a general understanding of where the peak stresses occur in the gear and pinion fillet areas as shown in Fig. 1.4. It is possible to use this location information to redevelop the gear design to achieve lower bending stresses.

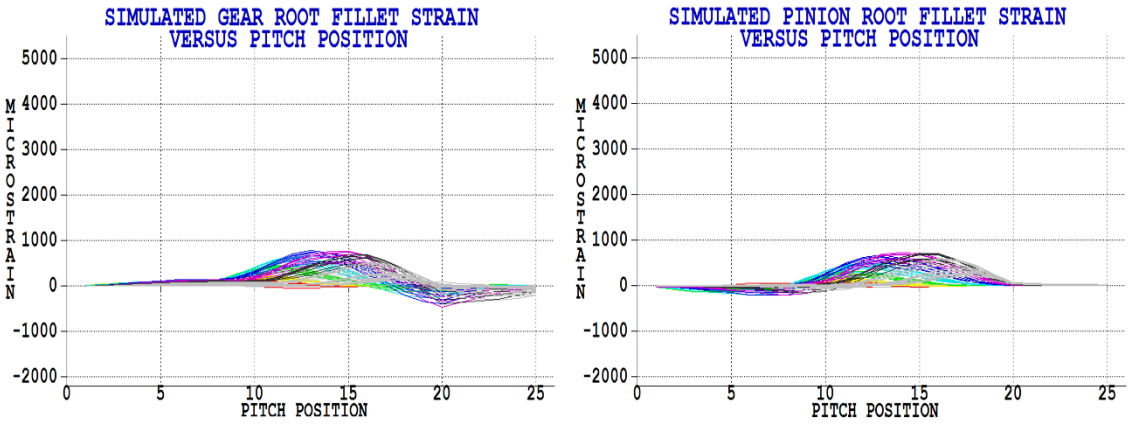

Fig. 1.4 Maximum fillet stress range

A commercial tool with finite element analysis in conjunction with bevel gear contact development in Fig. 1.5 gives the actual calculated contact stress of gear surface and also analyzes the pitting failure.

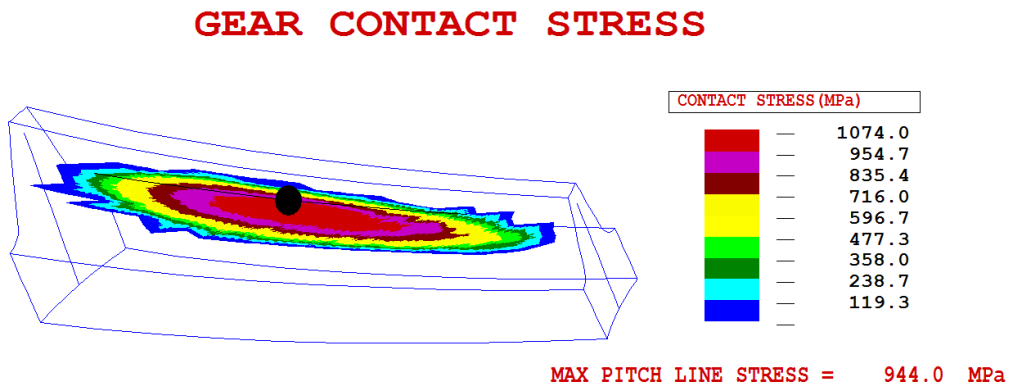

Fig. 1.5 Bevel gear contact stress

Location of high contact pressure determines the failure type. Along the pitch line of the gear, high contact pressure indicates the possibility of pitting while along the tip of the gear resulting in high wear in the flank area of the mating pinion.

Scoring is considered to be a rapid wearing away of the tooth surfaces due to heat generated by pressure and sliding of the tooth surfaces. Scuffing is a welding and

subsequent tearing apart of the tooth surfaces due to a breakdown of the oil film. As shown in Fig. 1.6, gear pair contact zone temperature increases due to combination of sliding friction and surface pressure then breakdown the oil film, which resulting in micro welding of asperities. Therefore, hot scuffing occurs typically within minutes in the direction of sliding velocity.

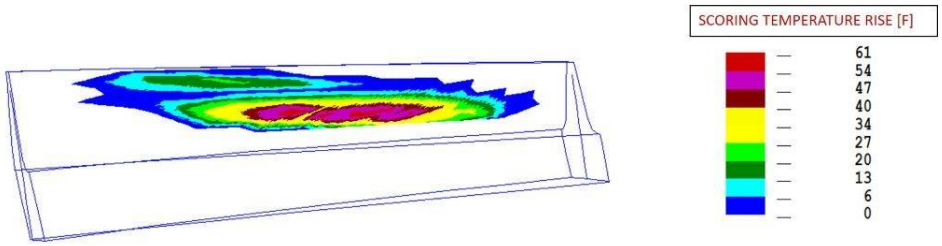

Fig. 1.6 Scoring temperature rise

The main goal in the design of these drive systems is to achieve accurate predictions of contact and bending stresses in order to have longer service lives with lighter gears and to minimize flash temperature. However, these predictions change under dynamic loadings which result in much higher stresses. In addition to that, noise and vibration are not still easy to predict. Therefore, in practice spiral bevel gear pairs go through a series of tests to finalize the system design. As a result, gear dynamics play a key role in finalizing design of spiral bevel gear pairs, because of the complex nature of the spiral bevel gear tooth, its sensitivity to manufacturing and assembly errors that contribute to nonlinear dynamic nature of the gear trains.

1.2 Literature Survey

For the strength analysis of a gear-pair, failure modes such as tooth breakage, surface pitting and scoring are taken into account. The methods established in the gear standards such as AGMA [2] are good starting points for the design process.

However, even if the spiral bevel gears are manufactured according to the required quality assembly and operational conditions affect the meshing performance of the spiral bevel gears. Hence, spiral bevel gears are manufactured with tooth micro modifications for best performance and strength.

The methods of spiral bevel gear tooth micro geometry development start with the proper identification of the gear macro geometry according to the system design requirements. Hence, gear blank data based on standards, gear cutter specifications, gear machine tool settings, pinion machine tool settings and desired objective transmission function are used as inputs to the gear modeling. The outputs are the tooth and root forms of the crown, gear and pinion tooth contact path and pattern for unloaded and loaded cases, transmission error in to produce the desired tooth form. The process is typically iterative until the desired contact and transmission error are established without sacrificing the design performance, strength, durability and cost requirements. The tooth contact patterns and transmission errors are calculated using the differential geometry and Hertzian contact theory in [3] and [4], while using FEA in [5], [6] and [7].

In [8], authors presents so called ultimate motion graph method to reduce the noise, improve the sensitivity of gears against deflection under load and no-load conditions while increasing the strength levels of face milled spiral bevel gears by using universal motion concept (UMC) free form bevel gear grinding machines. Advantages and manufacturability of the tooth crowning from very practical perspective are presented. The UMC method is applied to sample automotive bevel gear that are manufactured with different ease-off topographies. The success of the manufacturing is proven by measurements and with the support of acoustic tests on contact tester and actual operation of the selected spiral bevel gears. One of the earlier examples of the simulation of the hypoid and spiral bevel gear cutting with the mathematical tools that models the universal motion generator is shown in [9]. Modified generating roll ratio, helical motion, and cutter tilt are included in this

mathematical model. The relevant coordinate transformation matrices are established and explained clearly with figures. As a follow-up work in [10], a methodology to model the mating tooth surfaces with UMC characteristics is presented to calculate machine settings for the modified radial motion which leads the generation of the contact path and fourth-order motion curve.

Furthermore, authors present an accurate modeling method for generation of the face-milled and face-hobbed spiral bevel gears with free form gear machining with universal motion concept in [11], [12] and [13]. A corrective machine setting technique is developed to modify the theoretical machine tool settings to compensate for the surface errors in a simulation of machining environment. Additionally, in [14] and [15], authors are dealing with the elimination of this iterative design process to find the optimal solution by specifying an ease-off topography that defines an optimum contact pattern from which the machine tool settings are calculated to satisfy the design requirement. Here, unconstraint nonlinear optimization problem is formulated and solved. Similarly, in [16] and [17] methods to optimize the ease-off topography are presented for hypoid gears that reduces the trial and errors in the design of tooth contact and loaded transmission error. One of the conclusions of this work is that the level of accuracy needed to practically realize the optimum ease-off topography is high; hence, the grinding method is needed to produce required micro geometry. The example parametric effects on kinematical errors are presented for different machine settings data. The theoretical development of the tooth micro geometry is also included the flank form errors and their effect on the universal motion concept coefficients in practical applications as shown in [18] and [19] where the higher order coefficients are considered. Further improvements are demonstrated in [20] and [21]. The influence of tooth modifications contact characteristics in face-hobbed spiral bevel gears is investigated in [22] while observing machine tool setting and head-cutter profile variations. This is extended in [23] to investigate the elastohydrodynamic lubrication characteristics of the spiral bevel gears with different tooth micro

geometries and to evaluate the effects of different machine settings used to produce the pinion.

The most of the literature summarized above mainly concentrates on the accurate modeling of the tooth form based on the manufacturability and the ease-off characteristics of the bevel gears that produces the optimal contact area and transmission error. Also, in addition to the optimum contact pattern to avoid edge contact for the meshing teeth, the dynamic mesh loading, and system dynamic behavior and response are crucial elements of the bevel gear drive trains. One of the most critical elements of the gear dynamics is the mesh stiffness. However, gear mesh stiffness relevant to dynamic analysis is not commonly found in the literature. The beam theory is used in [4] for the estimation of the tooth stiffness. In [24], finite strip method is presented as a method to calculate the tooth stiffness. The effect of torque change in a specified bevel gear tooth with correct machine settings are presented in [25]. Here, the mesh stiffness is obtained by FEA based bending and surface integral based contact model. Here, a quasi-static loaded tooth contact analysis at one pitch cycle in discrete steps of angular mesh point positions is performed to calculate stiffness, transmission error, and load distributions as shown in Fig. 1.7.

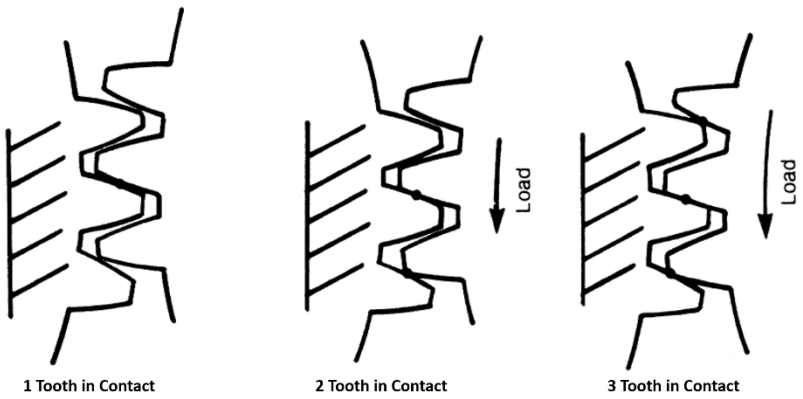

Fig. 1.7 Load distribution scheme [4].

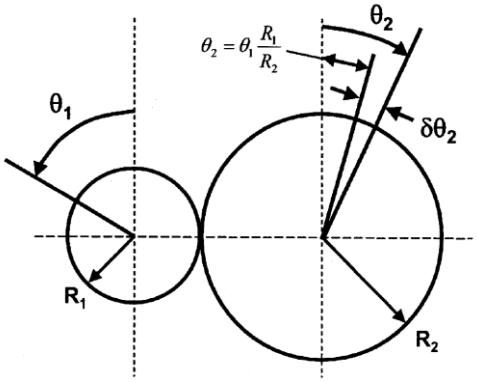

Fig. 1.8 Definition of motion error

The difference between the actual position of the output gear and the position it would occupy if the gear drive is perfectly conjugate. As shown in Fig. 1.8, θ_1 is both theoretical and actual angular position for input pinion. However, θ_2 is theoretical angular position for output gear; while, $\theta_2 + \delta\theta_2$ is actual angular position for output gear.

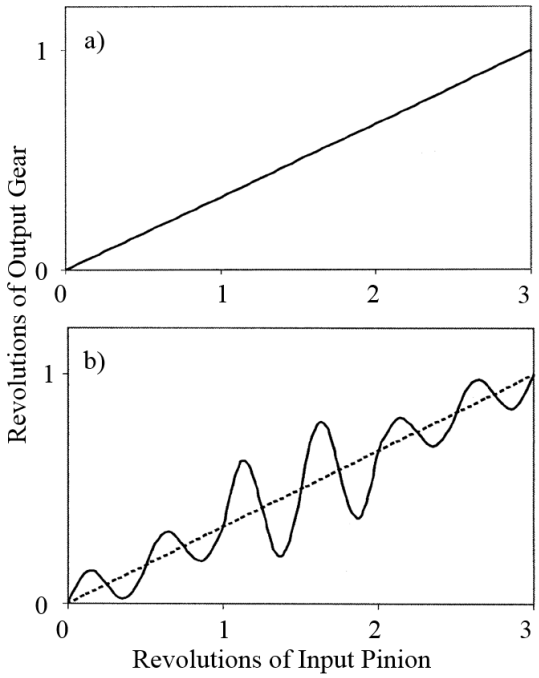

Fig. 1.9 Gear pairs with and without transmission error

Fig. 1.9 -a) shows perfect conjugate action; so, there is no transmission error. Input pinion and output gear rotate with ratio 3 continuously. On the other hand, ratio 3 fluctuates for gear pair due to transmission error as shown in Fig. 1.9 b).

In gear dynamics, there are relatively few publications studying the dynamics of spiral bevel gear pairs compared with the parallel axis gear pairs Dynamics of a hypoid gear pair model is proposed by considering the effects of time-varying mesh parameters and backlash nonlinearity in [26]. Effects of tooth mesh stiffness asymmetric nonlinearity for drive and coast sides are investigated in [27]. Dynamics of right angle gear pair including both backlash and asymmetric mesh stiffness nonlinearities with time varying and asymmetric mesh parameters is formulated in [28]. A MDOF nonlinear dynamic model of a spiral bevel gear pair mounted on flexible shafts and bearings is considered in [29]. Then, the authors extend this study to include time variation of mesh stiffness and employ receptance method in order to decrease computational time in [30]. These are the content of current literature in dynamic studies of spiral bevel gear pair. In these previous works, many assumptions and simplifications are done to reduce the complex temporal and spatial varying mesh characteristic, the coupling effect between nonlinear gear mesh and some effects that need further considerations.

1.3 Motivation, Objective and Scope

In the light of the summarized literature, it is certain that the machine settings and cutter specifications substantially determine the conditions of meshing and contact of the spiral bevel gears. There are mathematical models for the tooth surface generation according to the bevel gear type and the machining methods. Once the surface generation is completed, the process continues as unloaded and loaded tooth contact analysis, load distribution, transmission error and optimization of the machine settings for a good contact pattern and minimum transmission error. While

the presented literatures are very effective in developing tools on quasi-static analysis of contact pattern and stress a necessity of understanding for the modifications that affect the dynamic characteristics exist. One of the most significant parameters in spiral bevel gear dynamics is the modeling the mesh stiffness. However, mesh model coupled with the macro and micro geometry along with mesh stiffness and static transmission error calculation according to the actual tooth geometry is not common in literature. Especially, the effect of the ease-off topography on the mesh stiffness, that is adaptable to dynamic analyses, is not documented in the current literature. Hence, gear mesh of a spiral bevel gear pair with different micro geometries based on real machine settings is evaluated in this study to prepare a foundation to dynamic analysis of the spiral bevel gears. Different micro geometries are given in order to obtain three main tooth flank modifications (profile crowning, lengthwise crowning and flank twist) of spiral bevel gear teeth.

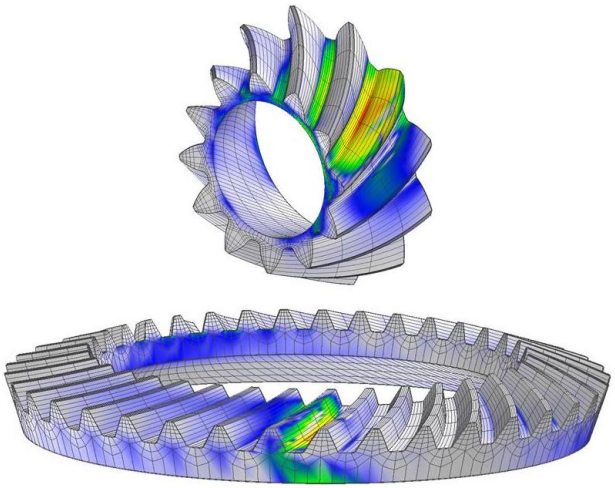

Fig. 1.10 Calyx FEA gear pair model [32]

Therefore, the main objective of this study is to perform nonlinear dynamic analysis of a spiral bevel gear pair used in the helicopter gearboxes with different tooth flank modifications such as profile crowning, lead crowning and flank twist.
In this thesis, the following tasks are needed.

- Actual tooth geometry with these flank modifications and its corresponding real machine settings produced by Gleason CAGE4WIN™ software will be synthesized for load distribution results of a three-dimensional loaded tooth contact analysis with a combined surface integration according to the guidance in [31].
- According to the actual tooth geometry, a mesh model to represent the dynamic coupling between engaging gear pair will be extracted from Calyx software [32] as shown in Fig. 1.10.
- Viscous damping assumption is used to model energy dissipation due to all sorts of damping.
- The spiral bevel gear pair with backlash nonlinearity as well as asymmetric and time-varying mesh coupling model will be proposed. Multi-term HBM coupled with discrete Fourier transform (DFT) and numerical continuation will be applied to solve nonlinear algebraic equations for dynamic displacements in torsional mode.
- Perform detailed comparative study for certain effects of tooth flank modifications on dynamic response under light, medium and high loads and to identify sensitivity of dynamic response with static transmission error and mesh stiffness of actual tooth having different flank modifications.

1.4 Organization

In this study, introduction including literature survey, motivation, objective and scope are presented as a Chapter 1. In Chapter 2, a selected pair of spiral bevel gears with numbers of teeth 23 and 47 is designed in terms of macro and micro geometry. The details of the macro geometry are given. The micro geometry with real machine settings are produced by Gleason CAGE software. In the next step, parameters such as mesh stiffness and static transmission error to model gear mesh coupling are

obtained by Calyx software. Mesh stiffness is load dependent and variation of tooth mesh stiffness for drive and coast sides are considered. In Chapter 3, a dynamic model including backlash nonlinearity and nonlinear time-varying mesh parameters is formulated for spiral bevel gear pairs with tooth flank modifications. The system is reduced to a single-degree-of-freedom definite model by using the relative gear mesh displacement as the generalized coordinate. The equation of motion is solved for periodic steady-state response by using Harmonic Balance Method (HBM) with discrete Fourier transform. Floquet theory is applied to determine the stability of the steady-state solution. Nonlinear dynamic responses of spiral bevel gear pairs with different motion error and stiffness are discussed and this gives designers a chance in order to understand how much these flank modifications affect dynamic response of gear pair before finalizing their design. Finally Chapter 4 gives the general summary and conclusions of this study.

CHAPTER 2

ACTUAL TOOTH DATA AND GEAR MESH MODEL

2.1 Actual Tooth Data

2.1.1 Manufacturing Method

Designing a spiral bevel gear pair for helicopter transmission drive systems requires a tooth geometry produced by special settings and cutting processes which are based on two motions, generation and single indexing. Concept of bevel gear generation is that mating gear and pinion are considered to be generated by complementary virtual generating gears that are conjugate to each other simultaneously. The rotational motion of the virtual generating gear is implemented by cradle mechanism of a bevel gear generator, which is schematically shown in Fig. 2.1. In other words, tooth shape is generated by a relative roll between the cutting tool and workpiece. If there is no relative motion, gear teeth profile is the inverse of the cutter profile. That is, cradle angle is not changing, so; gear is not generated. In all cases, pinion member of pairs is generated in order to give micro modifications on pinion tooth surface. Therefore, making a bevel gear pair generated depends on whether gear member of pairs is generated or non-generated. The shape of the cutting tool does not determine the final shape of the "Generated" tooth surface. Ratio of the generated roll determines the final shape of tooth [18].

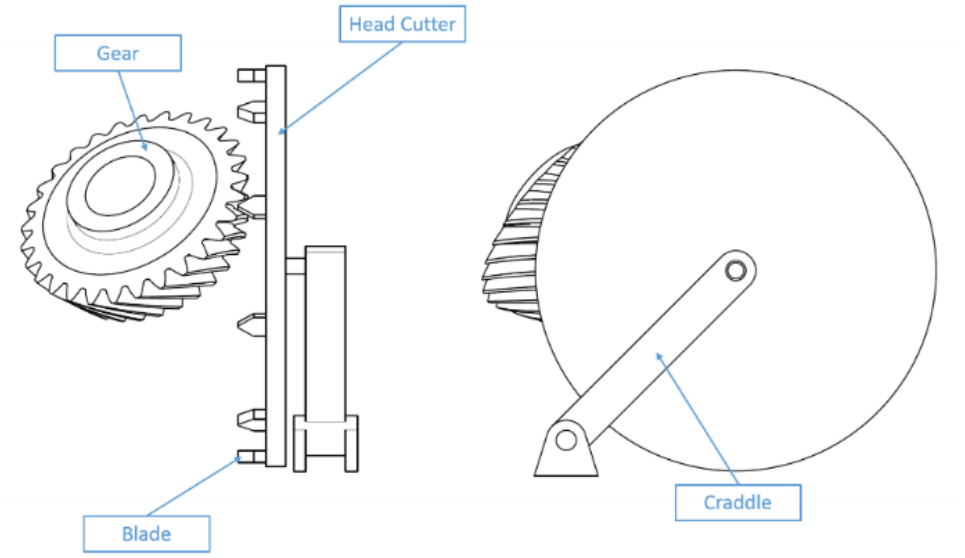

Fig. 2.1 Schematic of generation of a spiral bevel gear

Single indexing, face milling is intermittently provided by rotating the workpiece after finishing a tooth space or one slot at a time. On the other hand, in continuous indexing, face hobbing, the work has continuous rotation and the cutter rotates in a timed relationship with successive cutter blade groups engaging successive tooth slots as the gear is being cut. Fig. 2.2 shows that face milling is more suitable process for grinding of tooth as finishing operation because of the fact that mathematical function of generating gear flank is circular not epicycloid as in the case of face hobbing process.

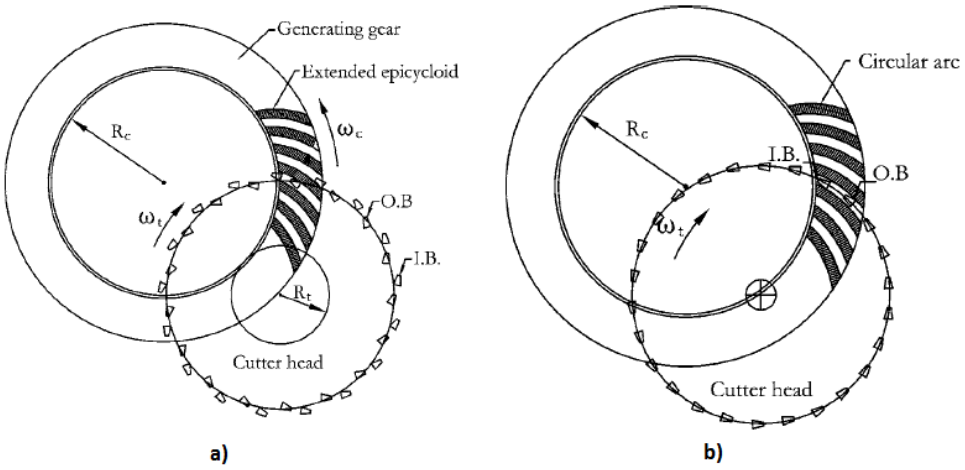

Fig. 2.2 a) Face hobbing process (Continuous indexing) vs. **b)** Face milling process (Single indexing) [12]

Therefore, generation process and face milling are used for applications like helicopter gearboxes where greatest control of tooth contact pattern and surface finish are demanded. Besides to generation process and face milling, pinion's concave and convex side are cut separately for ultimate control of machine settings. By using face milling and generation process, a spiral bevel gear pair is designed in terms of macro geometry as shown in Fig. 2.3 the details of which are given in following equations.

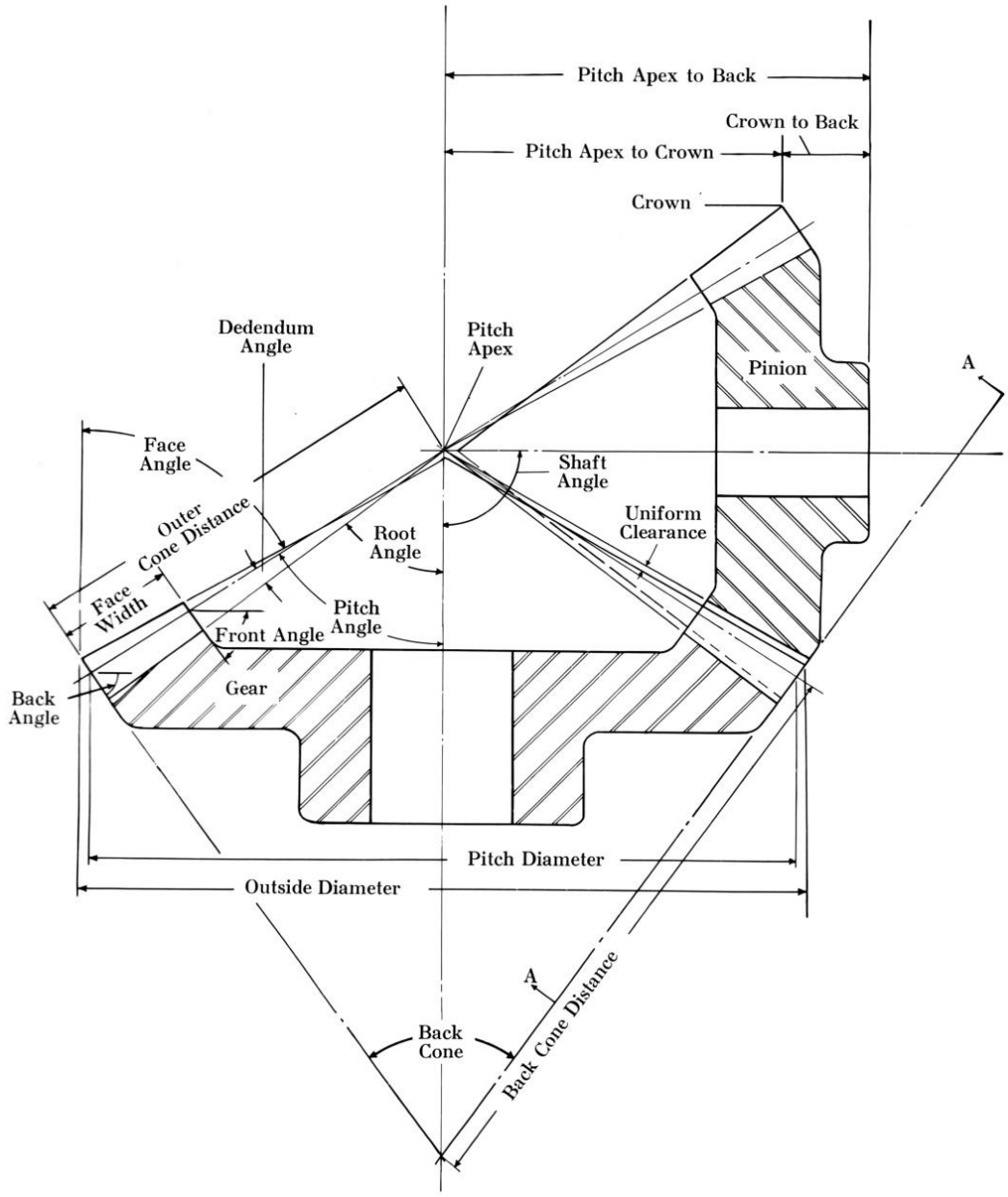

Fig. 2.3 Nomenclature of a spiral bevel gear [1]

2.1.2 Macro Geometry

The selected gear pair macro geometries are designed and corresponding equations are calculated according to the rules and guidelines presented in [2] and [31]. The specific use of the selected example pair is for high speed, high loaded aerospace applications where the gear strength, mesh efficiency, roller bearing endurance are required to be highest while the overall system vibration is minimum. For the generation of macro-geometry of a spiral bevel gear, the parameters tabulated at Table 2.1 are the main design inputs [2]:

- Numbers of teeth, n_j,
- Outer pitch diameter of any member, d_1 or d_2,
- Shaft angle, Σ,
- Face width, F,
- Mean spiral angle, ψ_m,
- Normal pressure angle, ϕ^n,
- Cutter radius, R_c,

where $(j = 1, 2)$ index gear and pinion.

These preliminary design inputs are taken into considerations to define the rest of the geometry definitions of the spiral bevel gear pairs.

- Number of teeth and gear size: To establish the required reduction ratio there can be infinitely many number of teeth combinations; however, it is recommended to select to obtain a gear pair where there is no common factor in the gear and mating pinion. This is called hunting tooth principle. After specifying gear size, module and number of teeth can be optimized for other requirements according to below Eq. (2.1).

$$m_t = \frac{d_1}{n_1} = \frac{d_2}{n_2}, \tag{2.1}$$

where m_t is outer transverse module.

- Shaft and pitch angles: The angle between two axes of the two members is called as the shaft angle. According to gearboxes types where used in helicopter transmission drive system, the shaft angle changes between 40 and 100. The pitch angles Γ for the pinion and gear can be calculated as

$$\Gamma_2 = tan^{-1}\left[\frac{sin(\Sigma)}{\left({}^{n_1}/_{n_2}\right) + cos(\Sigma)}\right], \tag{2.2}$$

$$\Gamma_1 = \Sigma - \Gamma_2\,, \tag{2.3}$$

- Facewidth and cone distances: In general, face width for all gears should not exceed 30 percent of the outer cone distance or 10/Pd whichever is less. According to [31], in addition to general state mentioned above, face width can be taken as 0.155 of the gear (wheel) pitch diameter. These are recommendations for general applications. In helicopter gearboxes, facewidth is relatively chosen small around 20-25 percent of outer cone distance; because, some percent of increments can be added towards to toe section without changing anything if drive system needs more torque than expected. With the known values of the face width F and outer pitch diameter d of any member, the mean cone distance A_m can be found as

$$A_m = \frac{d_1}{2\,sin(\Gamma_1)} - \frac{F}{2} = \frac{d_2}{2\,sin(\Gamma_2)} - \frac{F}{2} \tag{2.4}$$

The cone distance at any location along the centerline is restricted by the inner and outer cone distances.

$$\mathrm{A}_i = \mathrm{A}_m - \frac{F}{2} < A_x < \mathrm{A}_m + \frac{F}{2} = \mathrm{A}_o \tag{2.5}$$

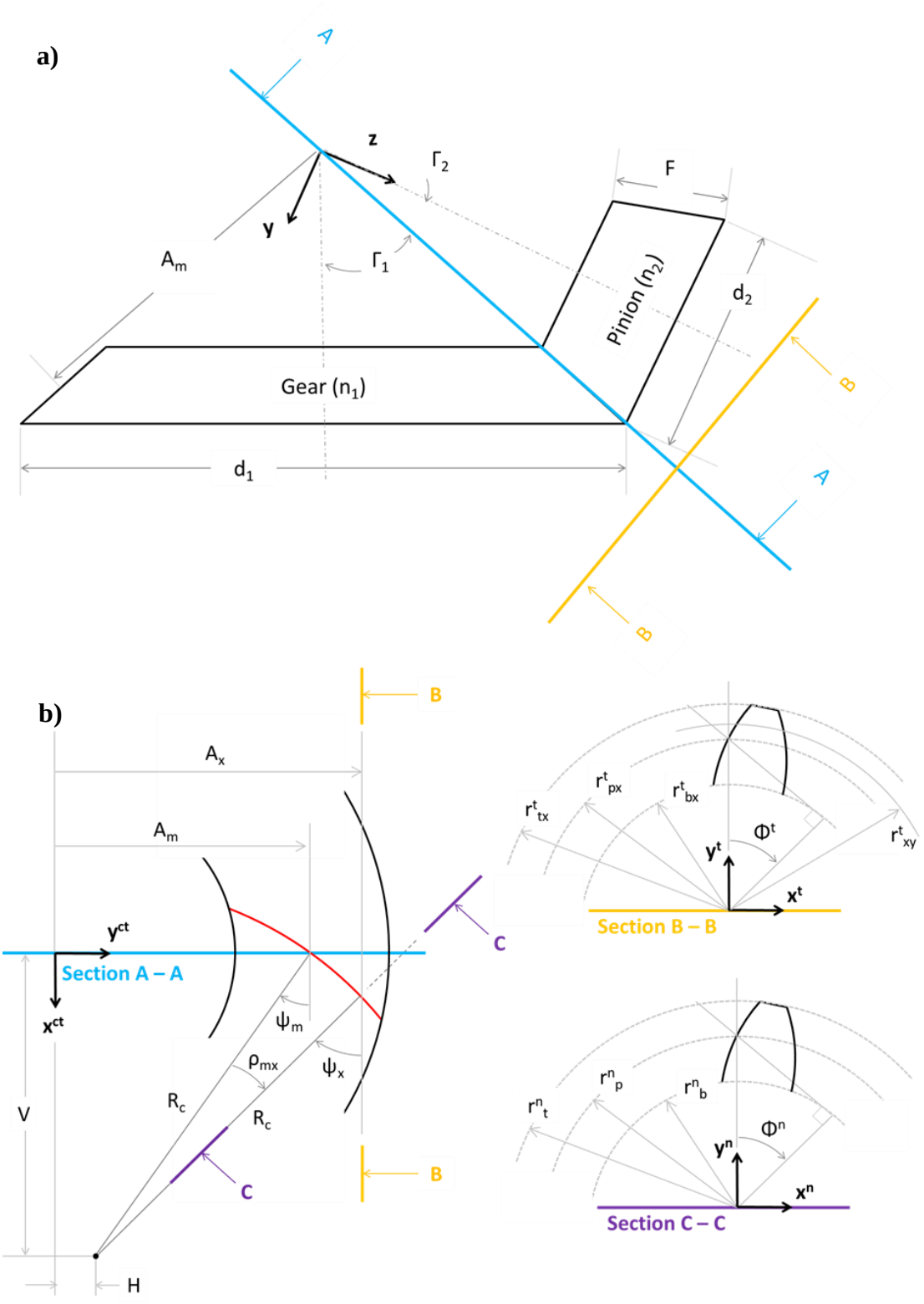

Fig. 2.4 Bevel gear geometry a) Side view b) Sectional views

- Mean spiral angle: In these gearboxes, spiral angle can be changed between 25 and 36 degree for different design spectrums. Gears with 25º degree spiral angle are more suitable for gearboxes requiring low thrust loads and high efficiency, while gears with 35 º degree are used for high speeds applications and smoothness is needed. However, as a rule of thumb, spiral angle is given to satisfy the face contact ratio larger than 2.0 for aerospace applications. Given the mean spiral angle ψ_m and cutter radius R_c, the spiral angle at any cone distance ψ_x can be calculated as

$$\psi_x = sin^{-1}\left[\frac{2A_m R_c\, sin(\psi_m) - {A_m}^2 + {A_x}^2}{2A_x R_c}\right] \qquad (2.6)$$

- Pressure angle: The most commonly used pressure angle for bevel gears is 20 degrees. Aerospace spiral bevel gears generally use higher pressure angles (20°-25°) to reduce bending stress. The pressure angle depends on the inside and outside blade angle of cutter and has effects on gear design in many ways. In general, lower pressure angle increase the bending stress but reduce the contact stress. Lower pressure angles;
    - increase the risk of undercut,
    - reduce the axial and separating forces,
    - increase the toplands and slot width, so allow the use of larger fillet radii,
    - increase the transverse contact ratio.

  The last two items increases bending strength, but bending strength should not fall down more due to the fact that thickness at the root of the tooth is decreased.

Since the normal pressure angle is constant along the spiral at each cone distance, the transverse pressure angle ϕ_x^t are calculated as follows

$$\phi_x^t = tan^{-1}\left[\frac{tan(\phi^n)}{cos(\psi_x)}\right] \tag{2.7}$$

- Addendum and dedendum: Addendum is the radial distance between the pitch circle and the tip circle, while dedendum is the radial distance between the pitch circle and the root circle. Addendum and dedendum portions of gear and pinion are not equal in helicopter gearboxes. Addendum of pinion is designed and manufactured to be larger than that of gear to obtain many advantages, such as increasing fatigue life and reducing scoring temperature. In this study, whole h_t and working depth h_k, addendum $a_{o,j}$ and dedendum $b_{o,j}$ at the outer section is calculated as

$$h_t = 1.888m_t, \tag{2.8}$$

$$h_k = 1.7m_t, \tag{2.9}$$

$$a_{o,2} = 0.460m_t + 0.390m_t(\frac{n_1}{n_2})^2 \tag{2.10}$$

$$b_{o,2} = h_t - a_{o,2}, \tag{2.11}$$

$$a_{o,1} = h_k - a_{o,2}, \tag{2.12}$$

$$b_{o,1} = h_t - a_{o,1}, \tag{2.13}$$

At any cone distance, the pitch radius in the transverse plane is the back cone distance corresponding to that cone distance. Therefore, the radii of the transverse pitch and base circles for both pinion and gear ($j = 1,2$) can be calculated as

$$r_{px,j}^{t} = A_x \, tan\left(\Gamma_j\right) \tag{2.14}$$

$$r_{bx,j}^{t} = r_{px,j}^{t} \cos\left(\phi_x^t\right) \tag{2.15}$$

Then, the root and tip radii are found as follows

$$r_{rx,j}^{t} = r_{px,j}^{t} - b_{x,j}^{t} \tag{2.16}$$

$$r_{tx,j}^{t} = r_{px,j}^{t} + a_{x,j}^{t} \tag{2.17}$$

where $a_{x,j}^{t}$ and $b_{x,j}^{t}$ are the addendum and dedendum for the two members at each transverse section. They can be calculated as

$$a_{x,j}^{t} = a_{m,j}^{t} + (A_x - \mathrm{A}_m) \tan\left(\delta_{j^*}\right) \tag{2.18}$$

$$b_{x,j}^{t} = b_{m,j}^{t} + (A_x - \mathrm{A}_m) \tan\left(\delta_j\right) \tag{2.19}$$

- <u>Circular thickness factor:</u> Circular thickness factor K, is used for determining the outer transverse circular thickness of pinion and gear $t_{o,j}^{t}$ and changes for different design options such as equal stress, equal life and desired option. In addition, normal circular thickness depends on backlash and method of cutting. The backlash is obtained by pinion thickness; because, in this report gear is cut with spread blade (1 rough cut & 1 finish cut) and pinion is cut with fixed setting (1 rough cut & 2 finish cut) as for typical

aerospace applications. Therefore, fixed setting enables the pinion concave and convex are to be cut separately and with desired backlash.

$$t_{o,2}^{t} = \frac{p}{2} - \left(a_{o,1} - a_{o,2}\right)\frac{tan(\phi^{n})}{\cos(\psi)} - Km_{t} \tag{2.20}$$

$$t_{o,1}^{t} = p - t_{o,2}^{t} \tag{2.21}$$

The normal circular tooth thickness along the pitch line at any cone distance $t_{px,j}^{n}$ is calculated for both members as

$$t_{px,j}^{n} = t_{px,j}^{t}\cos\left(\psi_{x}\right) \tag{2.22}$$

where $t_{px,j}^{n}$ is the normal circular tooth thickness along the pitch line at any cone distance.

- Cutter Radius: Cutter radius, R_c affects many geometric parameters of spiral bevel gears. Cutter radius has also effects on strength of gears. A small cutter radius increases contact ratio by generating large spiral angle differences at the both ends of tooth, which minimizes contact pattern movements under different load conditions. Therefore, gear pair is working with more stable contact pattern and then it increases surface fatigue durability. However, a small cutter radius results in unbalanced tooth thicknesses at different sections such as inner, mean and outer, so; bending strength decreases at section having small tooth thickness. Finally, cutter radius is to be selected according to Eq. (2.23) in order to balance the gear pair for these considerations.

$$R_c = 1.1A_m \cos(\psi) \tag{2.23}$$

By considering all details explained above in terms of macro geometry, a spiral bevel gear pair is designed to be used in this study. The main details of this gear pair are tabulated in Table 2.1.

Table 2.1 Parameters of the example system

Gear Parameters		
	Pinion	Gear
Number of teeth	23	47
Module (mm)	3.0	3.0
Pitch diameter	69.000	141.000
Outer cone distance	78.489	78.489
Normal pressure angle (°)	20	20
Shaft angle (°)	90	90
Pitch angle (°)	26.08	63.92
Mean spiral angle (°)	27	27
Hand of spiral	Left	Right
Face width (mm)	25	25
Cutter radius (mm)	47.625	47.625
Outer addendum	3.388	1.579
Outer whole depth	5.531	5.531
Face angle	28.76	65.18
Root angle	24.82	61.24
Mean transverse circular thickness	4.625	3.154
Mesh Parameters		
Damping coefficient (ζ)	0.03	
Backlash (mm)	0.04	

2.1.3 Micro Geometry

Generally, a helicopter has a vast variety of load spectrums due to different flight conditions and gearboxes of it are to be designed to work properly during these operations. In order to do that, spiral bevel gears used in these gearboxes needs flank modifications on their tooth surface to have a stable contact under different deflections. Macro geometry given in Table 2.1 is used to generate the micro geometries and corresponding machine settings in Gleason Cage software for this study.

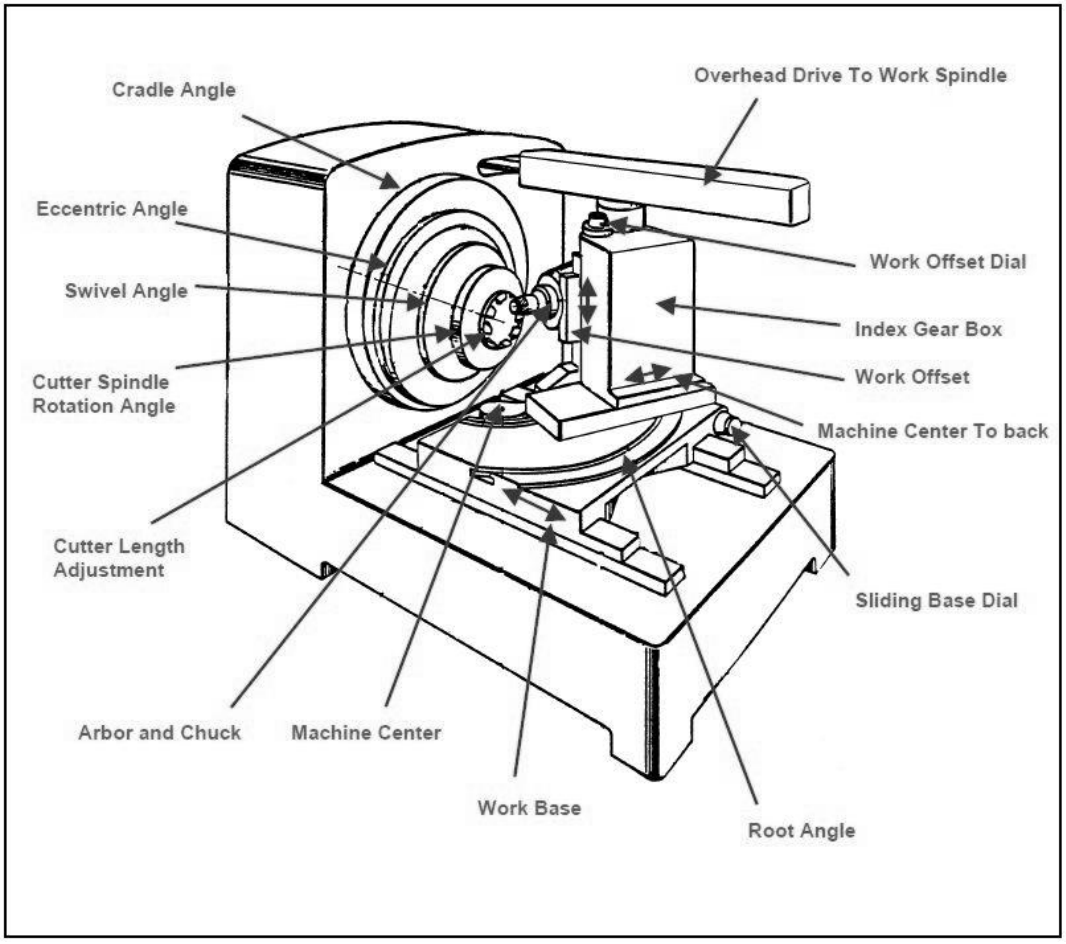

Fig. 2.5 Machine Settings [1]

Corresponding machine settings of spiral bevel gear for these ease-offs are motion elements of parameters shown in Fig. 2.5. Each elements affects surface generation model of tooth surface. These elements are used in terms of higher order polynomials to give tooth flank modifications in details for spiral bevel gears used in helicopter gearboxes. Gear micro geometries with real machine settings for concave and convex flanks of actual tooth are designed to obtain different tooth flank modifications. Pinion concave-gear convex side is taken as drive side of gear pair. Therefore, tooth flank modifications are especially done on this drive side. Although, direction of rotation does not change, operational conditions may produce torque changes time to time, which causes a contact and loading on the coast side. Hence, to avoid gear strength problems, some tooth flank modifications are also given on coast side.

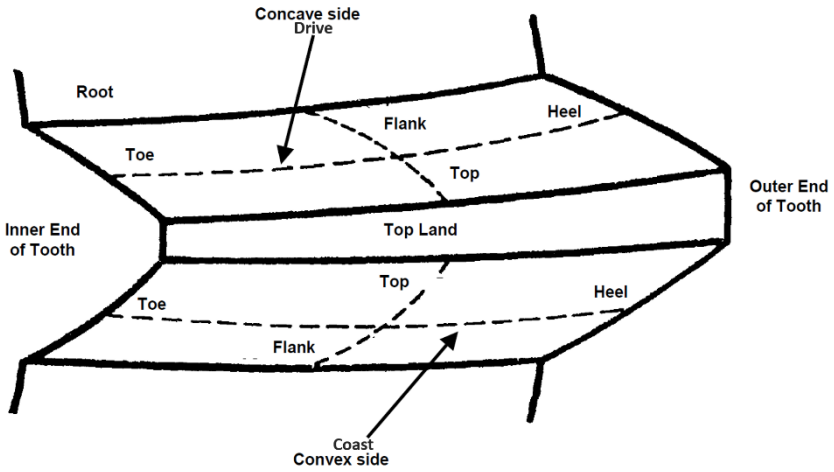

Fig. 2.6 Tooth nomenclature of a spiral bevel gear [1]

Table 2.2 Real machine settings of gear pair micro geometry with different types of crowning

Machine Settings	Profile Crowning		Lengthwise Crowning		Flank Twist	
	Concave	Convex	Concave	Convex	Concave	Convex
Cutter point radius (mm)	44.1677	51.2103	48.8950	48.6410	46.3550	49.6570
Machine center to cross point (mm)	-3.83510	4.22064	-1.79794	-0.86535	3.38082	0.64237
Sliding base (mm)	1.18115	-2.20096	0.32588	-0.06566	-1.84838	-0.69865
Blank offset (mm)	0.00000	0.00000	-2.54000	0.00000	0.00000	0.00000
Radial distance (mm)	57.4470	65.8424	58.6786	61.29528	62.82263	62.92223
Machine root angle (deg.)	24.82	24.82	24.82	24.82	24.82	24.82
Swivel angle (deg.)	17.08	16.42	18.92	16.60	14.88	16.91
Tilt Angle (deg.)	0.00	0.00	0.00	0.00	0.00	0.00
Ratio of Roll	2.122409	2.441129	2.17343	2.243307	2.346762	2.326863
Modified Roll Coefficient C	0.00000	0.0000	0.0000	0.0000	-0.09165	-0.08276
Modified Roll Coefficient D	0.00000	0.0000	0.0000	0.0000	-0.10000	-0.10000

As shown in Fig. 2.7, Ease-Off is used to be a representative way of showing the sum of tooth flank modifications of drive and coast side in a gear pair. The Ease-Offs show misalignments of gear mesh due to crowning applied on tooth surfaces of gear pairs. The curved upper surfaces are identical to the flat bottom surfaces if there is no crowning and no misalignments.

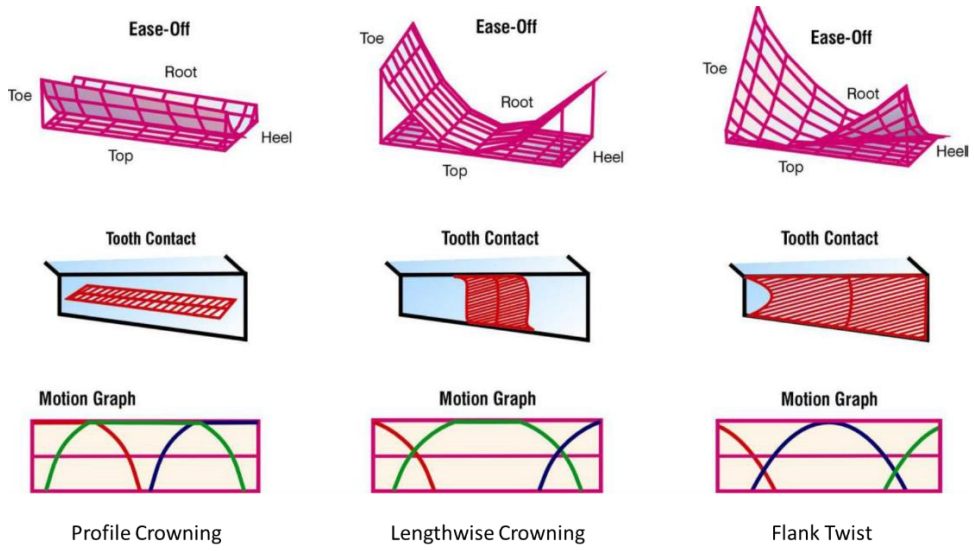

Fig. 2.7 Tooth flank form modifications [33]

Flank form modifications are deviations from conjugate action which can be expressed as one of gear pair contacts with other gear pair tooth flank and rolls perfectly without motion error. That is, the change angle from one contact line to another contact line is exactly same discrete angles created by their ratio during rotation of gear pairs. Conjugate tooth action is not possible in the gearboxes due to manufacturing tolerances and load-dependent deflections of shafts, housings and bearings. Therefore, gear tooth flank requires three main crowning types which are a circular relief in profile, lead and diagonal directions. Gleason CAGE software is used to obtain Ease-Offs for gear pairs with three different flank modifications.

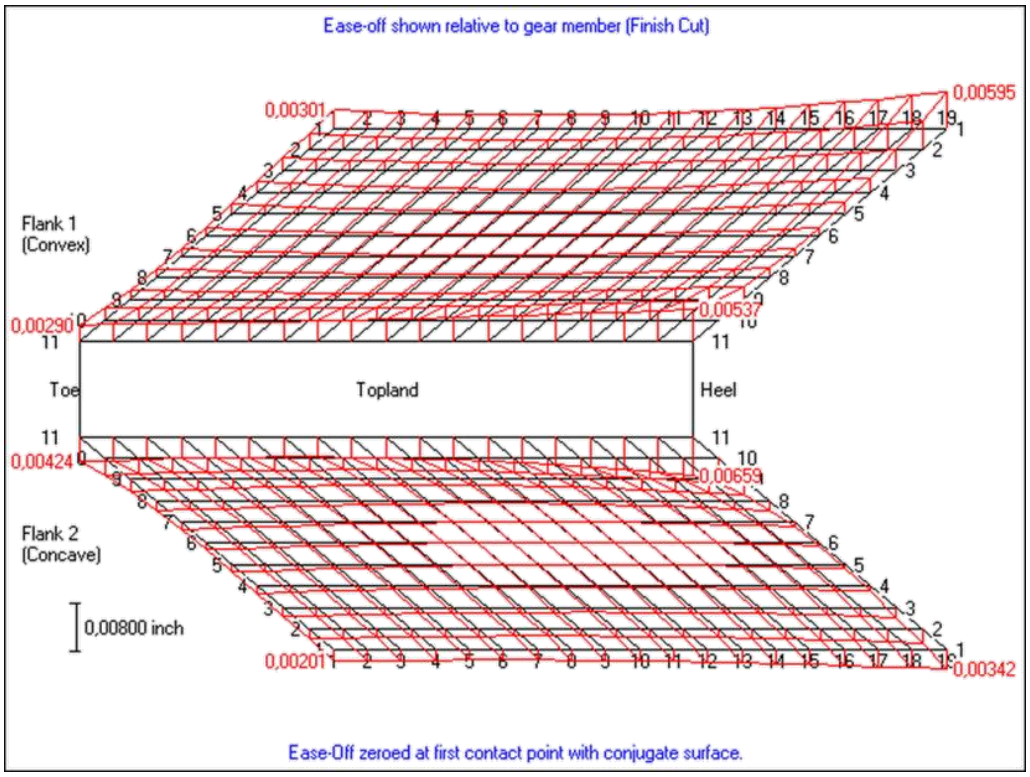

Fig. 2.8 Profile Crowning Ease-Off.

Profile crowning, a circular relief in profile direction, is obtained by designing curvature on cutter blade or grinding disk to give profile in or profile out on tooth surface. Ease-Off of actual tooth with profile crowning is generated and used in this study is shown in Fig. 2.8 and corresponding machine setting for profile crowning is given in Table 2.2.

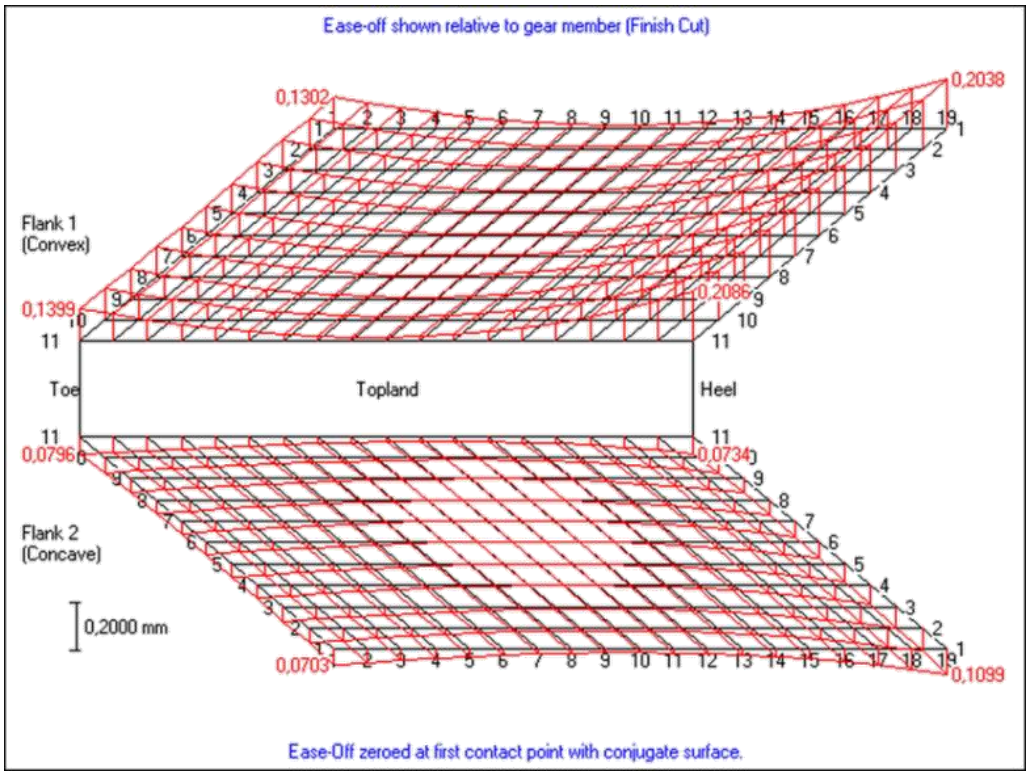

Fig. 2.9 Lengthwise Crowning Ease-Off.

Length or lengthwise crowning, a circular relief in lead or along facewidth direction is based on cutter radius modifications, which provides a clearance at toe and end of tooth sections. Fig. 2.9 shows ease-off of actual tooth with length crowning and corresponding machine setting tabulated at Table 2.2.

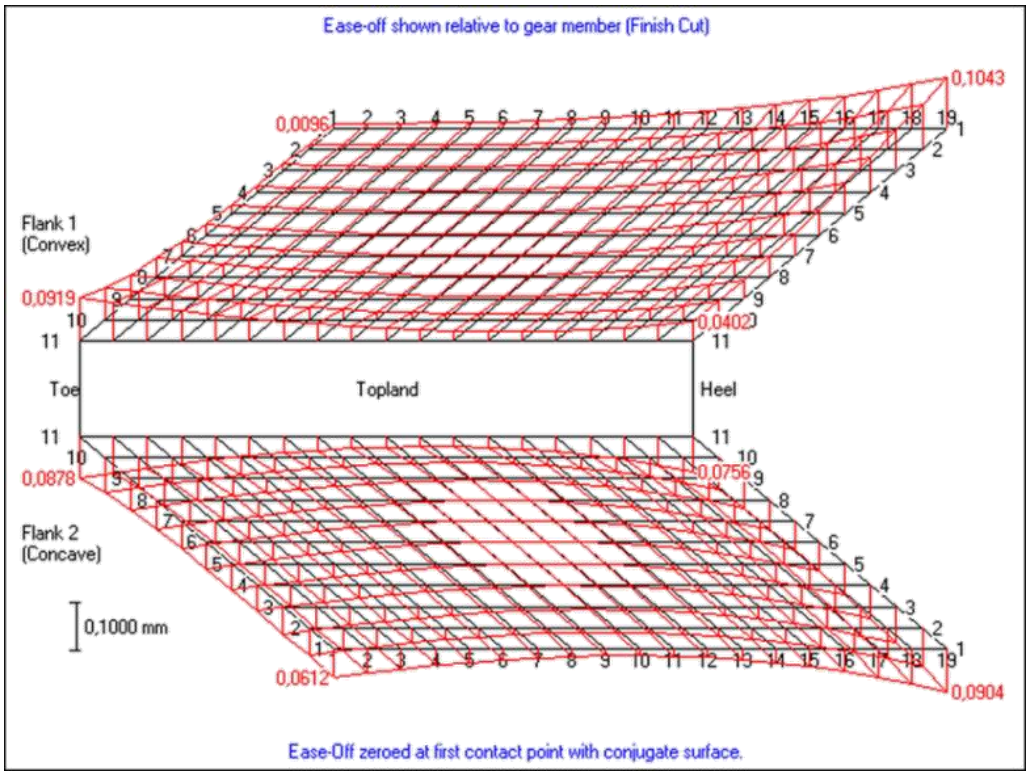

Fig. 2.10 Flank Twist Ease-Off.

Flank twist, a circular relief in diagonal direction, is consequences of cutter head tilt around machine root angle or high order modulation of ratio roll setting. As shown below in Fig. 2.10**,** there is bearing contact along one diagonal while there is stock on other diagonal.

The E, P, G and alpha values are selected as constant and set to zero in these ease-offs to avoid any further complexities. The E, P, G and alpha are constants representing the deflection of gear and pinion relative to the gear crossing point as torque is applied to the gear. Fig. 2.11 illustrates how E, P,G and Alpha are defined relative to the gear and pinion.

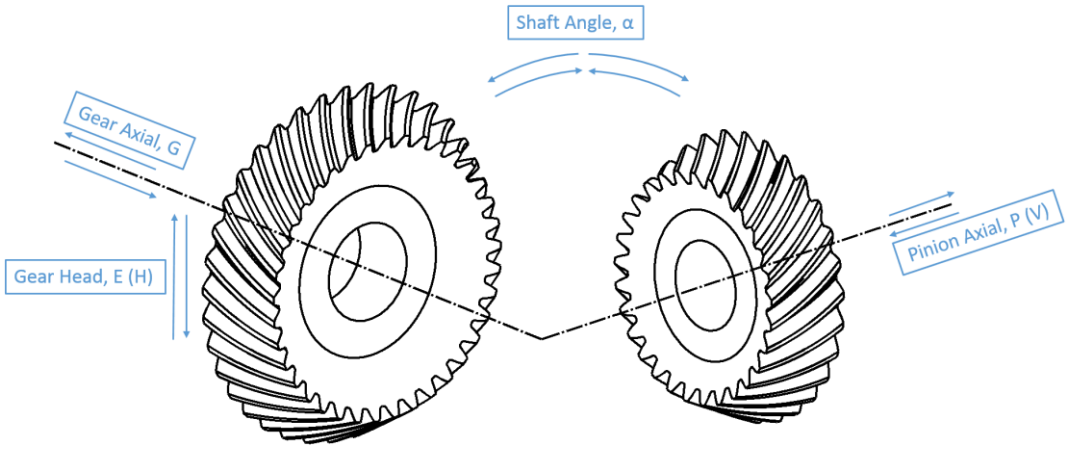

Fig. 2.11 Deflections E,P,G and alpha

The path of contact behaviors of unloaded bench test simulation, 100Nm, 200Nm and 400Nm for all three crowning types are presented in Fig. 2.12 on the gear convex side. The separation factor is 0.00635mm and all the meshed gear pairs are assumed without any deflections and misalignments in this study. Furthermore, for gear pairs used with these tooth modifications, loaded contact patterns and contact stresses are depicted in Fig. 2.13 for 400Nm load torque. Loaded contact patterns show the behaviors of tooth flank modifications. The bench test simulation in Fig. 2.12 is unloaded contact pattern check. Here, the angle of inclination of the path of contact is in the opposite direction to the leaning of the lines of contact. Hence, the nature of the bias for all three modifications is in the bias-in format.

Contact pattern on the profile crowned teeth at unloaded case is distributed at the pitch cone line region as shown in Fig. 2.12-a. The path of contact is close to horizontal nature with a shallow “S” shape. At some of the instances, the transition of the contact path is not stable. As the load torque increases, the contact area enlarges to the whole face-width. The gear pair contact area and path with lengthwise crowning are at the middle as expected in Fig. 2.12-b. The contact path is stable and close to vertical direction. The contact area is the smallest of all three modifications. Even if not edge contact is observed at 400Nm, there is a risk of

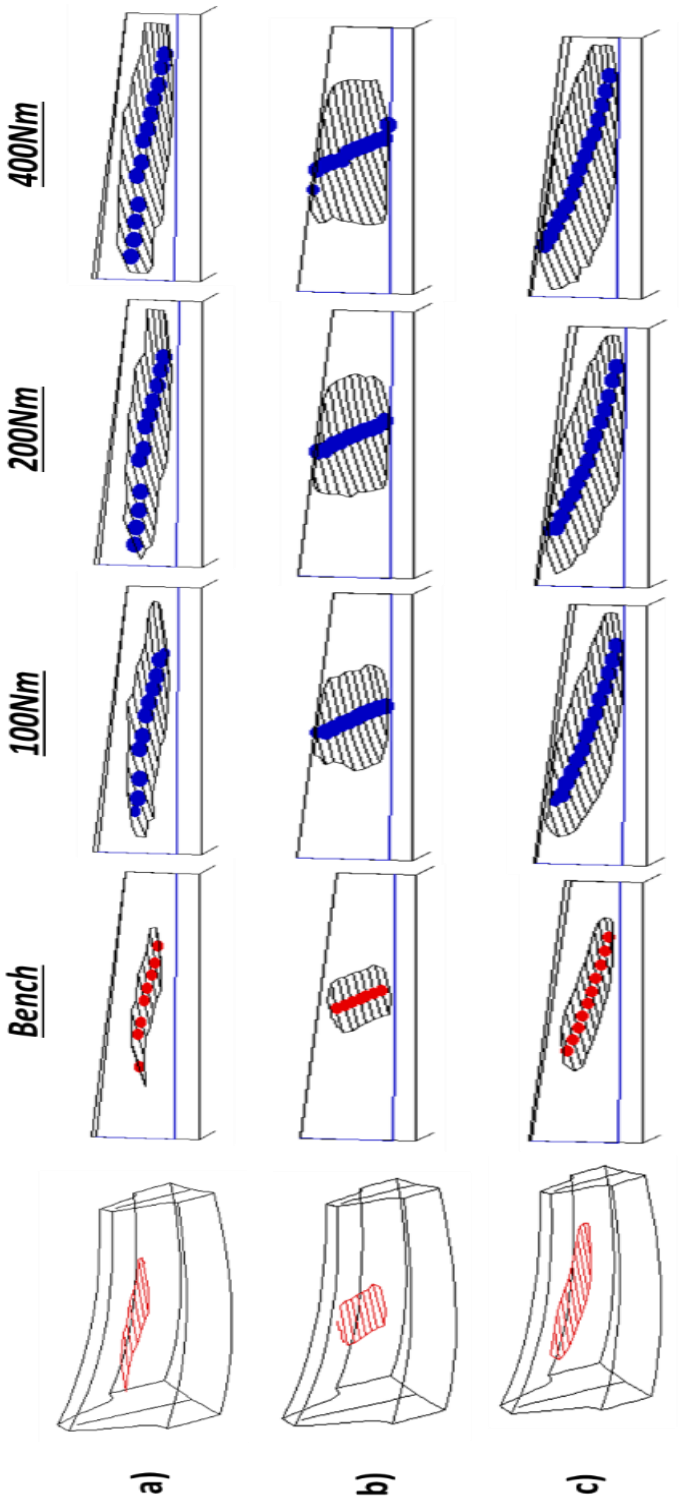

Fig. 2.12 Path of contact on gear convex; **a)** profile crowning, **b)** lengthwise crowning and **c)** flank twist

possible edge contact at the higher loads in this design. The unloaded contact pattern of flank twist design is diagonal on tooth surface with the lowest point being closer to the toe. As the load increases the contact area enlarges to the whole face-width and the contact area moves to the heel region more than the toe side. The highest contact area is observed in this modification. The contact path is more stable than the other two versions. The edge contact is avoided and the contact area is more evenly distributed. In Fig. 2.13, under 400 Nm torque load, the contact stresses on tooth surfaces for all three ease-off types are depicted. Gear pair having with flank twist has lower contact stress due to the high surface contact area and contact ratio. Although, the edge contact is avoided in all three gear tooth topographies, the design with lengthwise crowning has the highest risk for an edge contact if the load is increased or misalignments realized.

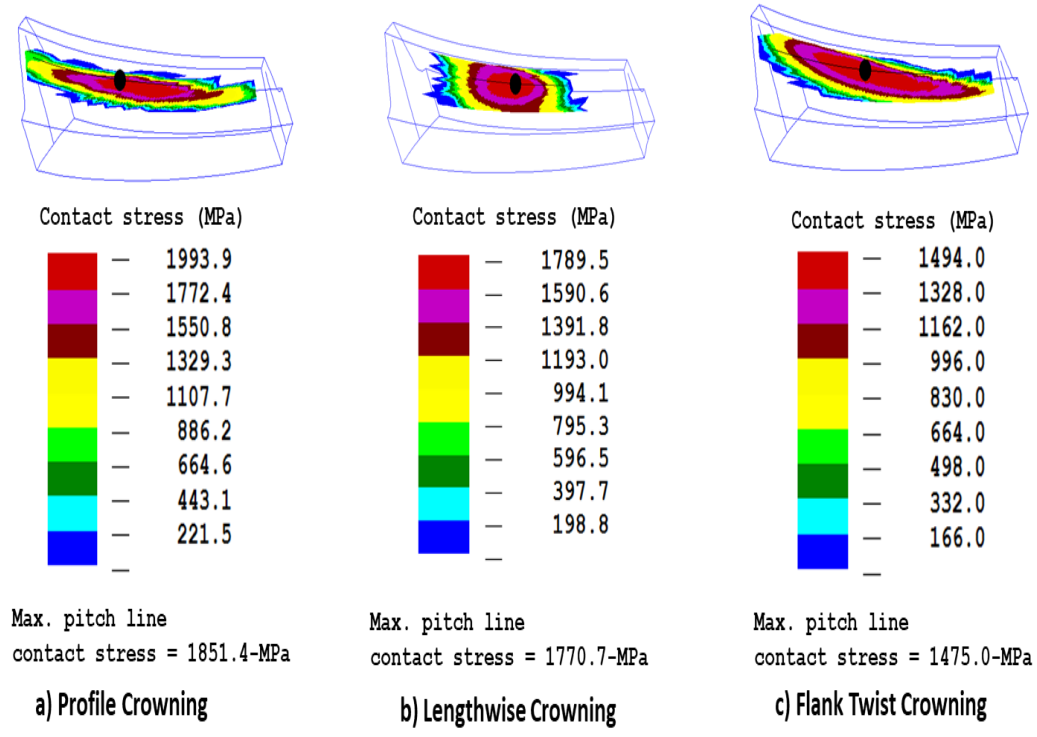

Fig. 2.13 Contact stress at 400Nm torque on gear convex; **a)** profile crowning, **b)** lengthwise crowning and **c)** flank twist

2.2 Mesh Stiffness Model and Case Studies

2.2.1 Mesh Model Development

The parameters used to model the mesh coupling between the gears are mesh stiffness, mesh damping, acting point and direction of line of action. Mesh spring, which extends along line-of-action between the mesh points of pinion and gear, is shown in Fig. 2.14.

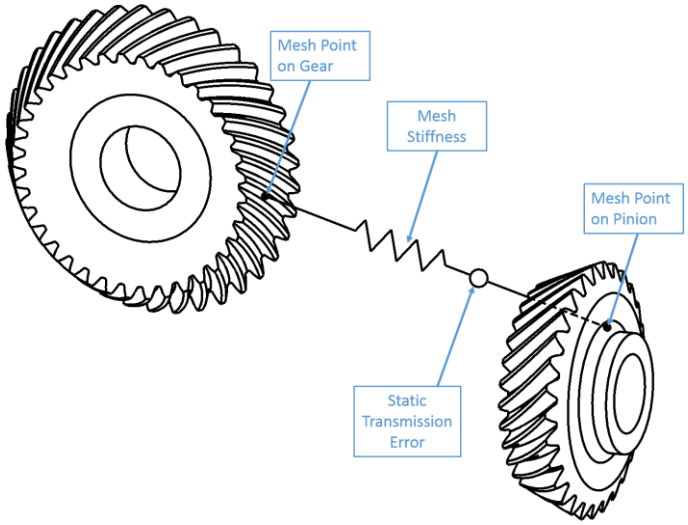

Fig. 2.14 Mesh Model.

These mesh parameters vary considerably for a spiral bevel gear pair as the gear pair rolls and are obtained by applying a three-dimensional quasi-static loaded tooth contact analysis (LTCA) that generates a detailed load and pattern distributions. This LTCA is conducted on a commercial package, Calyx, which combines finite element formulation away from the contact area and surface integral method near the contact area. Load distribution and angular transmission error are calculated from the rigid body rolling motions of the gear pair at each specified time step over a mesh cycle [34].

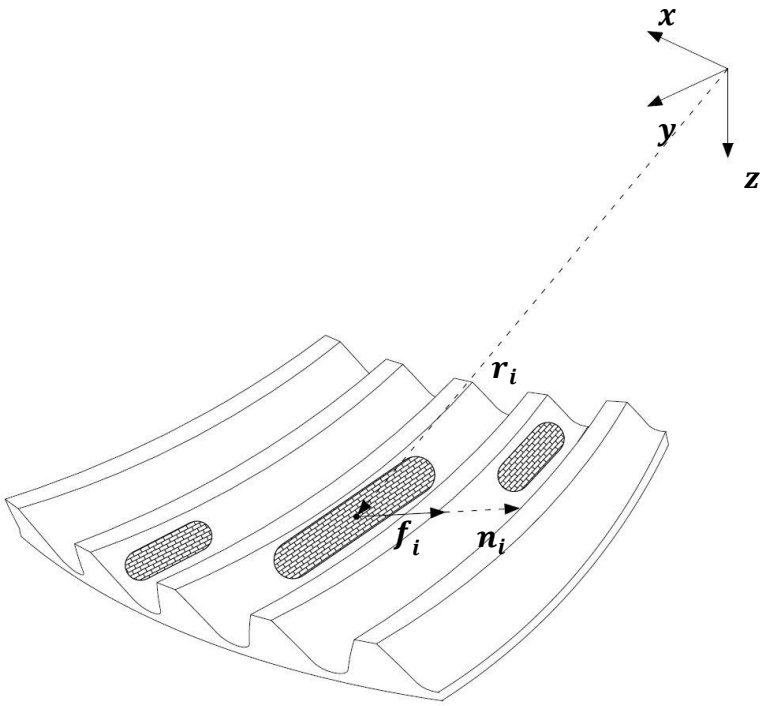

Fig. 2.15 Normal force and radius vectors representation.

Calyx divides the tooth contact surface into a total of N contact cells and calculates the surface normal vector, n_i, the position vector, r_i, and the normal force vector with a magnitude of f_i, on each cell.

$$F_x = \sum_{i=1}^{N} n_{ix} f_i \tag{2.24}$$

$$F_y = \sum_{i=1}^{N} n_{iy} f_i \tag{2.25}$$

$$F_z = \sum_{i=1}^{N} n_{iz} f_i \tag{2.26}$$

$$F_{tot} = \sqrt{{F_x}^2 + {F_y}^2 + {F_z}^2} \tag{2.27}$$

Using these forces, line of action $n_{lm}(n_x, n_y, n_z)$ can be calculated as

$$n_x = \frac{F_x}{F_{tot}} \qquad n_y = \frac{F_y}{F_{tot}} \qquad n_z = \frac{F_z}{F_{tot}} \tag{2.28}$$

In order to calculate effective mesh point, $r_{lm}(x_r, y_r, z_r)$, total moment is needed on the contact area and derived according to following equations.

$$M = \sum_{i=1}^{N} f_i (r_i \times n_i) \tag{2.29}$$

$$z_r = \sum_{i=1}^{N} r_{iz} f_i \Big/ \sum_{i=1}^{N} f_i \tag{2.30}$$

$$x_r = \frac{(z_r F_x - M_y)}{F_z} \tag{2.31}$$

$$y_r = \frac{(F_x x_r - M_z)}{F_x} \tag{2.32}$$

Using load distribution on the tooth surface, effective mesh point and line of action vector is obtained. Then, directional rotational radius is calculated according to Eq. (2.33).

$$\lambda_l = n_{lm} \cdot (j_{lm} \times r_{lm}) \tag{2.33}$$

where n_{lm} and r_{lm} are the line of action directional cosine vector and position vector of the effective mesh point, respectively. j_l is unit vector of pinion or gear rotating axis.

By Solving Eq.(2.33) directional rotation radius is obtained for gear rotation axis, where angular transmission error is defined.

$$\lambda_z = n_y x_r - n_x y_r \tag{2.34}$$

Furthermore, translational transmission error and mesh stiffness are calculated by using the known values of mesh force, directional rotation radius and loaded and unloaded angular transmission error, e_{la} and e_a.

$$e_l = e_{la}\lambda_z \qquad\qquad e = e_a\lambda_z \tag{2.35}$$

$$k_m = \frac{F_{tot}}{e_l - e} \tag{2.36}$$

where e_l and e are loaded and unloaded translational transmission errors and k_m is effective mesh stiffness.

2.2.2 Application of the Mesh Stiffness Model

In this chapter, the profile, lengthwise and flank twist crowning modification effects are investigated on drive and coast sides of the teeth at different load levels. The geometric properties established in Table 2.1 and Table 2.2 are first used to calculate the directional rotation radii of the gear and the pinion for 100Nm, 200Nm and 400Nm load torque values. The load share is presented at 400Nm for all three ease-off topographies. The static transmission error (STE) is calculated and the results are presented for drive and coast sides. Next, the loaded transmission error (LTE) is developed for different load levels. Finally, mesh stiffness is obtained for different load torque levels. Directional rotation radius is one of the main parameters to be

calculated. It is closely related to the path of contact and surface normal vectors as formulated above. From Fig. 2.16 to Fig. 2.19 show directional rotation radii of gear and pinion pair for the three ease-of topographies under 100Nm, 200Nm and 400Nm load torque levels. Furthermore, the directional rotation radii are plotted for drive and coast sides, as well. The line thicknesses increase from lighter to heavier as the torque load value increased in the plots. The range of the pinion roll angle shown in all the plots is only for one pitch. These features are kept in the next figures through the rest of this paper unless otherwise stated. Fig. 2.16 and Fig. 2.17 show directional rotation radii of gear under different loads for drive and coast sides, respectively.

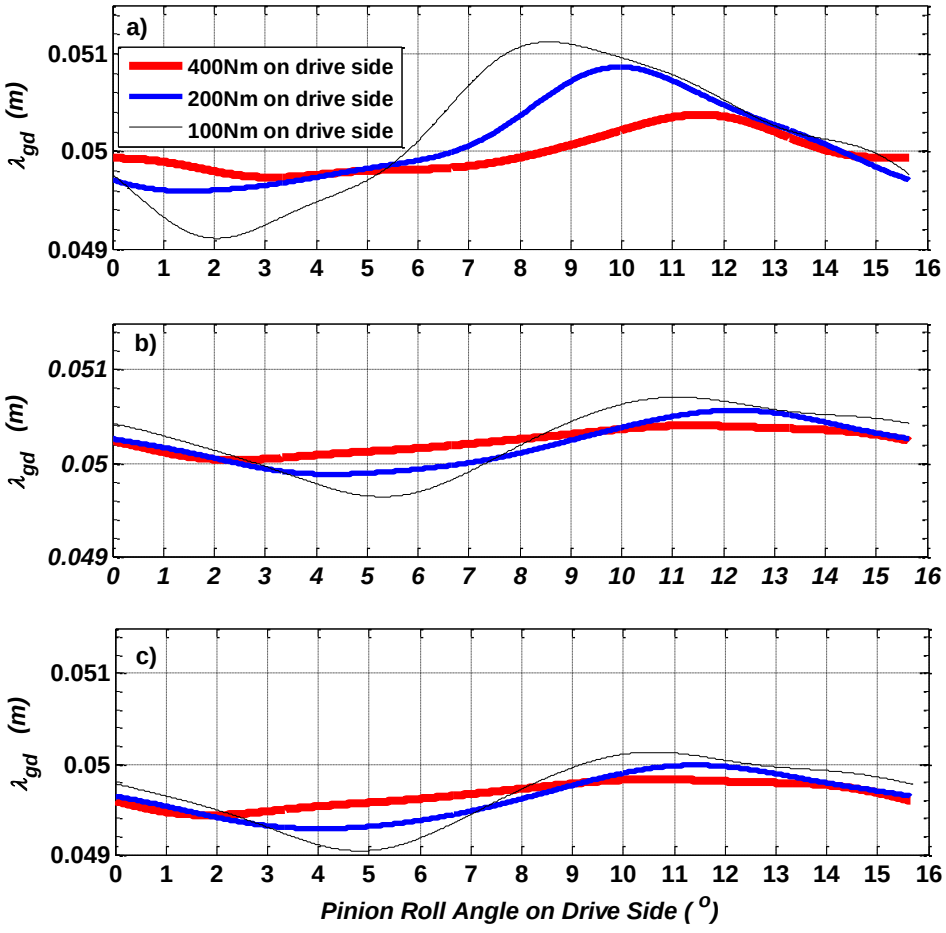

Fig. 2.16 Directional rotation radius of the gear member for: **a)** profile crowning drive side; **b)** lengthwise crowning drive side; **c)** flank twist drive side

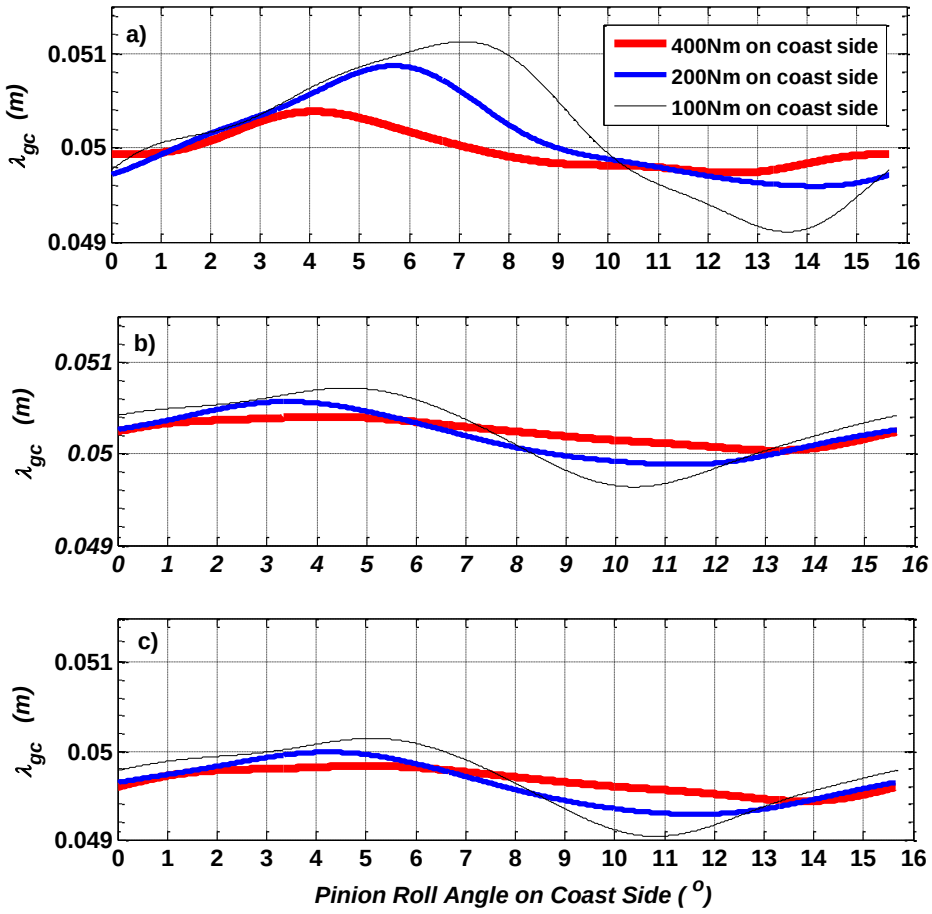

Fig. 2.17 Directional rotation radius of the gear member for: **a)** profile crowning coast side; b**)** lengthwise crowning coast side; **c)** flank twist coast side

Fig. 2.18 and Fig. 2.19 show directional rotation radii of pinion under different loads for drive and coast sides, respectively. Here, the roll angle magnitude of drive side is treated as rotation in clockwise direction while the coast side is counter-clockwise direction. Thus, the pinion roll angle on gear drive side starts from the reverse of the coast side. In these figures directional rotation radii are shown for profile crowning a), lengthwise crowning b) and flank twist c).

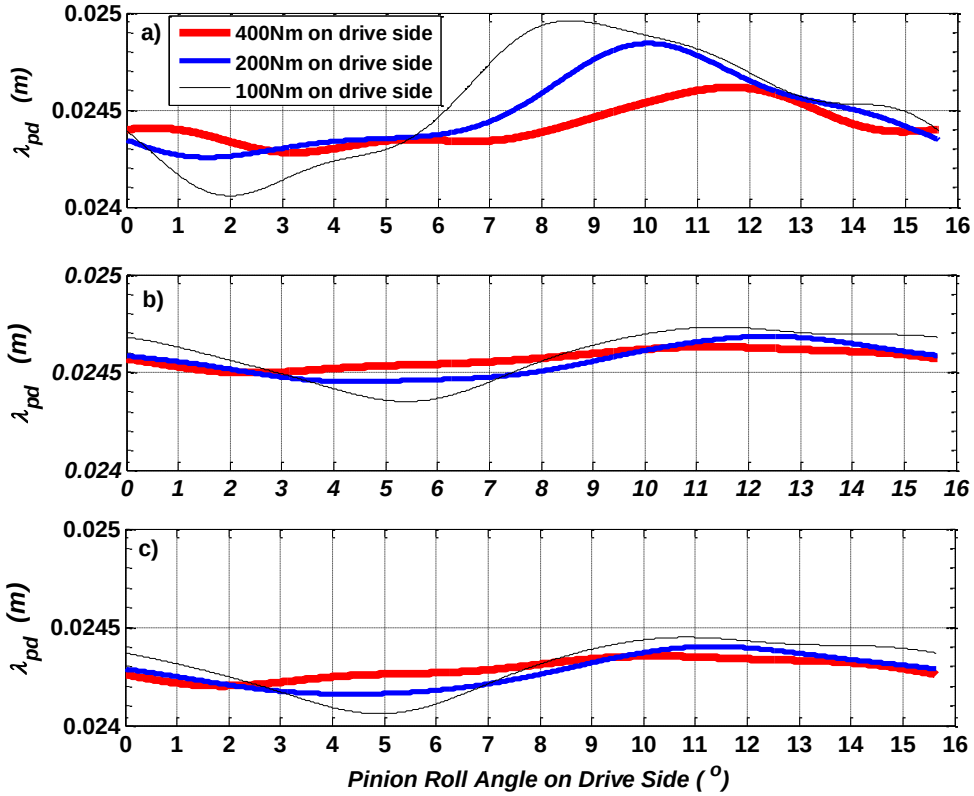

Fig. 2.18 Directional rotation radius of the pinion member for: **a)** profile crowning drive side; **b)** lengthwise crowning drive side; **c)** flank twist drive side

In all ease-off types, the trends of the pinion and gear in the directional rotation radius are very close to each other, because of the designed ease-off topographies are very similar to each other. Variation on the radii for both drive and coast side of gear teeth decreases as the loads increase on the gear pair. However, the magnitudes of the changes are relatively small when compared to the tooth proportions. The overall trend of the directional rotation radius for gear and pinion shows close similarities. The highest directional rotation radius magnitude and the change are observed in profile modification. The lengthwise crowning provides a smaller variation in the directional rotation radius since the path of contact is pocketed in the midst of the tooth. The smallest directional rotation radius is present with flank twist.

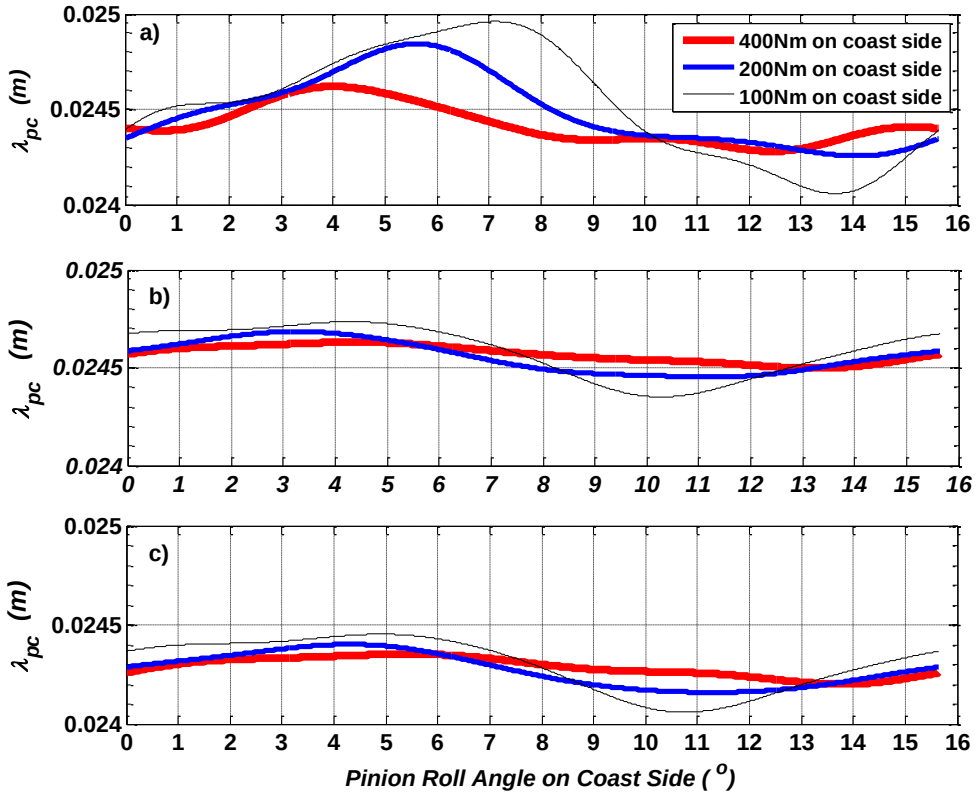

Fig. 2.19 Directional rotation radius of the pinion member for: **a)** profile crowning coast side ; **b)** lengthwise crowning coast side; **c)** flank twist coast

In a rigid and static case, the normal load at the mean pitch point is calculated as 8253.5N at 400Nm load torque based on the standard gear tooth force formula [2]. The load share between consecutive teeth at 400Nm load torque are presented in Fig. 2.20-a), b) and c) for the profile crowning, lengthwise crowning and flank twist, respectively. The simulation is conducted with Calyx. Here, the range of the pinion roll angle is for 3 mesh cycle to capture the all the teeth in contact. The teeth share the total mesh loads as shown in Fig. 2.20-a) for profile crowning such that when the simulation starts at 0.734˚ the load on tooth # 1 is around 6800N levels while load on tooth #2 is about 1200N levels. At the mesh cycle progress the load on tootn#1 reduces and tooth #2 increases. The load is shared equally at 6.5˚. Tooth #1

load share becomes significantly small around 13.2˚; hence, the tooth#1 is still in contact, kinematically, with very light load until 13.9˚ at when tooth # 3 enters the mesh. Further, the cycle continues in the similar manner. The mesh cycle for each tooth starts from the toe as presented in Fig. 2.12. The general behavior of lengthwise crowning and flank twist are similar to profile crowning. The major differences are the start of the contact of tooth #3 and the duration of tooth mesh contact. The total load variation through the mesh cycle is presented in Fig. 2.21. Here, profile crowning and flank twist show uniform variation in the 3 mesh cycles while the lengthwise crowning is relatively unstable. The reason for this condition is that, the lengthwise crowned gear has the most potential to present an edge contact start and the end of the mesh cycle as observed in Fig. 2.13. Therefore, during the quasi-static finite element calculations the lengthwise crowned gear presents an increase in the starting load at each tooth engagement. The standard rigid gear mesh load calculation at mean pitch point and the total load transferred with quasi-static finite element calculations have obvious differences. Because, finite element calculation includes the effects of the deflections on the gear teeth, moment arm changes due to the moving in the actual contacting point (directional rotation radius), the effect of the actual contact point pressure angle, spiral angle on the normal vector. The mesh forces are obtained by a torque balancing; hence, the total mesh force fluctuations are realized as shown in Fig. 2.21.

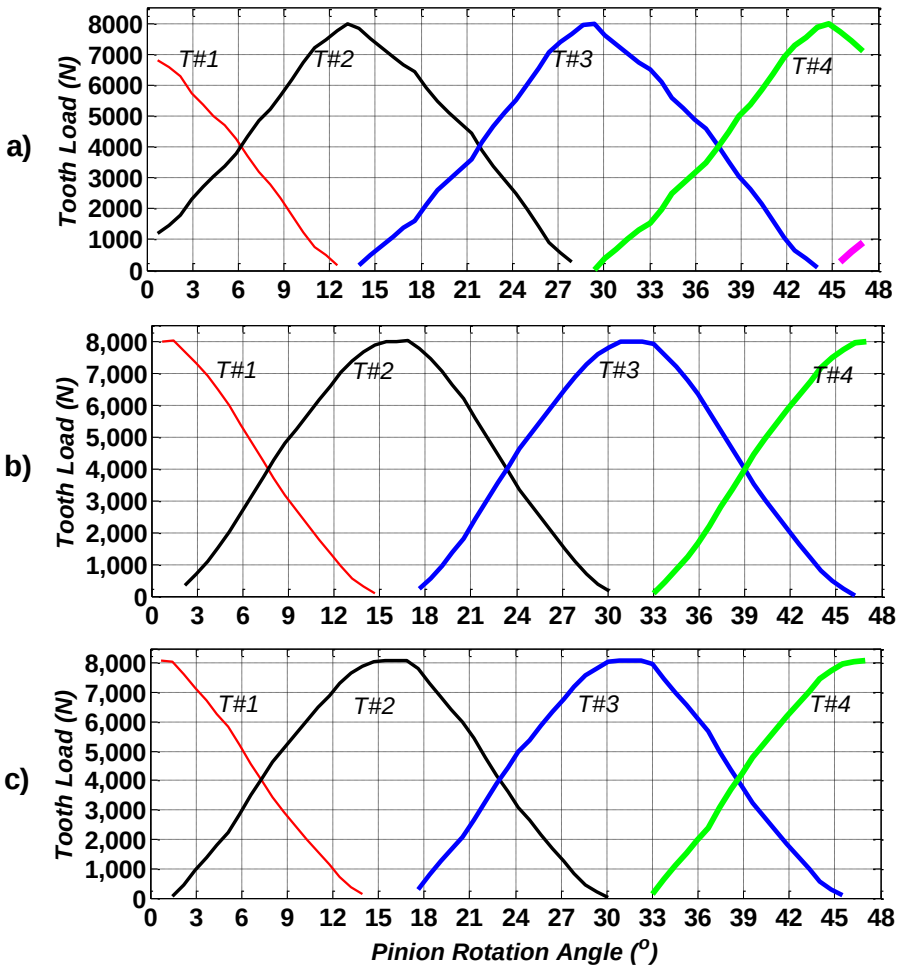

Fig. 2.20 Load share at 400Nm load torque: **a)** profile crowning; **b)** lengthwise crowning; **c)** flank twist

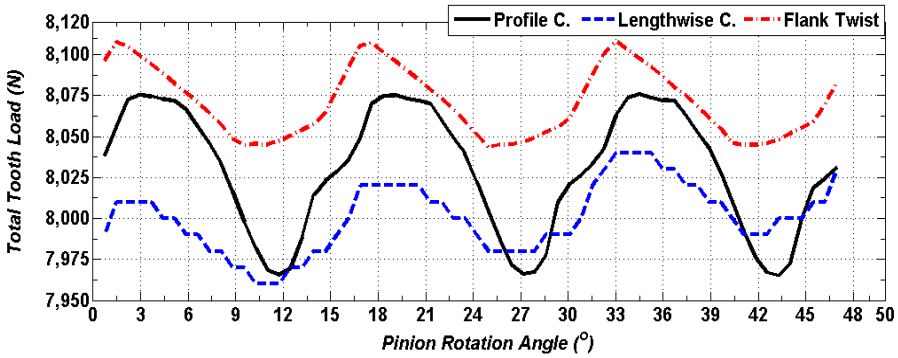

Fig. 2.21 Total load variation through mesh cycles

Translational unloaded static transmission errors (STE) for drive and coast sides are shown in Fig. 2.22 for profile crowning, lengthwise crowning and flank twist. The STE plots purpose is to define the nature of the motion transmitted. The pinion is assumed to be the driving member at constant speed and the gear is the driven. In Fig. 2.22-a, STE of profile crowned pair changes its values from positive to negative. This means that at positive STE the pinion roll angle instants the gear rotation is leading the theoretical position while at negative regions the gear is lagging the theoretical position. The STE for the lengthwise crowning is presented in Fig. 2.22-b for drive and coast sides. Both drive and coast sides show a similar trend and the magnitudes at positive values. Hence, the gear rotation is leading the theoretical position for the lengthwise crowning. The STE of the flank twist modified design is shown in Fig. 2.22-c for drive and coast sides. The motion starts and ends at the positive STE values while in the midst of the meshing the STE is at negative values. Hence the gear leads at the start and end of the meshing while lags in the midst of the meshing.

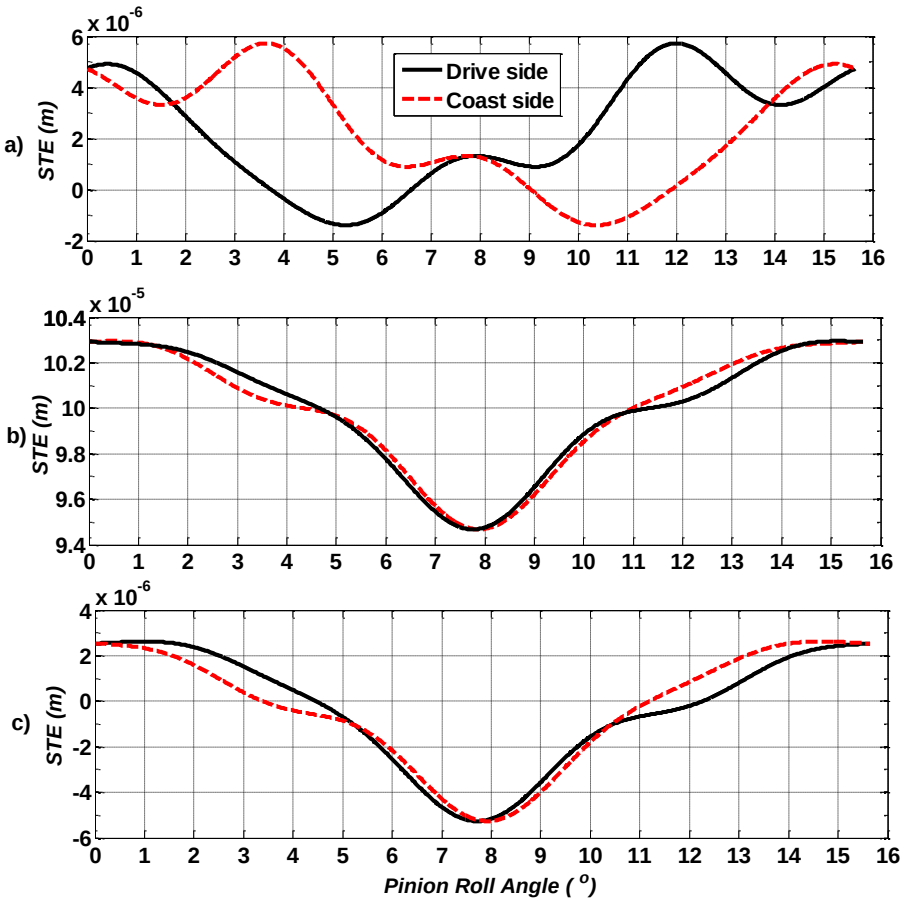

Fig. 2.22 Translational static transmission error for: a) profile crowning; b) lengthwise crowning; c) flank twist

Translational loaded transmission errors (LTE) of gear pair with profile crowning are shown in Fig. 2.23 for drive and coast sides at different torque load levels. As the torque increases magnitude of LTE grows. Here, the LTE values are all negative and differs from the nature of the STE. The variation of LTE at 200Nm torque load is relatively smaller than 100Nm and 400Nm. This indicates that around 200Nm there is a load torque that gives the most optimum LTE during the operation. This statement is true for the rest of the modifications. The LTE is depicted in Fig. 2.24 for drive and coast sides at different load levels.

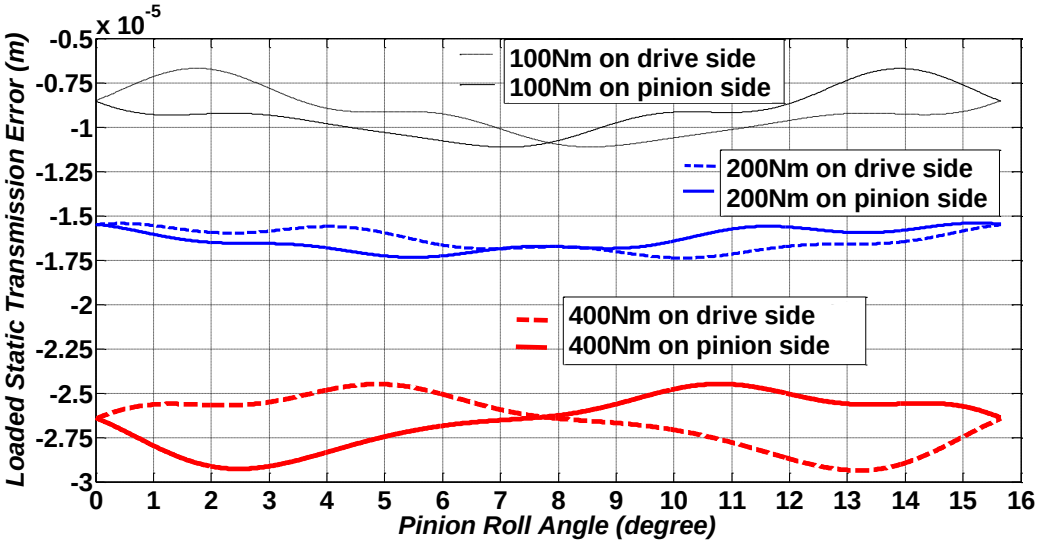

Fig. 2.23 Loaded translational static transmission errors for profile crowning

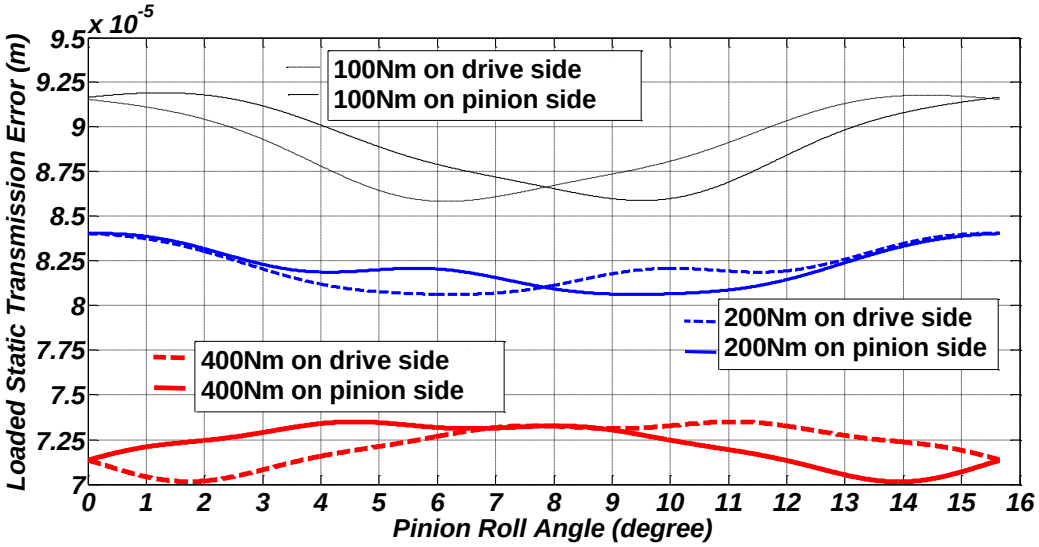

Fig. 2.24 Loaded translational static transmission errors for lengthwise crowning

The magnitude of the LTE is positive in all load cases and the LTE value reduces as the load increases. The LTE of flank twist is shown in Fig. 2.25 for drive and coast sides at different loads. The LTE values are all negative at all the selected load levels. The magnitude of the LTE increases as the load grows.

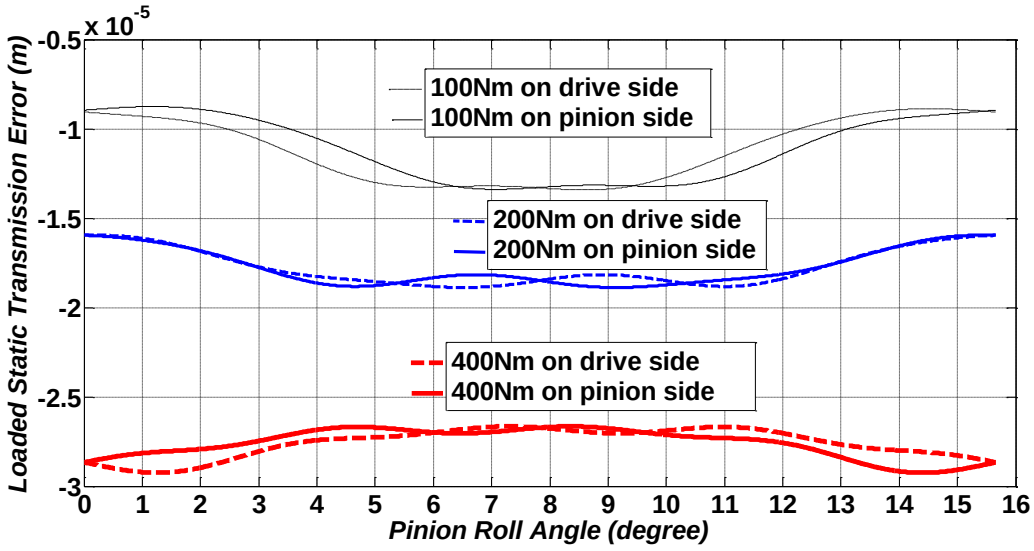

Fig. 2.25 Loaded translational static transmission errors for flank twist crowning

Finally, for profile crowning, the mesh stiffness variations of gear are illustrated in Fig. 2.26. The gear mesh stiffness increases as the function of the growth in the applied load. The drive and coast sides of the tooth shows an identical behavior because of the very similar ease-off topographies given in the drive and coast sides.

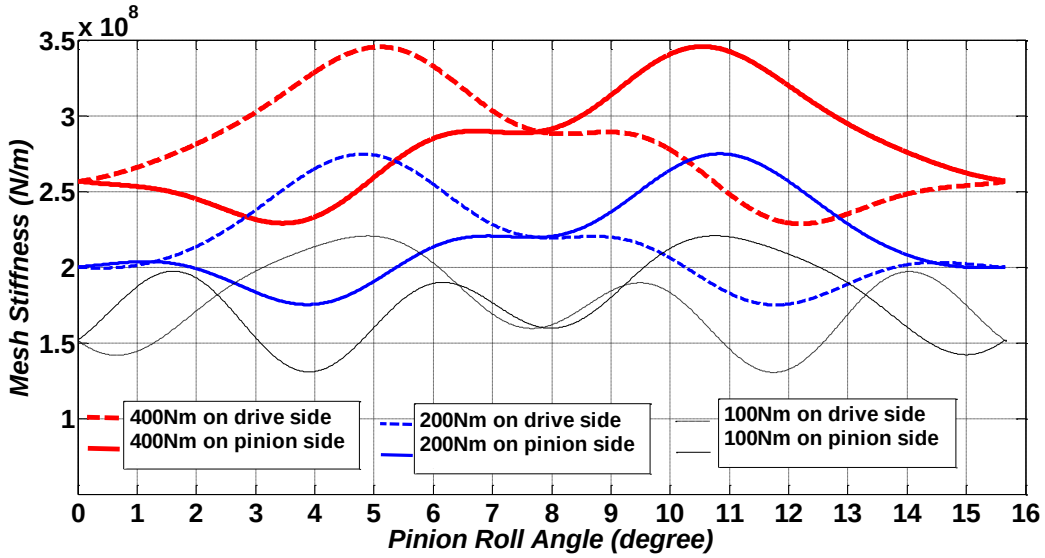

Fig. 2.26 Mesh stiffness variation under gear torque values for profile crowning

The mesh stiffness of the lengthwise crowning design is illustrated in Fig. 2.27 for drive and coast sides at different load torque values. Similar to the previous case, the mesh stiffness increases as the load torque grows.

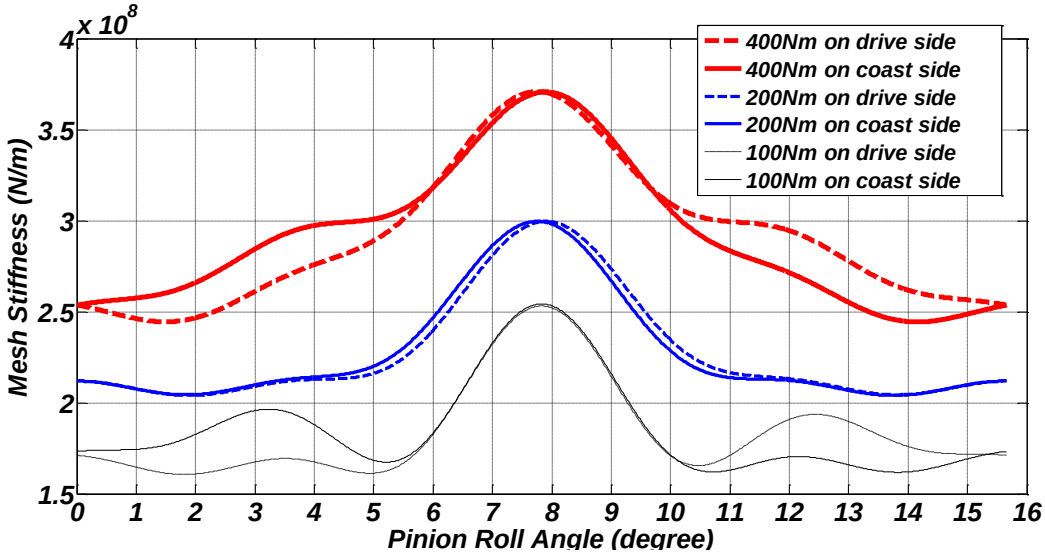

Fig. 2.27 Mesh stiffness variation under gear torque values for lengthwise crowning

The mesh stiffness of the flank twist crowning design for drive and coast sides are presented in Fig. 2.28 for different load torque levels. The mesh stiffness increases as the load grows in the flank twist case as well.

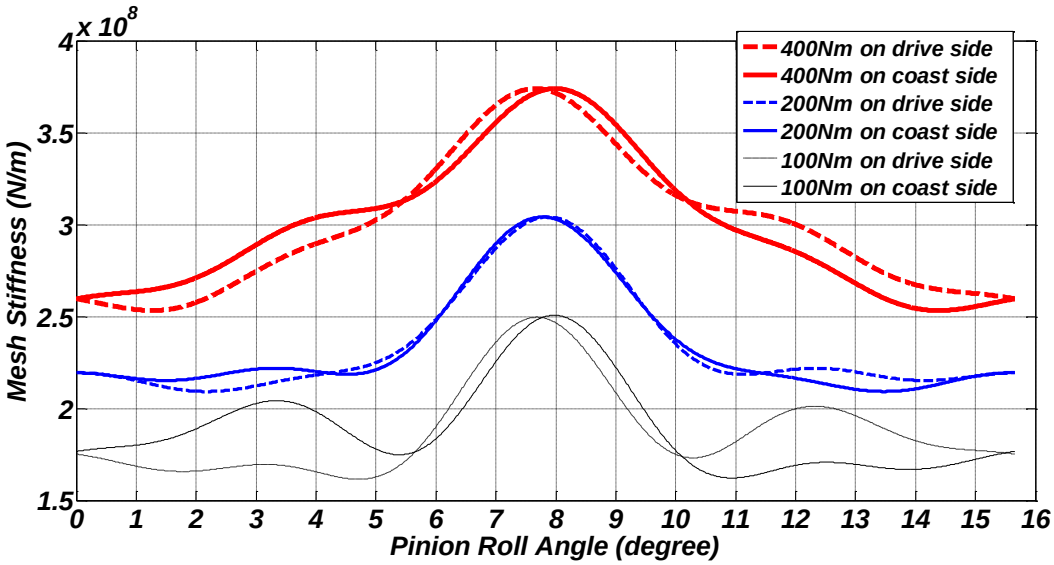

Fig. 2.28 Mesh stiffness variation under gear torque values for flank twist crowning

2.3 Discussion

It is clear from Fig. 2.12 and Fig. 2.13, edge contact is avoided under loaded conditions. However, it is not the only sufficient condition to make a judgement on the performance of the mesh and selected crowning type. Hence, as presented in the previous sections, the profile, lengthwise, flank twist crowning modifications all produce different effects on the directional rotation radius, STE, LTE and the mesh stiffness.

The directional rotation radius in all three modifications at 100Nm and 400Nm are shown in Fig. 2.29 for the drive side to have a better relative comparison between the different designs. The figure on the left and right presents 100Nm and 400Nm, respectively. At the lightly loaded conditions the contact path is distributed over a larger range towards the mean pitch diameter of the gears. As the load increase the path of contact narrows to the mean pitch diameter region. The effect of the load on the contact path is more on the profile crowned gear. At 100Nm torque profile modified gear shows the largest contact path distribution whereas at 400Nm the distribution and the value of the directional rotation radius reduces below lengthwise crowned gear. Flank twist shows the smallest directional rotation radius in all load levels. Hence, flank twist design has a more stable contact path nature compared to the other two modifications.

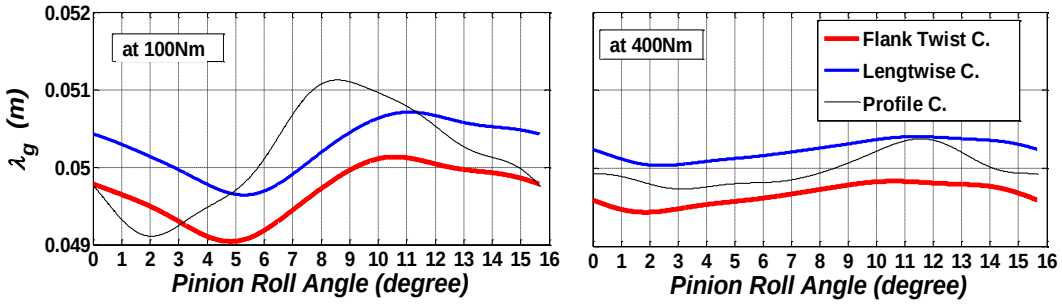

Fig. 2.29 Directional rotation radius variation under 100Nm and 400Nm gear torque values on drive side

STE change behavior of profile crowning is different than lengthwise and flank twist modifications, while lengthwise crowing gives considerably high transmission error in positive magnitudes. STE is in negative region approximately 19% of the one pitch mesh cycle in profile crowning and 50% in flank twist crowning design. The LTE for profile crowning and flank twist is always negative while lengthwise crowning stays at the positive values. The comparison of the LTE at 400Nm value for all three modifications are presented in Fig. 2.30 for the drive side. It is evident

that the profile and flank twist modifications are quite similar in magnitude even if the trend is slightly different. The general contact nature is close to each other as it can be reviewed in Fig. 2.8, Fig. 2.10 and Fig. 2.13. The contact area at the loaded operation of the lengthwise crowning is distributed in the center of the tooth as clearly evident from Fig. 2.9 and Fig. 2.30. Thus, the lengthwise modification in this particular design case presents the least desired properties when compared to profile and flank twist modifications from contact characteristics perspective.

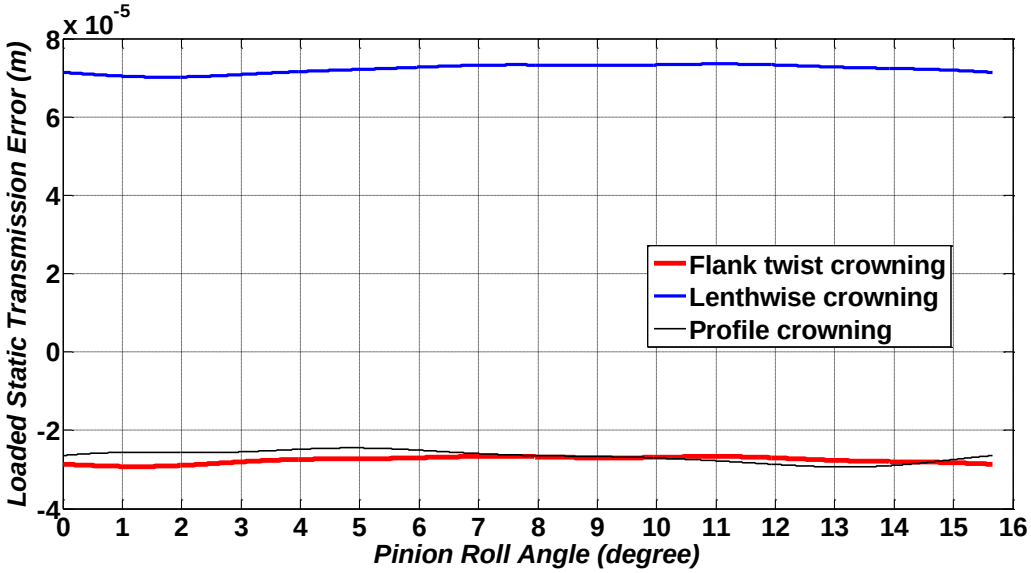

Fig. 2.30 LTE variation under 400Nm gear torque values for all modifications on drive side

The mesh stiffness is a load dependent feature as shown in the relevant figures where the increase in the load produces higher mesh stiffness. Even if the magnitude of lengthwise crowning is negative, due to the nature of Eq. (2.36), the stiffness is always positive, which means that the teeth are in compression as expected. Because, the contact area enlarges on tooth surface and produces a higher tooth contact ratio of the gear pair, which enables the mesh stiffening as the load increases. The comparison for 400Nm torque load for all three modification types are presented in Fig. 2.31 for the drive side. Lengthwise and flank twist crowning

designs show a very similar trend and magnitude while profile crowning shows relatively lower stiffness value. The effect on the shape of the mesh stiffness variation is dominated by the shape of STE. As a final remark, in combination with LTE, mesh stiffness and contact stress, the flank twist crowning is the most desirable case. Because of lower contact stress, stable contact path, low static and loaded transmission errors and high stiffness combination gives a promising design for dynamic evaluation.

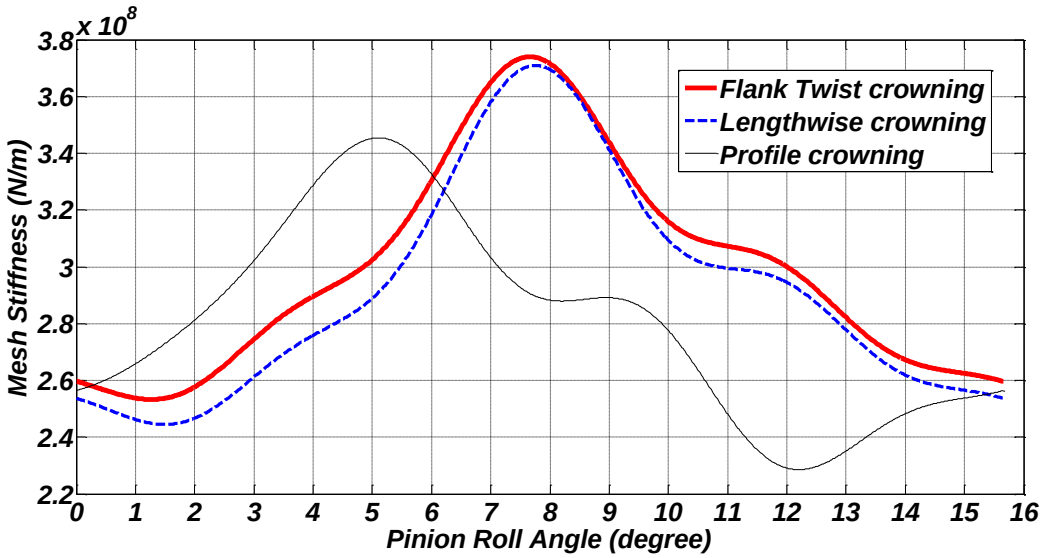

Fig. 2.31 Mesh stiffness variation under 400Nm gear torque values for all modifications

The gear mesh parameters are used in dynamic model are tabulated at Table 2.3, Table 2.4, Table 2.5 and Table 2.6. In dynamic model, transmission error of gear pair drive side is used and both drive and coast sides of gear pair are used for other mesh parameters.

Table 2.3 Transmission error of the example system

		Profile Crowning	**Flank Twist**	**Lengthwise Crowning**
µm	Term	Unloaded	Unloaded	Unloaded
e1	Mean	2.279	-0.326	99.99
e2	$\cos(\theta)$	1.933	3.396	3.83
e3	$\sin(\theta)$	-2.005	0.315	-0.44
e4	$\cos(2\theta)$	0.156	-0.727	-0.76
e5	$\sin(2\theta)$	0.46	0.265	0.48
e6	$\cos(3\theta)$	-0.244	0.496	0.57
e7	$\sin(3\theta)$	0.92	-0.154	-0.14
e8	$\cos(4\theta)$	0.593	-0.297	-0.34
e9	$\sin(4\theta)$	0.056	-0.023	-0.07

Table 2.4 Mesh stiffness of the example system

		Profile Crowning			**Flank Twist**			**Lengthwise Crowning**		
N/m ($x10^6$)	Term	100 Nm	200 Nm	400 Nm	100 Nm	200 Nm	400 Nm	100 Nm	200 Nm	400 Nm
kd1	Mean	176	217	280	188	234	300	184	228	292
kd2	$\cos(\theta)$	-7.6	-15.0	-24.5	-20.5	-32.0	-49.4	-23.1	-34.0	-49.8
kd3	$\sin(\theta)$	19.7	32.9	39.4	-10.2	-1.6	-5.0	-8.0	-1.6	-9.1
kd4	$\cos(2\theta)$	-7.8	-4.7	-3.1	15.3	21.3	10.4	17.4	21.2	13.2
kd5	$\sin(2\theta)$	-10.8	-8.5	-4.5	-6.4	-2.0	-4.7	-4.8	1.6	-4.5
kd6	$\cos(3\theta)$	3.3	5.2	8.2	-16.4	-10.4	-7.5	-17.9	-9.8	-8.7
kd7	$\sin(3\theta)$	-21.3	-11.1	-7.9	5.1	-0.3	2.2	1.4	-0.9	1.9
kd8	$\cos(4\theta)$	-12.9	-2.9	-5.0	9.0	6.2	6.4	10.5	6.6	7.0
kd9	$\sin(4\theta)$	-1.3	2.8	1.8	-0.9	1.8	-1.6	1.5	0.4	-0.7
kc2	$cos(\theta)$	-7.6	-15.0	-24.5	-20.1	-32.0	-49.4	-22.6	-34.0	-49.8
kc3	$sin(\theta)$	-19.5	-32.8	-39.4	11.0	1.6	5.0	8.7	1.6	9.1
kc4	$cos(2\theta)$	-7.8	-4.7	-3.0	15.0	21.3	10.4	17.2	21.2	13.2
kc5	$sin(2\theta)$	10.8	8.5	4.5	6.6	2.0	4.7	5.0	-1.6	4.5
kc6	$cos(3\theta)$	3.4	5.2	8.1	-16.6	-10.4	-7.5	-17.9	-9.8	-8.7
kc7	$sin(3\theta)$	21.3	11.2	8.0	-5.3	0.3	-2.2	-1.6	0.9	-1.9
kc8	$cos(4\theta)$	-12.9	-3.0	-5.0	9.1	6.2	6.4	10.7	6.6	7.0
kc9	$sin(4\theta)$	1.3	-2.7	-1.8	1.0	-1.8	1.6	-1.4	-0.4	0.7

Table 2.5 Pinion Radius of the example system

		Profile Crowning			**Flank Twist**			**Lengthwise Crowning**		
mm	Term	100 Nm	200 Nm	400 Nm	100 Nm	200 Nm	400 Nm	100 Nm	200 Nm	400 Nm
λ1	Mean	24.5	24.5	24.4	24.3	24.3	24.3	24.6	24.6	24.6
λd2	$\cos(\theta)$	-0.3	-0.1	0	0	0	0	0.1	0	0
λd3	$\sin(\theta)$	-0.3	-0.2	-0.1	-0.2	0.1	-0.1	-0.2	-0.1	-0.1
λd4	$\cos(2\theta)$	0.1	0	0	0	0	0	0	0	0
λd5	$\sin(2\theta)$	0	0.1	0	0	0	0	0	0	0
λd6	$\cos(3\theta)$	0	0	0	0	0	0	0	0	0
λd7	$\sin(3\theta)$	0	0	0	0	0	0	0	0	0
λd8	$\cos(4\theta)$	0	0	0	0	0	0	0	0	0
λd9	$\sin(4\theta)$	0	0	0	0	0	0	0	0	0
λc2	$cos(\theta)$	-0.3	-0.1	0	0	0	0	0.1	0	0
λc3	$sin(\theta)$	0.3	0.2	0.1	0.2	0.1	0.1	0.2	0.1	0.1
λc4	$cos(2\theta)$	0.1	0	0	0	0	0	0	0	0
λc5	$sin(2\theta)$	0	-0.1	0	0	0	0	-0.1	0	0
λc6	$cos(3\theta)$	0	0	0	0	0	0	0	0	0
λc7	$sin(3\theta)$	0	0	0	0	0	0	0	0	0
λc8	$cos(4\theta)$	0	0	0	0	0	0	0	0	0
λc9	$sin(4\theta)$	0	0	0	0	0	0	0	0	0

Table 2.6 Gear Radius of the example system

		Profile Crowning			**Flank Twist**			**Lengthwise Crowning**		
mm	Term	100 Nm	200 Nm	400 Nm	100 Nm	200 Nm	400 Nm	100 Nm	200 Nm	400 Nm
λ1	Mean	50.1	50.1	50	49.7	49.6	49.7	50.2	50.2	50.2
λd2	$\cos(\theta)$	-0.6	-0.3	0	0.1	0	-0.1	0.1	0.1	0
λd3	$\sin(\theta)$	-0.6	-0.5	-0.3	-0.5	-0.3	-0.2	-0.5	-0.3	-0.2
λd4	$\cos(2\theta)$	0.2	-0.1	-0.1	0.1	0	0	0	0	0
λd5	$\sin(2\theta)$	0	0.1	0	0.1	0	0	0.1	0	0
λd6	$\cos(3\theta)$	0	0	0	0	0	0	0	0	0
λd7	$\sin(3\theta)$	-0.1	-0.1	0	0	0	0	0	0	0
λd8	$\cos(4\theta)$	0.1	0	0	0	0	0	0	0	0
λd9	$\sin(4\theta)$	0	0	0	0	0	0	0	0	0
λc2	$cos(\theta)$	-0.6	-0.3	0	0.1	0	-0.1	0.1	0.1	0
λc3	$sin(\theta)$	-0.6	-0.5	-0.3	-0.5	-0.3	-0.2	-0.5	-0.3	-0.2
λc4	$cos(2\theta)$	0.2	-0.1	-0.1	0.1	0	0	0	0	0
λc5	$sin(2\theta)$	0	0.1	0	0.1	0	0	0.1	0	0
λc6	$cos(3\theta)$	0	0	0	0	0	0	0	0	0
λc7	$sin(3\theta)$	-0.1	-0.1	0	0	0	0	0	0	0
λc8	$cos(4\theta)$	0.1	0	0	0	0	0	0	0	0
λc9	$sin(4\theta)$	0	0	0	0	0	0	0	0	0

CHAPTER 3

DYNAMIC MODEL

3.1 Dynamic Model Formulation

A dynamic model simulating the vibration behavior of an actual spiral bevel gear pair is needed to make a final decision on a design of helicopter transmission drive system. In this study, a spiral bevel gear pair with a nonlinear time-varying dynamic model including backlash and asymmetric mesh effects is used by assuming rigidity for other components such as shaft, webs, bearings etc. 2-D torsional vibration model has also torsional rigidity for pinion shaft and gear web except for their utilization of the equivalent inertias on gear and pinion.

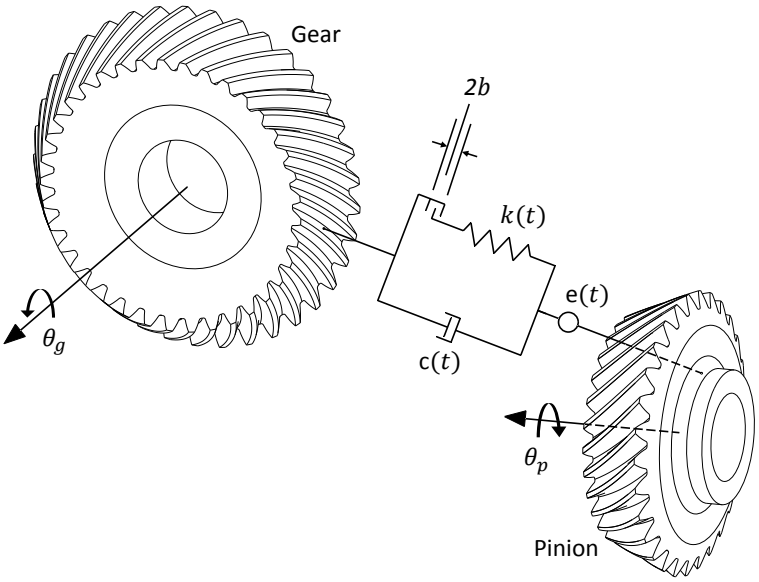

Fig. 3.1 Spiral bevel gear pair dynamic model

The model shown in Fig. 3.1 has asymmetric time-varying mesh stiffness and mesh damping, backlash and static transmission error along line of action. Rotation of pinion or gear relative to each other on tooth surface makes these parameters variable.

The equation of motion for the 2-DOF torsional vibration model can be written as [27, 28]

$$I_p\ddot{\theta}_p + \lambda_p(\delta)c(\delta)\left(\dot{\delta} - \dot{e}\right) + \lambda_p(\delta)k(\delta)f(\delta - e) = T_p \tag{3.1}$$

$$I_g\ddot{\theta}_g - \lambda_g(\delta)c(\delta)\left(\dot{\delta} - \dot{e}\right) - \lambda_g(\delta)k(\delta)f(\delta - e) = -T_g \tag{3.2}$$

where I_p and I_g are the mass moments of inertia of pinion and gear, respectively. T_p and T_g are the torque applied on pinion and gear. δ is the dynamic transmission error. In Eq. (3.1) and (3.2), stiffness $k(\delta)$, damping $c(\delta)$, directional rotation radius of pinion and gear, $\lambda_p(\delta)$ & $\lambda_g(\delta)$ are asymmetric and time-varying.

$$\lambda_p(\delta) = \begin{cases} \lambda_{pd}, & \delta \geq 0 \\ \lambda_{pc}, & \delta < 0 \end{cases} \tag{3.3}$$

$$\lambda_g(\delta) = \begin{cases} \lambda_{gd}, & \delta \geq 0 \\ \lambda_{gc}, & \delta < 0 \end{cases} \tag{3.4}$$

$$\lambda_{pd} = \lambda_{pd_1} + \sum_{l=1}^{L}\left(\lambda_{pd_{(2l)}}\cos(l\omega t) + \lambda_{pd_{(2l+1)}}\sin(l\omega t)\right) \tag{3.5}$$

$$\lambda_{pc} = \lambda_{pc_1} + \sum_{m=1}^{M}\left(\lambda_{pc_{(2m)}}\cos(m\omega t) + \lambda_{pc_{(2m+1)}}\sin(m\omega t)\right) \tag{3.6}$$

$$\lambda_{gd} = \lambda_{gd_1} + \sum_{u=1}^{U}\left(\lambda_{gd_{(2u)}}\cos(u\omega t) + \lambda_{gd_{(2u+1)}}\sin(u\omega t)\right) \tag{3.7}$$

$$\lambda_{gc} = \lambda_{gc_1} + \sum_{v=1}^{V} (\lambda_{gc_{(2v)}} \cos(v\omega t) + \lambda_{gc_{(2v+1)}} \sin(v\omega t)) \tag{3.8}$$

Asymmetric and time-varying mesh stiffness, mesh damping and dynamic transmission error, δ, are defined as

$$\delta = \lambda_p(\delta)\theta_p - \lambda_g(\delta)\theta_g \tag{3.9}$$

$$k(\delta) = \begin{cases} k_d, & \delta \geq 0 \\ k_c, & \delta < 0 \end{cases} \tag{3.10}$$

$$c(\delta) = \begin{cases} c_d, & \delta \geq 0 \\ c_c, & \delta < 0 \end{cases} \tag{3.11}$$

$$k_d = k_{d_1} + \sum_{a=1}^{A} (k_{d_{(2a)}} cos(a\omega t) + k_{d_{(2a+1)}} sin(a\omega t)) \tag{3.12}$$

$$k_c = k_{c_1} + \sum_{b=1}^{B} (k_{c_{(2b)}} cos(b\omega t) + k_{c_{(2b+1)}} sin(b\omega t)) \tag{3.13}$$

$$c_d = c_{d_1} + \sum_{d=1}^{D} (c_{d_{(2d)}} cos(d\omega t) + c_{d_{(2d+1)}} sin(d\omega t)) \tag{3.14}$$

$$c_c = c_{c_1} + \sum_{e=1}^{E} (c_{c_{(2e)}} cos(e\omega t) + c_{c_{(2e+1)}} sin(e\omega t)) \tag{3.15}$$

Nonlinear displacement function, $f(\delta - e)$, in Eq. (3.1) and (3.2) can be written as

$$f(\delta - e) = \begin{cases} \delta - e - b, & \delta - e \geq b \\ 0, & -b < \delta - e < b \\ \delta - e + b, & \delta - e \leq -b \end{cases} \tag{3.16}$$

Here, b denotes the half of the gear backlash, which is 40 micron in this study.

The static transmission error, e, which can be defined as displacement of a driven gear with respect to its theoretical uniform displacement as a pair of contacting gear teeth. It can be considered as periodic and can be represented as a Fourier series given in Eq. (3.17).

$$e = \sum_{g=1}^{G} (e_{(2g)}\, cos(g\omega t) + e_{(2g+1)}\, sin(g\omega t)) \tag{3.17}$$

This 2-DOF semi-definite system, where the generalized coordinates are θ_p and θ_g, is reduced to a single-degree-of-freedom (SDOF) definite system with the generalized coordinate, x. Let $x = \delta - e$, Eq. (3.1) and (3.2) is combined into the following single equation of motion:

$$m_e(\delta)\ddot{x} + c(\delta)\dot{x} + k(\delta)f(x) = m_e(\delta)\left(\frac{\lambda_p(\delta)T_p}{I_p} + \frac{\lambda_g(\delta)T_g}{I_g} - \ddot{e}\right) \tag{3.18}$$

$$m_e(\delta) = \begin{cases} m_{ed}, & \delta \geq 0 \\ m_e c, & \delta < 0 \end{cases} \tag{3.19}$$

$$m_{ed} = 1/\left(\lambda_{pd}^2/I_p + \lambda_{gd}^2/I_g\right) \tag{3.20}$$

$$m_{ec} = 1/\left(\lambda_{pc}^2/I_p + \lambda_{gc}^2/I_g\right) \tag{3.21}$$

$$f(x) = \begin{cases} x - b, & x \geq b \\ 0, & -b < x < b \\ x + b, & x \leq -b \end{cases} \tag{3.22}$$

For simplifications, $\dot{\lambda}_{lm}$ and $\ddot{\lambda}_{lm}$ are taken as zero, which is a reasonable assumption since the mesh point and line of action are typically continuous with little change in time as explained in 2.2.2 Application of the Mesh Stiffness Model. 2.2.2

By considering Eq. (3.20) for bias term and $\omega_n = \sqrt{k_{d_1}/m_{ed1}}$ and with the following transformations, the dimensionless equation of motion can be derived:

$$\tilde{x} = x/b \tag{3.23}$$

$$\tilde{t} = \omega_n t \tag{3.24}$$

$$\tilde{\omega} = \omega/\omega_n \tag{3.25}$$

$$\tilde{k}_d = k_d/k_{d_1} = 1 + \sum_{a=1}^{A} (\tilde{k}_{d_{(2a)}} \cos(a\tilde{\omega}\tilde{t}) + \tilde{k}_{d_{(2a+1)}} \sin(a\tilde{\omega}\tilde{t})) \tag{3.26}$$

$$\tilde{k}_c = k_c/k_{c_1} = 1 + \sum_{b=1}^{B} (\tilde{k}_{c_{(2b)}} \cos(b\tilde{\omega}\tilde{t}) + \tilde{k}_{c_{(2b+1)}} \sin(b\tilde{\omega}\tilde{t})) \tag{3.27}$$

$$\tilde{c}_d = c_d/c_{d_1} = 1 + \sum_{d=1}^{D} (\tilde{c}_{d_{(2d)}} \cos(d\tilde{\omega}\tilde{t}) + \tilde{c}_{d_{(2d+1)}} \sin(d\tilde{\omega}\tilde{t})) \tag{3.28}$$

$$\tilde{c}_c = c_c/c_{c_1} = 1 + \sum_{e=1}^{E} (\tilde{c}_{c_{(2e)}} \cos(e\tilde{\omega}\tilde{t}) + \tilde{c}_{c_{(2e+1)}} \sin(e\tilde{\omega}\tilde{t})) \tag{3.29}$$

$$\tilde{e} = e/b = \sum_{g=1}^{G} (\tilde{e}_{(2g)} \cos(g\tilde{\omega}\tilde{t}) + \tilde{e}_{(2g+1)} \sin(g\tilde{\omega}\tilde{t})) \tag{3.30}$$

$$\tilde{\lambda}_{pd} = \lambda_{pd}/\lambda_{pd_1} = 1 + \sum_{h=1}^{H} (\tilde{\lambda}_{pd_{(2h)}} \cos(h\tilde{\omega}\tilde{t}) + \tilde{\lambda}_{pd_{(2h+1)}} \sin(h\tilde{\omega}\tilde{t})) \tag{3.31}$$

$$\tilde{\lambda}_{pc} = \lambda_{pc}/\lambda_{pc_1} = 1 + \sum_{j=1}^{J} (\tilde{\lambda}_{pc_{(2j)}} \cos(j\tilde{\omega}\tilde{t}) + \tilde{\lambda}_{pc_{(2j+1)}} \sin(j\tilde{\omega}\tilde{t})) \tag{3.32}$$

$$\tilde{\lambda}_{gd} = \lambda_{gd}/\lambda_{gd_1} = 1 + \sum_{k=1}^{K} (\tilde{\lambda}_{gd_{(2k)}} \cos(k\tilde{\omega}\tilde{t}) + \tilde{\lambda}_{gd_{(2k+1)}} \sin(k\tilde{\omega}\tilde{t})) \tag{3.33}$$

$$\tilde{\lambda}_{gc} = \lambda_{gc}/\lambda_{gc_1} = 1 + \sum_{l=1}^{L} (\tilde{\lambda}_{gc_{(2l)}} \cos(l\tilde{\omega}\tilde{t}) + \tilde{\lambda}_{gc_{(2l+1)}} \sin(l\tilde{\omega}\tilde{t})) \quad (3.34)$$

Then, the simplified dimensionless equation of motion can be written as

$$\tilde{x}'' + 2\zeta c(\tilde{x}) g(\tilde{x}) \tilde{x}' + \frac{g(\tilde{x})}{1+\sigma} k(\tilde{x}) f(\tilde{x}) = \tilde{T}_p \tilde{\lambda}_p(\tilde{x}) + \tilde{T}_g \tilde{\lambda}_g(\tilde{x}) - \tilde{e}'' \quad (3.35)$$

where the parameters in the above equation are given by

$$\zeta = \frac{\lambda_{pd1}^2 c_{d_1}}{2 I_p \omega_n} \quad (3.36)$$

$$\sigma = \frac{\lambda_{gd1}^2 I_p}{\lambda_{pd1}^2 I_g} \quad (3.37)$$

$$\tilde{T}_p = \frac{\lambda_{pd_1} T_p}{b \omega_n^2 I_p} \quad (3.38)$$

$$\tilde{T}_g = \sigma \tilde{T}_p \quad (3.39)$$

$$c(\tilde{x}) = \begin{cases} \tilde{c}_d, & \tilde{x} \geq 1 \\ r_{da} \tilde{c}_c, & \tilde{x} < 1 \end{cases} \quad (3.40)$$

$$r_{da} = \frac{c_{c_1}}{c_{d_1}} \quad (3.41)$$

$$k(\tilde{x}) = \begin{cases} \tilde{k}_d, & \tilde{x} \geq 1 \\ r_k \tilde{k}_c, & \tilde{x} < 1 \end{cases} \quad (3.42)$$

$$r_k = \frac{k_{c_1}}{k_{d_1}} \quad (3.43)$$

$$f(\tilde{x}) = \begin{cases} \tilde{x} - 1, & \tilde{x} \geq 1 \\ 0, & -1 < \tilde{x} < 1 \\ \tilde{x} + 1, & \tilde{x} \leq -1 \end{cases} \quad (3.44)$$

$$g(\tilde{x}) = \begin{cases} \tilde{\lambda}_{pd}^2 + \sigma\tilde{\lambda}_{gd}^2, & \tilde{x} \geq 0 \\ r_p^2\tilde{\lambda}_{pc}^2 + \sigma r_g^2\tilde{\lambda}_{gc}^2, & \tilde{x} < 0 \end{cases} \tag{3.45}$$

$$\tilde{\lambda}_p(\tilde{x}) = \begin{cases} \tilde{\lambda}_{pd}, & \tilde{x} \geq 0 \\ r_p\tilde{\lambda}_{pc}, & \tilde{x} < 0 \end{cases} \tag{3.46}$$

$$\tilde{\lambda}_g(\tilde{x}) = \begin{cases} \tilde{\lambda}_{gd}, & \tilde{x} \geq 0 \\ r_g\tilde{\lambda}_{gc}, & \tilde{x} < 0 \end{cases} \tag{3.47}$$

$$r_p = \frac{\lambda_{pc_1}}{\lambda_{pd_1}} \tag{3.48}$$

$$r_g = \frac{\lambda_{gc_1}}{\lambda_{gd_1}} \tag{3.49}$$

3.2 Harmonic Balance Method

By using multi-term Harmonic Balance Method coupled with discrete Fourier Transform, which has been successfully applied in [29, 35], nonlinear equations of motion for x is solved. Since the static transmission error, mesh stiffness and mesh damping are periodic in time, the steady state solution, $\tilde{x}$, must also be periodic [29]. This implies that the nonlinear displacement function, $f(\tilde{x})$, can also be described periodically.

Thus, the steady state solution is assumed to be of the form

$$\tilde{x}(\tilde{t}) = \tilde{x}_1 + \sum_{m=1}^{M} (\tilde{x}_{(2\boldsymbol{m})}\cos(m\tilde{\omega}\tilde{t}) + \tilde{x}_{(2\boldsymbol{m}+1)}\sin(m\tilde{\omega}\tilde{t})) \tag{3.50}$$

Similarly, damping force, nonlinear restoring force and external excitation forces can be represented as Fourier series with multi harmonics as follows:

$$F_{\boldsymbol{c}}(\tilde{t}) = F_{\boldsymbol{c}_1} + \sum_{m=1}^{M} \left(F_{\boldsymbol{c}_{(2\boldsymbol{m})}} \cos(m\tilde{\omega}\tilde{t}) + F_{\boldsymbol{c}_{(2\boldsymbol{m}+1)}} \sin(m\tilde{\omega}\tilde{t})\right) \tag{3.51}$$

$$F_k(\tilde{t}) = F_{k_1} + \sum_{m=1}^{M} \left(F_{k_{(2m)}} \cos(m\tilde{\omega}\tilde{t}) + F_{k_{(2m+1)}} \sin(m\tilde{\omega}\tilde{t})\right) \tag{3.52}$$

$$F_p(\tilde{t}) = F_{p_1} + \sum_{m=1}^{M} \left(F_{p_{(2m)}} \cos(m\tilde{\omega}\tilde{t}) + F_{p_{(2m+1)}} \sin(m\tilde{\omega}\tilde{t})\right) \tag{3.53}$$

$$F_g(\tilde{t}) = F_{g_1} + \sum_{m=1}^{M} \left(F_{g_{(2m)}} \cos(m\tilde{\omega}\tilde{t}) + F_{g_{(2m+1)}} \sin(m\tilde{\omega}\tilde{t})\right) \tag{3.54}$$

where the Fourier coefficients of each series can be calculated by making the use of discrete Fourier Transform (DFT). The values of these forces at the discrete time $\tilde{t}_n = nh$ are as follows ($n \in [0, \mathrm{N}-1]$ and $h = 2\pi/(N\tilde{\omega})$

$$F_{\boldsymbol{c}}(\tilde{t}_n) = 2\zeta c\big(\tilde{x}(\tilde{t}_n)\big) g\big(\tilde{x}(\tilde{t}_n)\big) \tilde{x}'(\tilde{t}_n) \tag{3.55}$$

$$F_k(\tilde{t}_n) = \frac{g\big(\tilde{x}(\tilde{t}_n)\big)}{1+\sigma} k\big(\tilde{x}(\tilde{t}_n)\big) f\big(\tilde{x}(\tilde{t}_n)\big) \tag{3.56}$$

$$F_p(\tilde{t}) = \tilde{T}_p \tilde{\lambda}_p\big(\tilde{x}(\tilde{t}_n)\big) \tag{3.57}$$

$$F_g(\tilde{t}) = \tilde{T}_g \tilde{\lambda}_g\big(\tilde{x}(\tilde{t}_n)\big) \tag{3.58}$$

where total number of the discrete points, N must be larger than twice times of highest harmonic number R, in order not to have aliasing errors. The Fourier coefficients of these forces, F_u ($u = c, k, p, g$ for damping force, nonlinear restoring force, and external excitation forces on the pinion and gear, respectively) are determined by employing the inverse DFT equations:

$$F_{u_1} = \frac{1}{N}\sum_{n=0}^{N-1} F_u(\tilde{t}_n) \tag{3.59}$$

$$F_{u_{(2r)}} = \frac{2}{N}\sum_{n=0}^{N-1} F_u(\tilde{t}_n)\, cos(2\pi rn/N) \tag{3.60}$$

$$F_{u_{(2r+1)}} = \frac{2}{N}\sum_{n=0}^{N-1} F_u(\tilde{t}_n)\, \sin(2\pi rn/N) \tag{3.61}$$

By substituting equations Eq.(3.17) and Eq.(3.50) - Eq.(3.58) into Eq.(3.14) and equating the coefficients of like harmonic terms, a set of $2R + 1$ nonlinear algebraic equations can be obtained, which can be written in vector form as

$$S\left(F_c, F_k, F_p, F_g, \tilde{\omega}\right) = 0 \tag{3.62}$$

where the elements of S are given as ($r \in [1, \mathrm{R}]$)

$$S_1 = F_{c_1} + F_{k_1} - F_{p_1} - F_{g_1} \tag{3.63}$$

$$\begin{aligned} S_{(2r)} = &-(r\tilde{\omega})^2\tilde{x}_{(2r)} + F_{c_{(2r)}} + F_{k_{(2r)}} - F_{p_{(2r)}} - F_{g_{(2r)}} \\ &- (r\tilde{\omega})^2\tilde{e}_{(2r)} \end{aligned} \tag{3.64}$$

$$\begin{aligned} S_{(2r+1)} = &-(r\tilde{\omega})^2\tilde{x}_{(2r+1)} + F_{c_{(2r+1)}} + F_{k_{(2r+1)}} - F_{p_{(2r+1)}} \\ &- F_{g_{(2r+1)}} - (r\tilde{\omega})^2\tilde{e}_{(2r+1)} \end{aligned} \tag{3.65}$$

Eq. (3.63) is related to the bias term while Eq. (3.64) and (3.65) are the equation including the sine and cosine terms of the r^{th} harmonic.

3.3 Solution of Nonlinear Algebraic Equations

In steady-state vibration analysis of a system with nonlinear elements, nonlinear differential equations of motion are converted into a set of nonlinear algebraic equations as explained in the previous section. Hence, nonlinear algebraic equations are solved in order to obtain the vibratory characteristics of the nonlinear system.

The set of nonlinear algebraic equations given by Eqs. (3.63)-(3.65) is solved by Newton's Method, which is given by Eq. (3.66), for the unknown displacement vector $\tilde{x} = [\tilde{x}_1\ \tilde{x}_2 \cdots \tilde{x}_{2R+1}]^T$.

$$\tilde{x}^{(m)} = \tilde{x}^{(m-1)} - [J^{-1}]^{(m-1)} S^{(m-1)} \tag{3.66}$$

Here $\tilde{x}^{(m)}$ is the mth iterative solution based on (m-1)$^{\text{th}}$ solution and J^{-1} is the inverse of the Jacobian matrix. The iteration procedure described by Eq. (3.66) is repeated until the vector norm of $S^{(m)}$ is below a predefined error limit for that excitation frequency. Moreover, arc-length continuation method is used in the solution and a new parameter, arc-length, is chosen as the continuation parameter instead of the frequency in order to follow the path even at the turning points. Details of Newton's with arc-length continuation are found in [36], [37] and [38].

The stability of the steady state solution $\tilde{x}(\tilde{t})$ can be determined by examining the stability of the perturbed solution $\tilde{x}(\tilde{t}) + \Delta\tilde{x}(\tilde{t})$ using Floquet theory. The variational equation for the perturbation $\Delta\tilde{x}(\tilde{t})$ is

$$\Delta\tilde{x}(\tilde{t})'' + 2\zeta c(\tilde{x}(\tilde{t}))g(\tilde{x}(\tilde{t}))\Delta\tilde{x}(\tilde{t})' + \frac{g(\tilde{x}(\tilde{t}))}{1+\sigma} k(\tilde{x}(\tilde{t}))\phi(\tilde{t})\Delta\tilde{x}(\tilde{t}) = 0 \tag{3.67}$$

where $\phi(\tilde{t})$ is a discontinuous separation function

$$\phi(\tilde{t}) = \begin{cases} 1, & |\tilde{x}(\tilde{t})| > 1 \\ 0, & |\tilde{x}(\tilde{t})| \leq 1 \end{cases} \tag{3.68}$$

The Eq. (3.67) can be written in state-space form $z(\tilde{t})' = G(\tilde{t})z(\tilde{t})$ where $z(\tilde{t}) = [\Delta\tilde{x}(\tilde{t}) \quad \Delta\tilde{x}(\tilde{t})']^T$ is the state vector and $G(\tilde{t}) = G(\tilde{t} + T)$ is the periodic state matrix given by [39]

$$G(\tilde{t}) = \begin{bmatrix} 0 & 1 \\ -\dfrac{g(\tilde{x}(\tilde{t}))}{1+\sigma} k(\tilde{x}(\tilde{t}))\phi(\tilde{t}) & -2\zeta c(\tilde{x}(\tilde{t}))g(\tilde{x}(\tilde{t})) \end{bmatrix} \tag{3.69}$$

Then, the monodromy matrix, $M = z(T)$ is defined as the state transition matrix at the end of one analysis period, which is obtained by solving the homogenous matrix equation $z(\tilde{t})' = G(\tilde{t})z(\tilde{t})$ given initial condition $z(0) = I_2$, and the stability of the perturbed solution and consequently the stability of the corresponding solution $\tilde{x}(\tilde{t})$ are determined by examining the eigenvalues of this matrix. Here I_2 is $2x2$ identity matrix [39]. M is again computed with a method that is based on an assumed stepwise variation of the state transition matrix. The state matrix $G(\tilde{t})$ is approximated as a series of step functions G_n at N discrete time intervals $\tau = nh$ as follows [39]

$$G_n = \frac{1}{h} \int_{(n-1)h}^{nh} G(\tau)\, d\tau \qquad n \in [1, N] \tag{3.70}$$

If large number of time steps N is used, $G(\tilde{t})$ can be considered constant between two consecutive time steps and the integration is not needed. Between these two time instants, the following relation, where the exponential term is the state transition matrix, can be written [40]

$$z_{n+1} = e^{hG_n} z_n \tag{3.71}$$

Then, the monodromy matrix is computed as the product of the individual transition matrices [19]:

$$z_N = \prod_{n=0}^{N-1} e^{hG_n} z_0 = M z_0 \tag{3.72}$$

$$M = \prod_{n=0}^{N-1} e^{hG_n} \tag{3.73}$$

Here, Pade approximation is used in MATLAB via *"expm"* command for matrix exponentiation. Then, the complex eigenvalues λ_1 and λ_2 of M, which are called Floquet multipliers, are calculated and if the modulus of either λ_1 or λ_2 is greater than unity, the solution $q(t)$ is unstable.

3.4 Results and Discussion

The equation of motion given in Eq. (3.35) is solved by both harmonic balance method (HBM) and numerical integration (NI). Using HBM solution, RMS values of dynamic displacements, u_{rms}, which is normalized with respect to backlash of gear pair, are obtained. u_{rms} is the root-mean-square (RMS) amplitude of the alternating component of $\tilde{x}(\tilde{t})$ and given in Eq. (3.74)

$$u_{rms} = \sqrt{\sum_{r=1}^{R} {A_r}^2} \tag{3.74}$$

$$A_r = \sqrt{{u_{2r}}^2 + {u_{2r+1}}^2} \tag{3.75}$$

where A_r is the amplitude of the r[th] harmonic obtained by HBM.

For NI solution, MATLAB *"ode45"* solver, which is based on an explicit 4^{th}-5^{th} order Runge-Kutta method, is used. In this method, the number of cycles for the solution to reach steady-state depends on damping, initial conditions etc. Therefore, ensuring the solution to reach steady-state, a constant number of cycles specified according to the initial runs is used for whole frequency range. As seen from Fig. 3.2, numerical integration solution is matched with stable HBM solution up to $\tilde{\omega} = 0.45$, and has a jump at this frequency. The reason behind that single-sided tooth impact region starts at $\tilde{\omega} = 0.56$. In other words, tooth separation begins to happen and response continues to emerge. Meanwhile, HBM solution shows that the response curve bends left towards lower frequency up to close to jump frequency for NI solution due to the softening-type nonlinear behavior of the backlash. At this region, then response curve changes its direction continues to increase with frequency up to $\tilde{\omega} = 0.75$ and maximum value of itself. In this case, the backlash nonlinearity behaves as a hardening spring because of the additional impact with the preceding tooth, which is called as double-sided tooth impact.

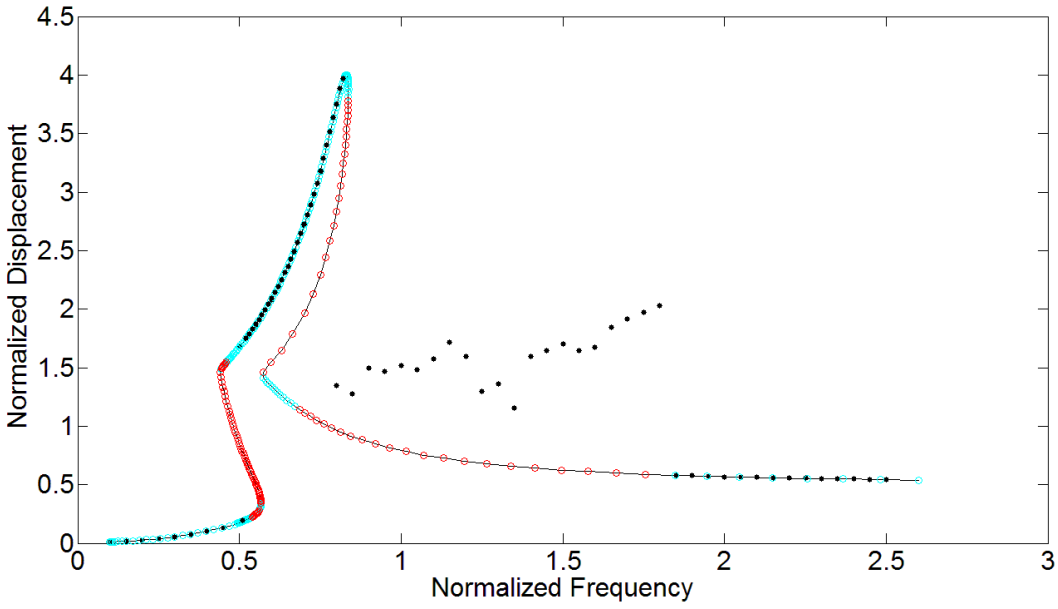

Fig. 3.2 Comparison of u_{rms} components of HBM (**o** stable, **o** unstable) and NI (·) solutions

Here, NI solution is again coincident with stable HBM solution. NI solution is different than solution of HBM at frequencies between $\tilde{\omega} = 0.75$ and $\tilde{\omega} = 1.8$**.** In these regions, multiple solutions coexist depending on the initial conditions; so this region are unstable. Moreover, by incorporating the sub-harmonic motions into the solution, HBM solution matching with the NI solution in that region. Fig. 3.3 shows the RMS of the dynamic response including the period-2 ($2T$) and period-3 ($3T$) motions. For period-β (βT) motion, the response $\tilde{x}(\tilde{t})$ is represented in Fourier series as follows:

$$\tilde{x}(\tilde{t}) = \tilde{x}_1 + \sum_{m=1}^{M} (\tilde{x}_{(2\boldsymbol{m})} \cos\left(\frac{m}{\beta}\tilde{\omega}\tilde{t}\right) + \tilde{x}_{(2\boldsymbol{m}+1)} \sin\left(\frac{m}{\beta}\tilde{\omega}\tilde{t}\right)) \qquad (3.76)$$

where β is the subharmonic index. For period-2 ($2T$) motion, $\beta = 2$ and the response consists of the harmonics with the frequencies $\tilde{\omega}/2$, $2\tilde{\omega}/2$, $3\tilde{\omega}/2$, $4\tilde{\omega}/2 \cdots$. The period of the response in this case is $2 \times (2\pi/\tilde{\omega})$. Therefore, the motion described by such a response is referred as period-2 ($2T$) motion. On the other hand, for period-3 ($3T$) motion ($\beta = 3$), the response consists of the harmonics with the frequencies $\tilde{\omega}/3$, $\widetilde{2\omega}/3$, $3\tilde{\omega}/3$, $4\tilde{\omega}/3 \cdots$, and the period of the response is $3 \times (2\pi/\tilde{\omega})$. Therefore, the motion described by such a response is referred as period-3 ($3T$) motion. In general, the period of the response consisting of the subharmonics with the index of β is $\beta \times (2\pi/\tilde{\omega})$.

Consequently, the NI solution may converge to primary and sub-harmonic motions in the multi-valued regions depending on the initial conditions. HBM solution captures NI solution for $\tilde{\omega} = 1.8$ and higher frequencies when solution is stable as shown also in Fig. 3.2 and Fig. 3.3. By considering this comparison, sub-harmonic motions and stability analysis are not used for the rest of this study when comparing responses of spiral bevel gears with different tooth flank modifications.

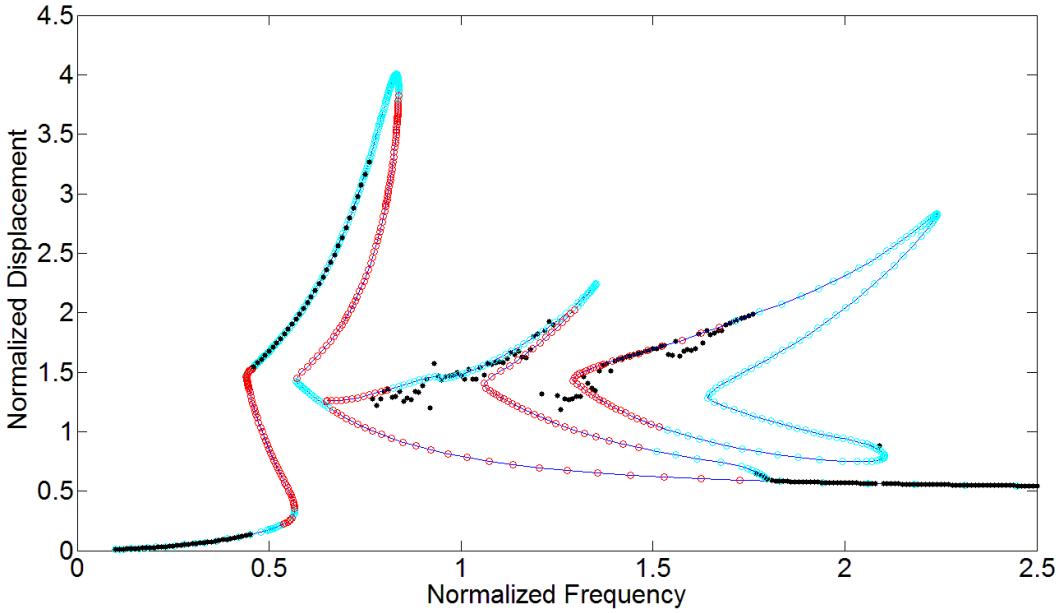

Fig. 3.3 Comparison of u_{rms} components of HBM (**o** stable, **o** unstable) and NI (·) solutions

Firstly, for spiral bevel gear with flank twist modifications, Fig. 3.4 shows that u_{rms}values of dynamic displacements vs. normalized frequency with respect to natural frequency under different load conditions. In addition to primary resonance peaks, 2nd, 3rd and 4th super-harmonic resonance peaks are also seen in Fig. 3.4. The peak behavior of super-harmonic responses are different than that of resonance response during different torque values, which results from harmonic amplitudes of mesh parameters shown in Fig. 3.5, Fig. 3.6, Fig. 3.7 and Fig. 3.8.

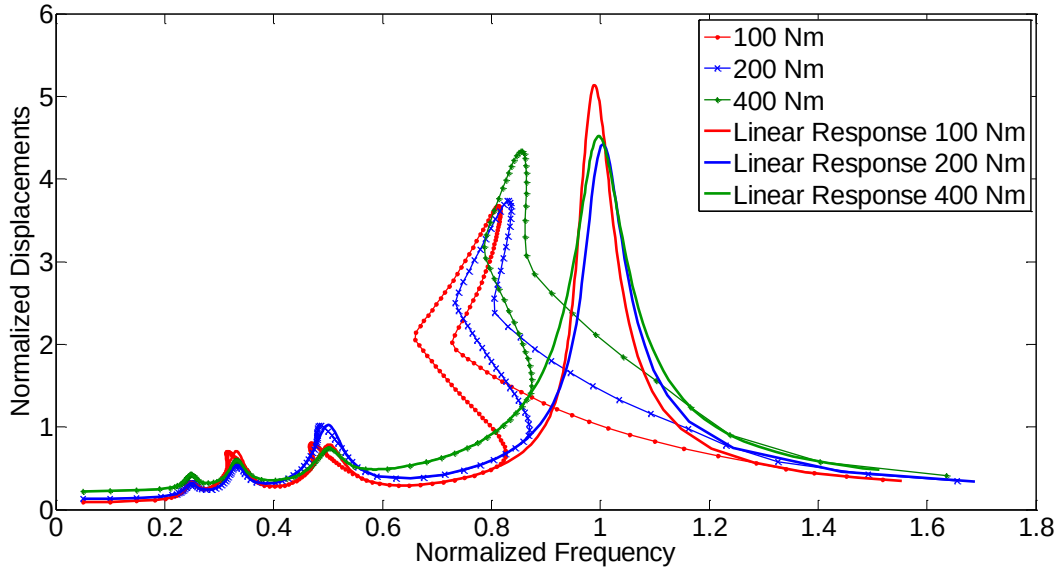

Fig. 3.4 RMS values of dynamic torsional displacements for FT

First mesh harmonics are more dominant than other mesh harmonics for static transmission error and directional rotational radii. However, as shown in Fig. 3.5, first mesh harmonic of mesh stiffness has slightly larger than other mesh harmonics at light load and it starts to dominate much more than others when gear pair are under higher loads.

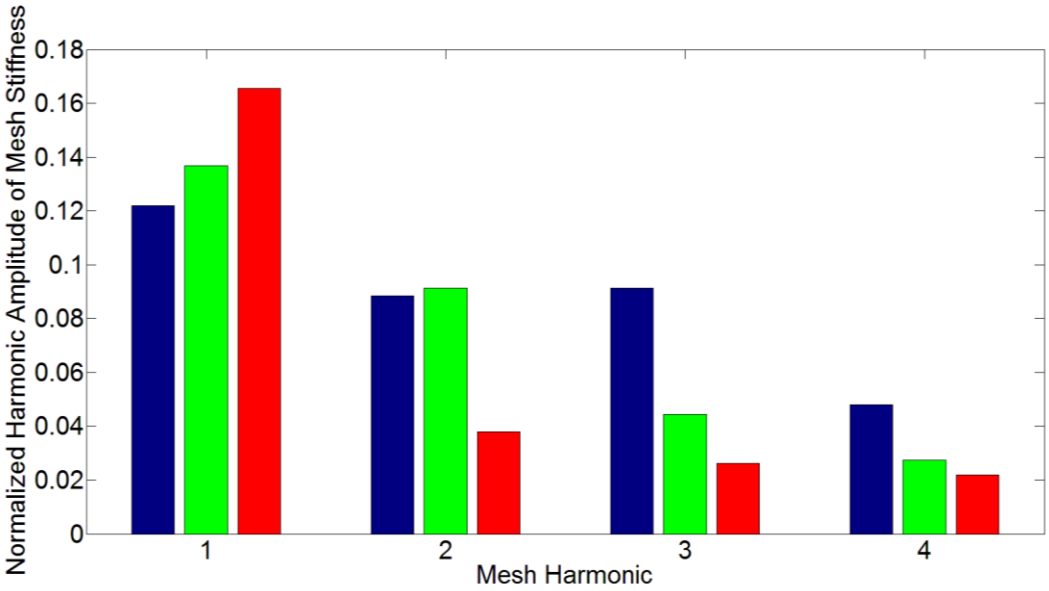

Fig. 3.5 Normalized Harmonic Amplitudes of Mesh Stiffness for FT

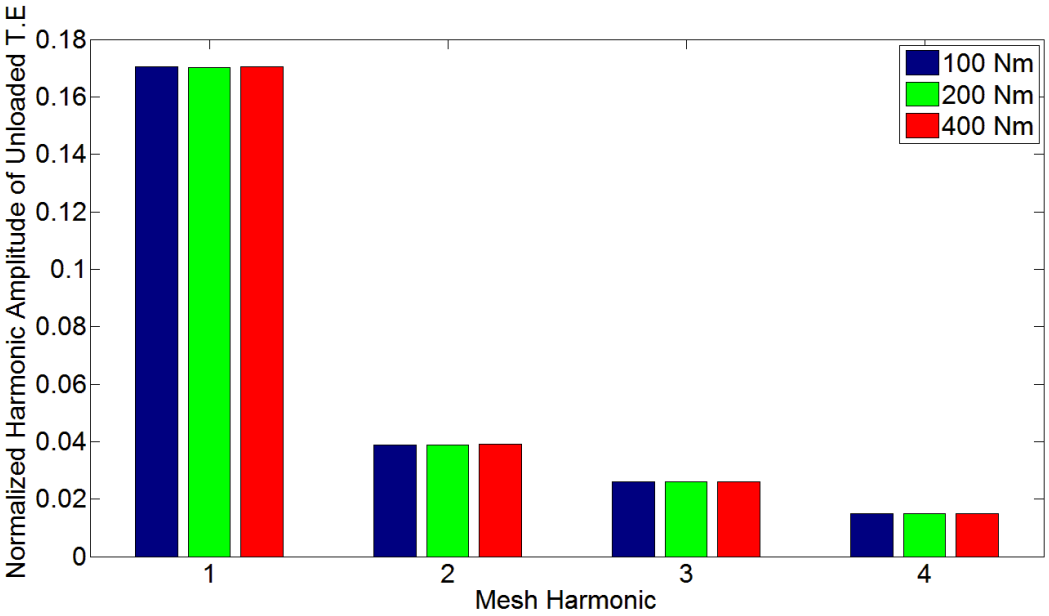

Fig. 3.6 Normalized Harmonic Amplitudes of Unloaded T.E for FT

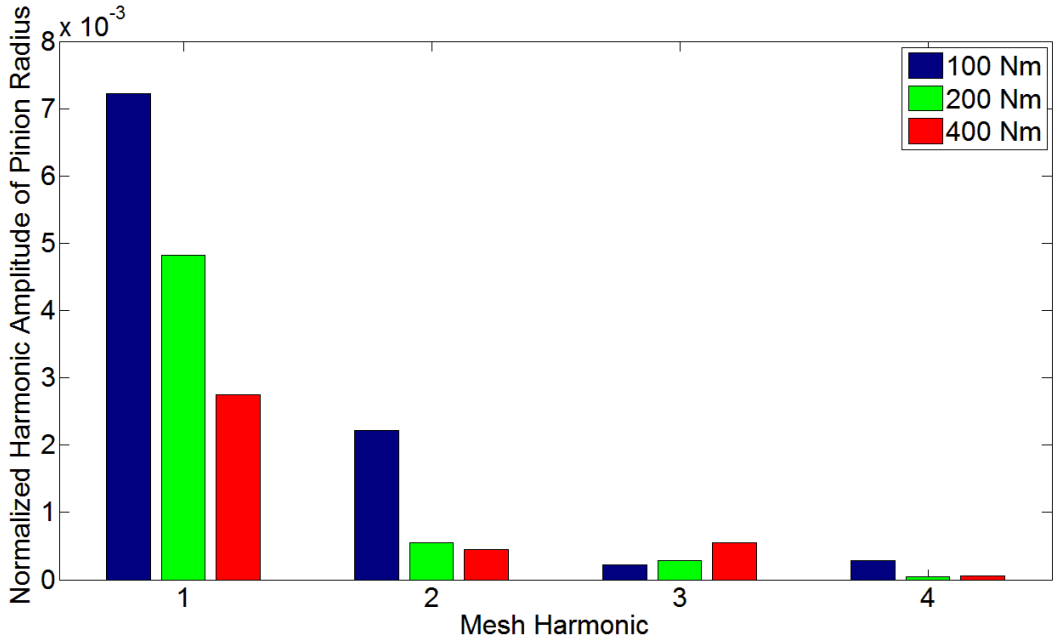

Fig. 3.7 Normalized Harmonic Amplitudes of Pinion Radius for FT

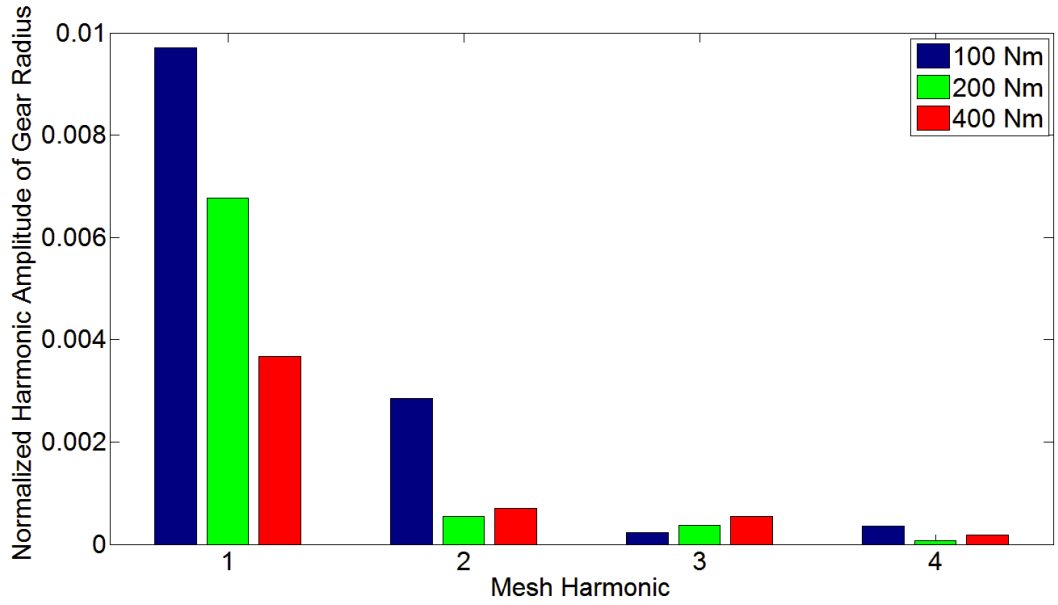

Fig. 3.8 Normalized Harmonic Amplitudes of Gear Radius for FT

Secondly, for spiral bevel gear with profile modification, normalized responses under different load conditions is shown in Fig. 3.9. In this case, the peak behavior of super-harmonic responses are same with that of resonance response during different torque values.

3

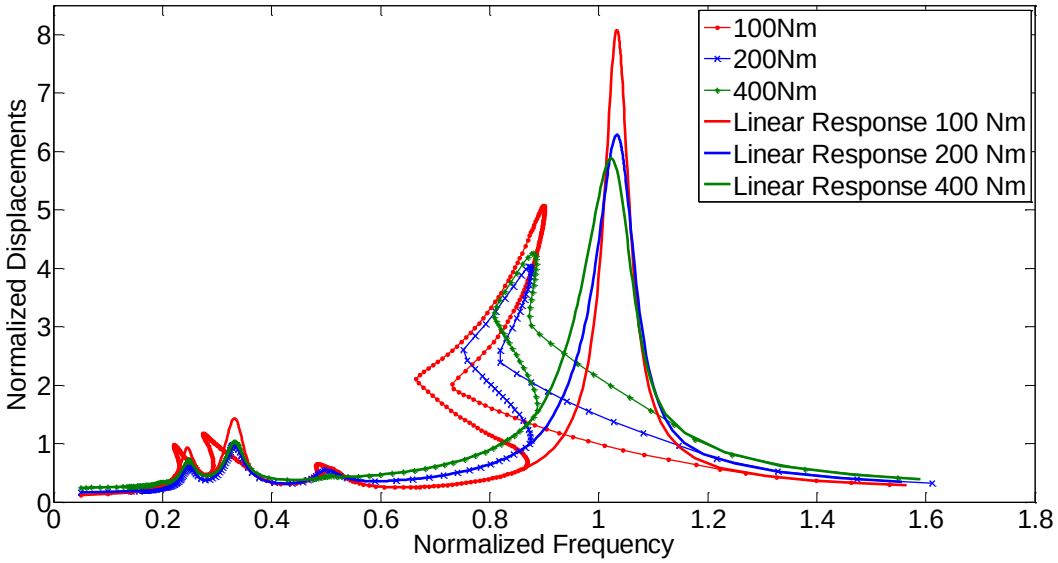

Fig. 3.9 RMS values of dynamic torsional displacements for PF

Fig. 3.10 and Fig. 3.11 show that third mesh harmonic of mesh stiffness and static transmission error affects more than second harmonic of these mesh parameters. In addition to that, third mesh harmonic of mesh stiffness dominates slightly more than first mesh harmonic. The other mesh harmonics of mesh stiffness are also considerably comparable with first and third mesh harmonics especially for light load. Mesh harmonic amplitudes of directional rotation radii for pinion and gear with profile crowning as seen from Fig. 3.12 and Fig. 3.13 are almost twice times than that of the other gear pairs.

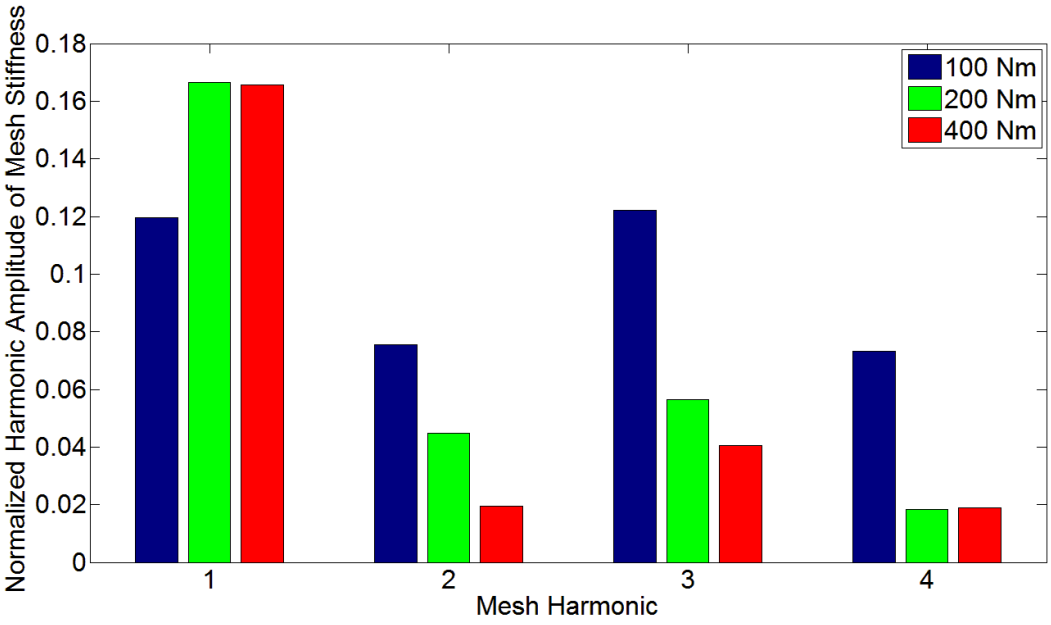

Fig. 3.10 Normalized Harmonic Amplitudes of Mesh Stiffness for PF

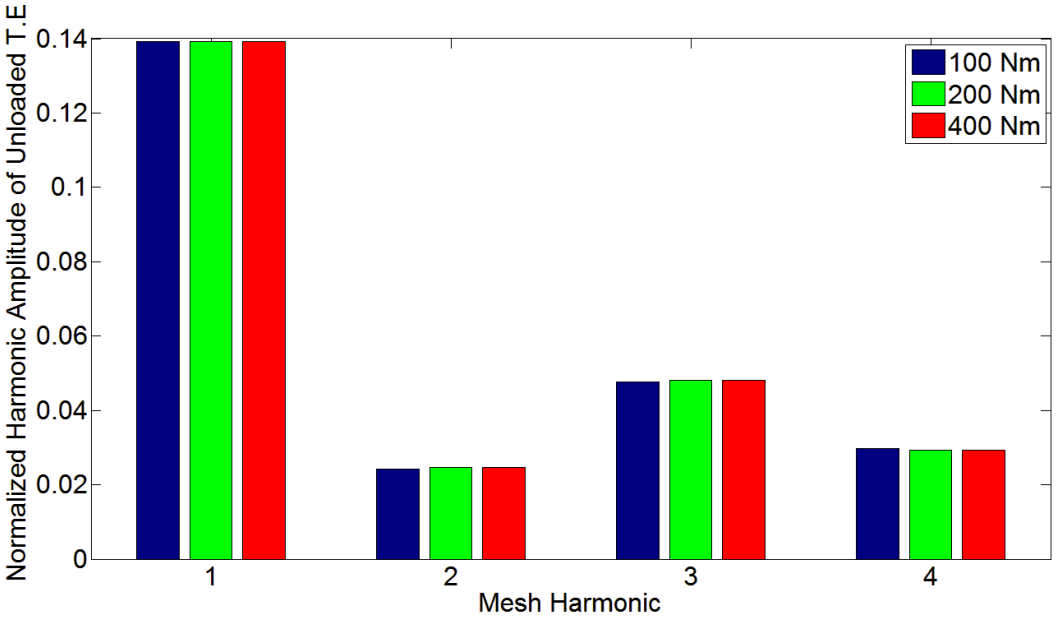

Fig. 3.11 Normalized Harmonic Amplitudes of Unloaded T.E for PF

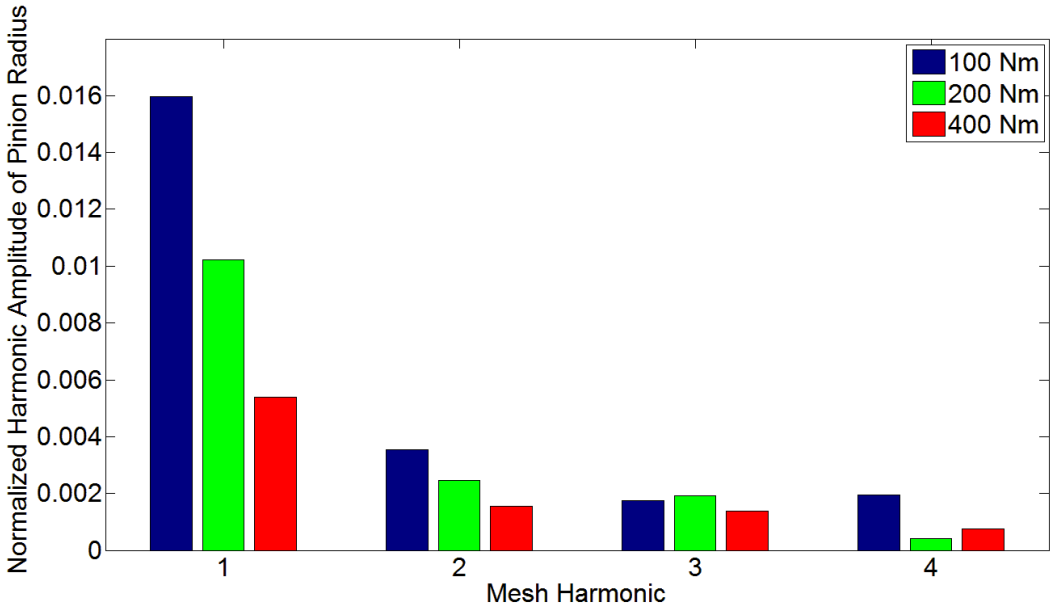

Fig. 3.12 Normalized Harmonic Amplitudes of Pinion Radius for PF

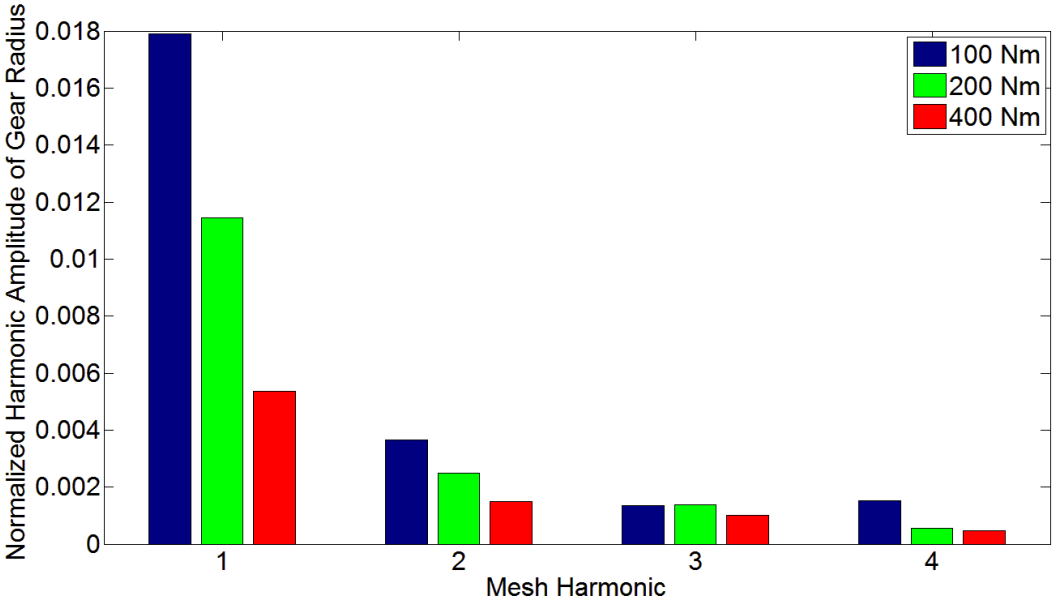

Fig. 3.13 Normalized Harmonic Amplitudes of Gear Radius for PF

Finally, Fig. 3.14 illustrates normalized responses of spiral bevel gear with lengthwise crowning which is close to gear with flank twist in terms of peak behavior of responses and normalized mesh harmonics shown in Fig. 3.15, Fig. 3.16, Fig. 3.17 and Fig. 3.18. Also, peak behavior of response changes for resonance and other super harmonics and effects of first mesh harmonic on mesh parameters are more than that of other harmonic in this type crowning.

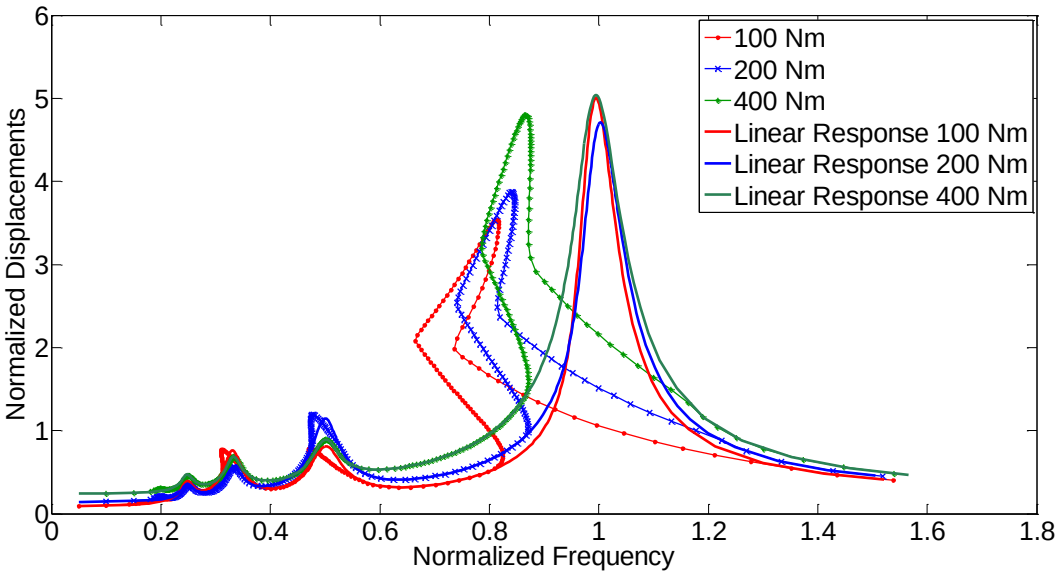

Fig. 3.14 RMS values of dynamic torsional displacements for LW

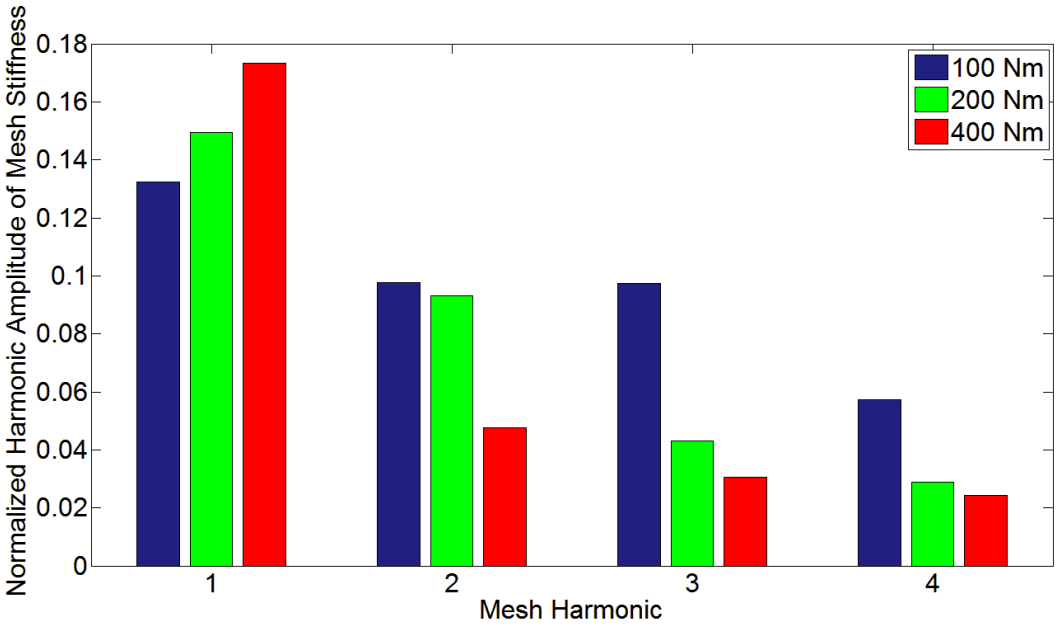

Fig. 3.15 Normalized Harmonic Amplitudes of Mesh Stiffness for LW

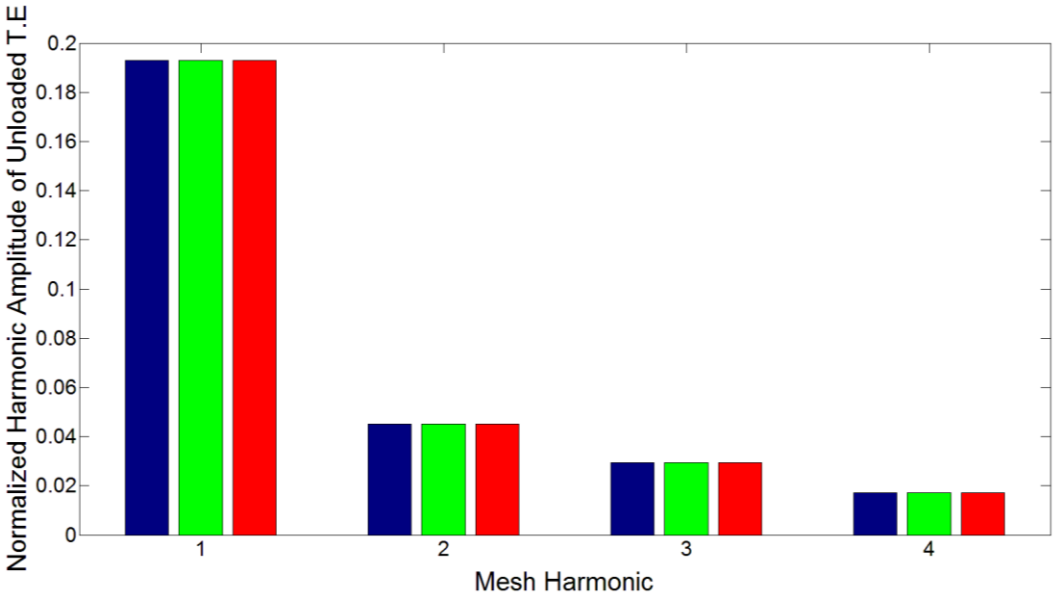

Fig. 3.16 Normalized Harmonic Amplitudes of Unloaded T.E for LW

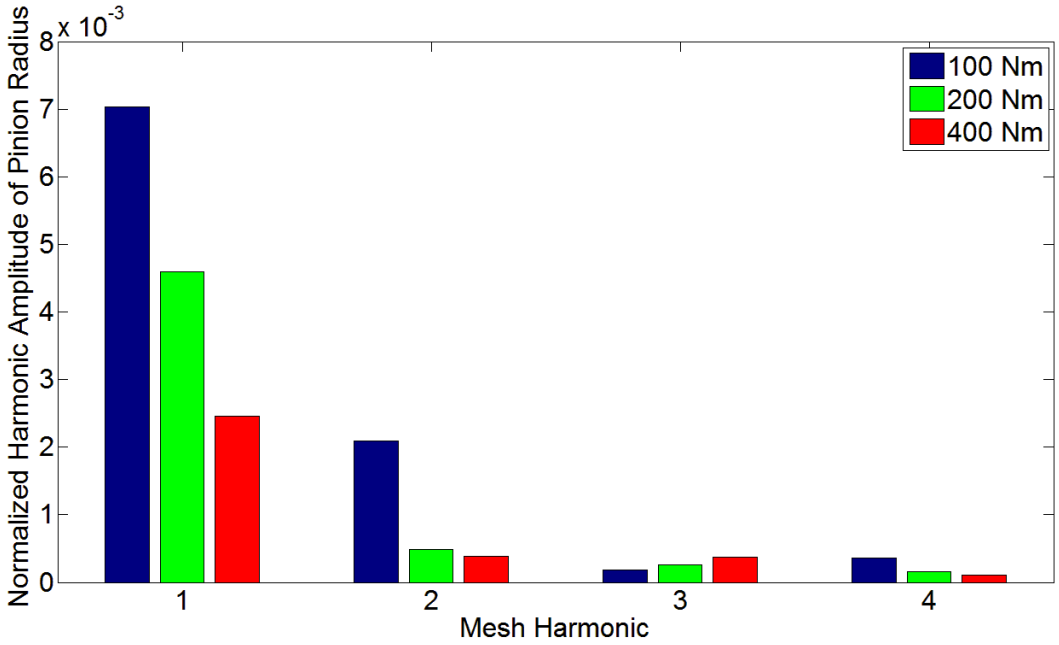

Fig. 3.17 Normalized Harmonic Amplitudes of Pinion Radius for LW

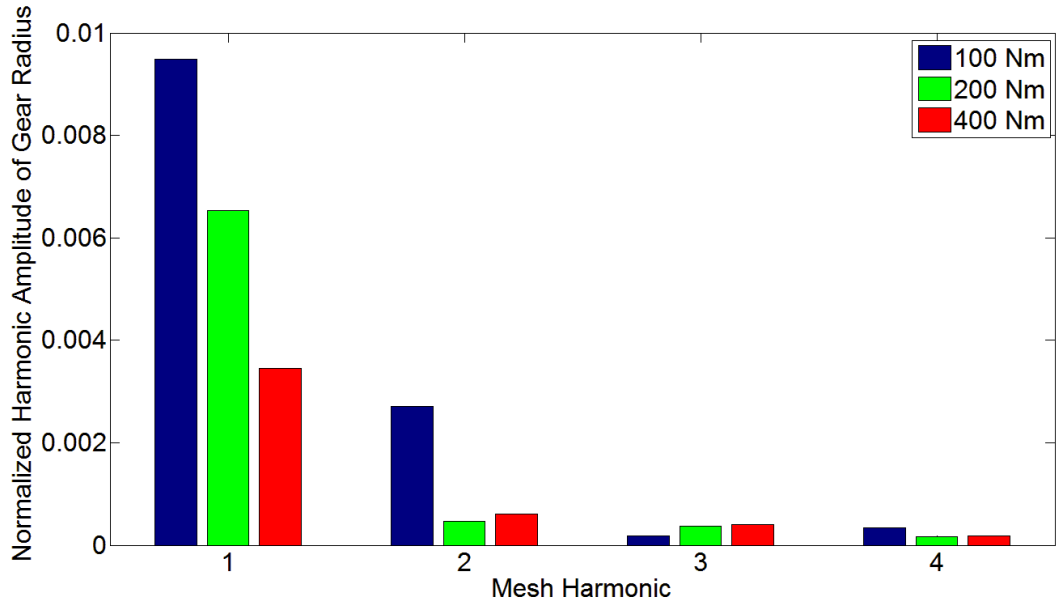

Fig. 3.18 Normalized Harmonic Amplitudes of Gear Radius for LW

Gear pairs with different tooth flank modifications gives a chance to have a better understanding of dynamic displacements with static transmission error and load dependent mesh stiffness. Firstly, different tooth flank modifications results in different translational static transmission error shown in Fig. 3.19. Amplitudes of static transmission error of gear pairs with profile crowning and flank twist are much smaller than that of gear pair with lengthwise crowning.

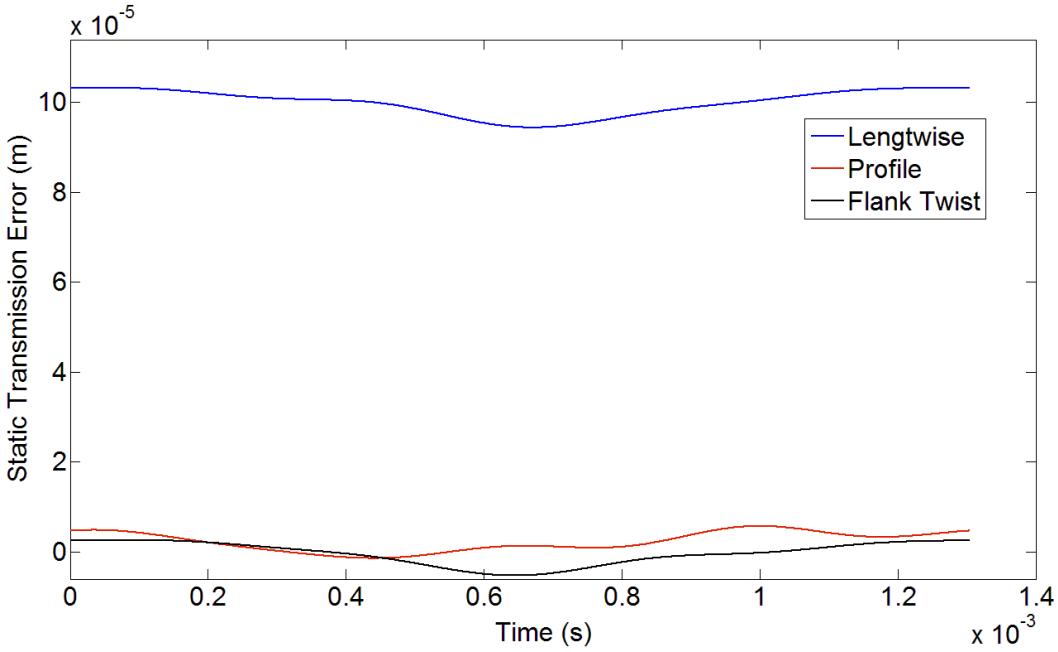

Fig. 3.19 Static transmission errors of gear pairs

Fig. 3.20 shows mesh stiffness variation of gear pairs obtained for lengthwise, profile and flank twist modifications under gear torque of 100 Nm. On the contrary of static transmission error, mesh stiffness variation of gear pair with flank twist is close to that of gear pair with lengthwise crowning and different than that of gear pair with profile crowning.

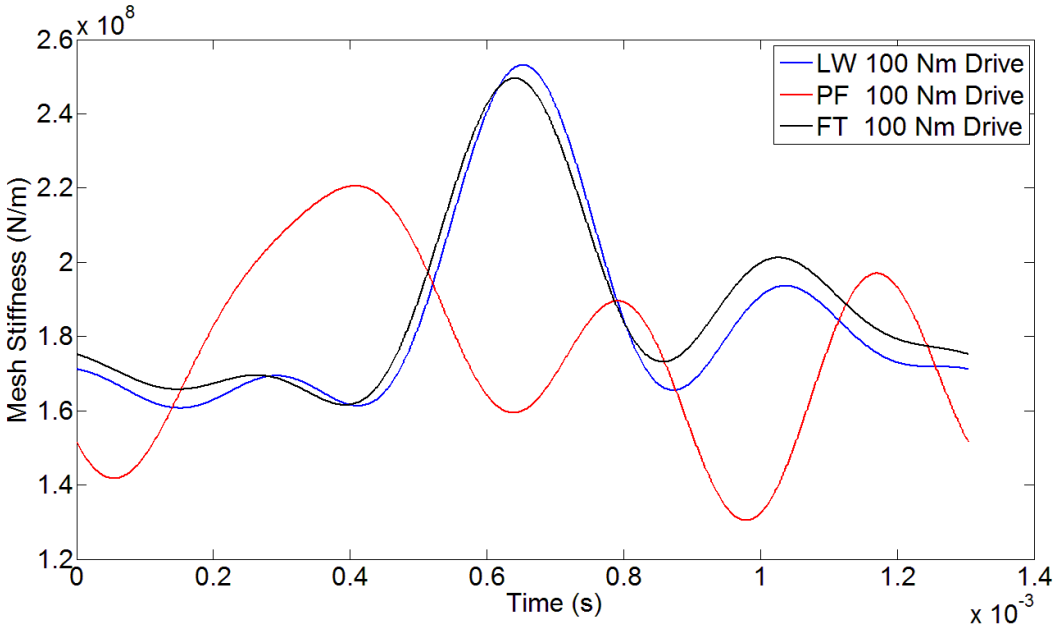

Fig. 3.20 Mesh stiffness variations for gear pairs under light load.

In Fig. 3.21 which shows dynamic displacements of gear pairs with these mesh stiffness variations, the dynamic response of the gear pair with profile crowning differs from those of other gear pairs considerably. Upon further investigation, it is observed that responses of gear pairs with flank twist and lengthwise crowning are slightly different from each other even though static transmission error of these gear pairs are totally different. However, mesh stiffness variations of them are almost same.

Therefore, these two outcomes support that mesh stiffness variation in lightly loaded gear pairs has more effects on dynamic displacements rather than static transmission error.

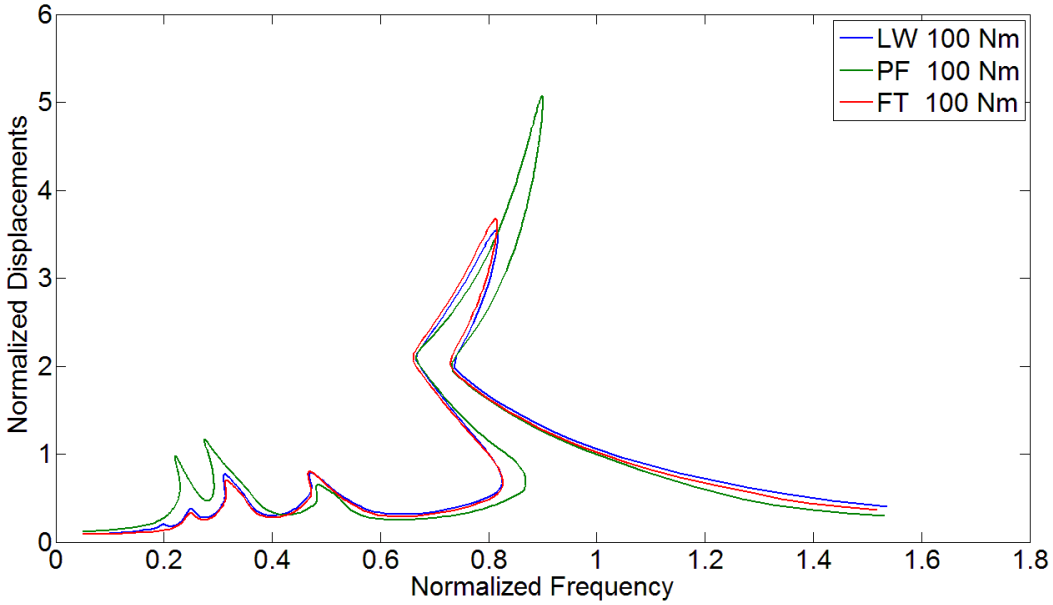

Fig. 3.21 Dynamic Displacements of Gear Pairs with light load.

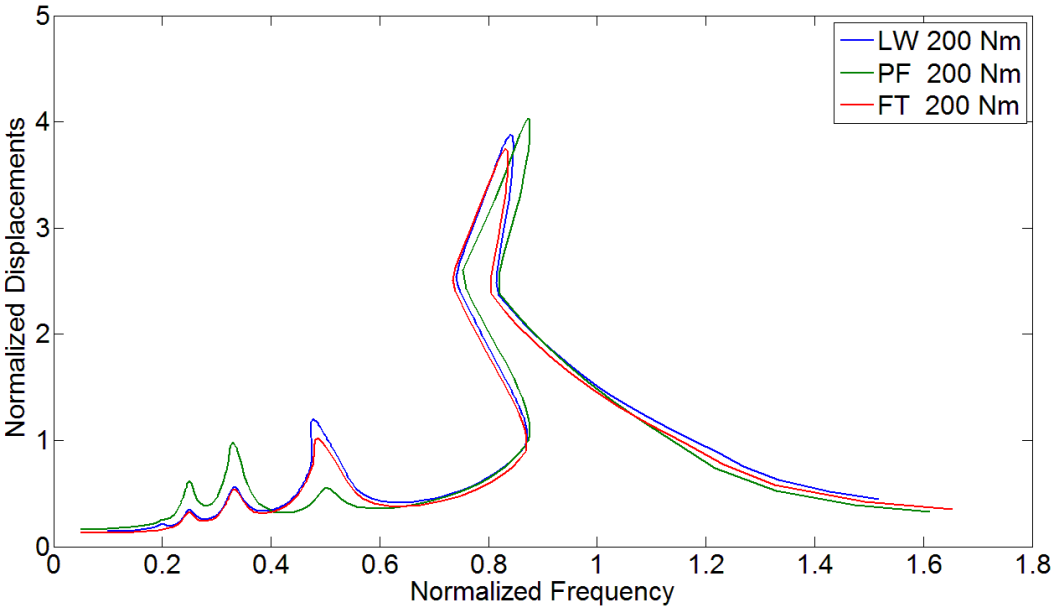

Fig. 3.22 Dynamic Displacements of Gear Pairs with medium load

Effects of mesh stiffness and static transmission error on dynamic displacements change gradually when torque on gear pair increases. Static transmission error starts to be more effective than mesh stiffness variation when gear pairs go through from lightly loaded case to highly loaded case. Responses of gear pair with lengthwise crowning having a large static transmission error increases, while responses of gear pair with profile crowning having large mesh stiffness variation decreases under moderate load as shown in Fig. 3.22. However, mesh stiffness variation is still dominant compared to static transmission error on the response around the primary resonance, 3rd and 4th super-harmonic resonances. When the torque is increased further, gear pair starts to work in heavily loaded condition. For example; for the gear pair given in this study, working condition under torque equal to or larger than 400 Nm can be acceptable as heavily loaded.

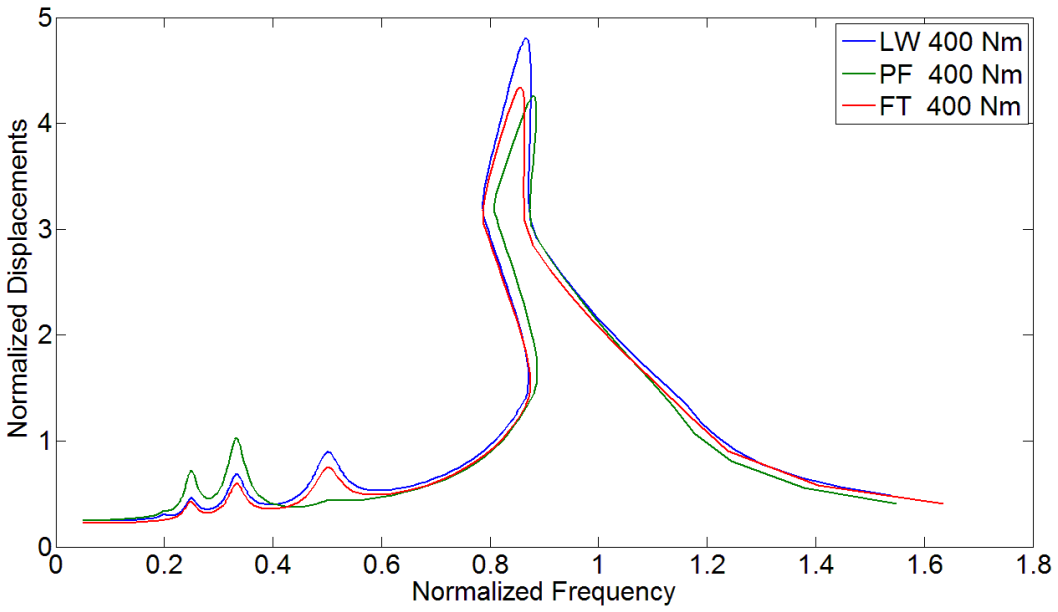

Fig. 3.23 Dynamic Displacements of Gear Pairs with high load

On account of this, dynamic responses for heavily loaded case of gear pairs with tooth flank modifications are shown in Fig. 3.23, in which the peak amplitudes of resonance response are changing between gear pairs with lengthwise and profile crowning when compared to response amplitude under light and moderate load cases. This time, response of gear pair with lengthwise crowning is larger than other gear pairs due to that it has large static transmission error which starts to play a key role on resonance responses of gear pairs.

CHAPTER 4

CONCLUSION AND FUTURE WORK

4.1 Conclusion

The fundamental characteristics of the typical profile crowning, lengthwise crowning and flank twist ease-off topographies are generated in this study for a selected spiral bevel pinion gear pair. The macro and micro geometries are established according to design requirements for generic purposes high load, high speed applications. Macro geometry generation with single indexing and geometry details such as number of teeth, face-width, spiral angle and cutter radius are presented for a given design requirement. Micro geometries are generated in order to obtain gear pairs with profile crowning, lengthwise crowning and flank twist. Corresponding real machine settings of actual tooth for these flank modifications are obtained and basic parameters of machine setting and cutting tool which causing these flank modifications are tabulated. Gear mesh investigations include contact pattern and stress, directional rotation radii, load share, static and loaded transmission errors, and mesh stiffness for drive and coast sides of the tooth. A three-dimensional quasi-static loaded tooth contact analysis is applied to find load distribution and transmission error at each specified time step over a mesh cycle. Then, these mesh parameters used in gear mesh model are calculated. The contact stress at 400Nm is the lowest at the flank twist design. The contact path and directional rotation radius variation of lengthwise crowning and flank twist designs are more stable than the profile modification. The static transmission error and loaded transmission results for profile modification and flank twist are comparable with each other while the lengthwise crowning static transmission error is the

highest. The mesh stiffness magnitude and variation of lengthwise crowning and flank twist modifications are comparable with each other while profile crowning shows a different trend with relatively smaller magnitude. In overall, based on contact path and stress, static and loaded transmission error, mesh stiffness characteristics, flank twist modification is a better selection over the other types.

This thesis is a bridge between kinematics and dynamics of spiral bevel gear pairs. Therefore, nonlinear dynamics of a spiral bevel gear pair with different tooth flank modifications are studied in this paper. Macro geometry of spiral bevel gear pair is generated with face milling and generation motion to prevent failure types such as scoring, tooth breakage and pitting which are seen mostly in helicopter gearboxes. Tooth flanks of gear pairs are modified with real machine settings, which gives actual tooth data with profile crowning, lengthwise crowning and flank twist. In order to get best performance of gearboxes, dynamic characteristic of these gear pairs are taken into consideration by formulating a dynamic model which is composed of a spiral bevel gear pair with a nonlinear time-varying mesh parameters such as stiffness, damping, static transmission along line of action and backlash nonlinearity. These parameters that are used in gear mesh model are obtained by applying a three-dimensional quasi-static loaded tooth contact analysis (LTCA). In order to obtain dynamic displacements in torsional mode, multi-term HBM coupled with discrete Fourier transform (DFT) are applied to solve nonlinear algebraic equations.

As a result of this study, gear pairs with profile crowning, lengthwise crowning and flank twist are analyzed to see effects of modifications on dynamic responses. It is observed that response of gear pairs with profile crowning and lengthwise crowning are more sensitive than flank twist to loading condition. The reasons are that profile crowning and lengthwise crowning causes larger mesh stiffness variation and static transmission error, respectively. Therefore, flank twist can be the best candidate of tooth flank modification in a spiral bevel gear pair used in helicopter gearboxes.

4.2 Future Work

As a future work, transmission drive systems including bevel gears with these flank modifications can be investigated in terms of dynamic behavior in order to find suitable flank modification. Furthermore, parametric studies can be done for optimizing dynamic response of bevel gear pair used in high speed applications such as engine, and helicopter transmission gearboxes. This optimized design can be verified by experimental tests. In terms of mesh model used in this study, friction based on elastohydrodynamic lubrication (EHL) formulation can be combined in order to study the influence of friction on system dynamics. Moreover, mesh damping model can be improved further and the effect of mesh damping on system dynamics can be investigated.

REFERENCES

[1] Gleason Works, “Fundamentals of Bevel Gear Design”

[2] ANSI/AGMA Standard 2005–D03, Design Manual for Bevel Gears

[3] Fong Z, Tsay C., Kinematical Optimization of Spiral Bevel Gears., ASME. J. Mech. Des. 1992;114(3):498-506. doi:10.1115/1.2926578

[4] Krenzer, T. J., Tooth contact analysis of spiral bevel and hypoid gears under load, SAE paper 810688, 1981,

[5] F.L. Litvin, A.G. Wang, R.F. Handschuh, Computerized generation and simulation of meshing and contact of spiral bevel gears with improved geometry, Computer Methods in Applied Mechanics and Engineering, Volume 158, Issues 1–2, 1998, Pages 35-64, doi.org/10.1016/S0045-7825(97)00229-6

[6] Argyris J., Fuentes A., Litvin F.L., Computerized integrated approach for design and stress analysis of spiral bevel gears, Computer Methods in Applied Mechanics and Engineering, Volume 191, Issues 11–12, 2002, Pages 1057-1095, doi.org/10.1016/S0045-7825(01)00316-4

[7] Litvin F.L.,Fuentes A.A., Hayasaka K., Design, manufacture, stress analysis, and experimental tests of low-noise high endurance spiral bevel gears. Mechanism and Machine Theory, v.41, 83-118, 2006, 10.1016/j.mechmachtheory.2005.03.001.

[8] Stadtfeld H.J. . Gaiser U., The Ultimate Motion Graph, J. Mech. Des. 1999, 122(3):317-322, doi:10.1115/1.1286124.

[9] Fong Z.H., Mathematical Model of Universal Hypoid Generator With Supplemental Kinematic Flank Correction Motions, J. Mech. Des. 2000;122(1):136-142. doi:10.1115/1.533552

[10] Wang P.W., Fong Z.H., Fourth-Order Kinematic Synthesis for Face-Milling Spiral Bevel Gears with Modified Radial Motion (MRM) Correction, J. Mech. Des. 2005;128(2):457-467. doi:10.1115/1.2168466.

[11] Fan Q., Computerized Modeling and Simulation of Spiral Bevel and Hypoid Gears Manufactured by Gleason Face Hobbing Process, J. Mech. Des 128(6), 1315-1327 (Dec 24, 2005) (13 pages), doi:10.1115/1.2337316

[12] Fan Q. Enhanced Algorithms of Contact Simulation for Hypoid Gear Drives Produced by Face-Milling and Face-Hobbing Processes. ASME. J. Mech. Des. 2006;129(1):31-37. doi:10.1115/1.2359475

[13] Fan, Q. , Ease-Off and Application in Tooth Contact Analysis for Face-Milled and Face-Hobbed Spiral Bevel and Hypoid Gears. Mechanisms and Machine Science. 34. 321-339. , 2016,. 10.1007/978-3-319-19740-1_15

[14] Artoni A., Bracci A., Gabiccini M. , Guiggiani M., Optimization of the Loaded Contact Pattern in Hypoid Gears by Automatic Topography Modification, J. Mech. Des. 2008;131(1):011008-011008-9, doi:10.1115/1.3013844.

[15] Gabiccini M., Bracci A., Guiggiani M., Robust Optimization of the Loaded Contact Pattern in Hypoid Gears with Uncertain Misalignments, J. Mech. Des. 2010;132(4):041010-041010-8, doi:10.1115/1.4001485.

[16] Artoni A., Kolivand M., Kahraman A., An Ease-Off Based Optimization of the Loaded Transmission Error of Hypoid Gears, J. Mech. Des. 2009;132(1):011010-011010-9. doi:10.1115/1.4000645

[17] Kolivand M., Kahraman A., A load distribution model for hypoid gears using ease-off topography and shell theory. Mechanism and Machine Theory. 2009, v.44, pages 1848-1865, 10.1016/j.mechmachtheory.2009.03.009.

[18] Fan Q., DaFoe R.S., Swanger J.W., Higher-Order Tooth Flank Form Error Correction for Face-Milled Spiral Bevel and Hypoid Gears. ASME. J. Mech. Des. 2008;130(7):072601-072601-7. doi:10.1115/1.2898878

[19] Zhou Z., Tang J., Ding H., Accurate modification methodology of universal machine tool settings for spiral bevel and hypoid gears, Proceedings of the Institution of Mechanical Engineers, Part B: Journal of Engineering Manufacture, Vol 232, Issue 2, pp. 339 - 349, doi.org/10.1177/0954405416640173

[20] Ding H., Tang J., Zhong J., Accurate nonlinear modeling and computing of grinding machine settings modification considering spatial geometric errors for hypoid gears, Mechanism and Machine Theory, Volume 99, 2016, Pages 155-175, https://doi.org/10.1016/j.mechmachtheory.2016.01.008.

[21] Ding H., Zhou Y., Tang J., Zhong J., Zhou Z., Wan G., A novel operation approach to determine initial contact point for tooth contact analysis with errors of spiral bevel and hypoid gears, Mechanism and Machine Theory, Volume 109, 2017, Pages 155-170, doi.org/10.1016/j.mechmachtheory.2016.11.007

[22] Simon V.V., Influence of tooth modifications on tooth contact in face-hobbed spiral bevel gears. Mechanism and Machine Theory, 2011, v46., Pages 1980-1998. 10.1016/j.mechmachtheory.2011.05.002.

[23] Simon V.V., Influence of machine tool setting parameters on EHD lubrication in hypoid gears. Mechanism and Machine Theory (2009), 44. 923-937. 10.1016/j.mechmachtheory.2008.06.005

[24] Gosselin C.C., Gagnon P.P., Cloutier L.L. Accurate Tooth Stiffness of Spiral Bevel Gear Teeth by the Finite Strip Method. ASME. J. Mech. Des. 1998;120(4):599-605. doi:10.1115/1.2829321

[25] Cheng Y, Lim T.C., Dynamics of Hypoid Gear Transmission with Nonlinear Time-Varying Mesh Characteristics, ASME. J. Mech. Des., 2003; 125(2):373-382. doi:10.1115/1.1564064

[26] Wang, J., Lim, T. C., and Li, M., 2007, "Dynamics of a hypoid gear pair considering the effects of time-varying mesh parameters and backlash nonlinearity," J. Sound Vib., 308, pp. 302–329.

[27] Wang, J., Lim, T.C.: Effect of tooth mesh stiffness asymmetric nonlinearity for drive and coast sides on hypoid gear dynamics. J. Sound Vib. 319, 885–903 (2009)

[28] Yang, J., Peng, T., and Lim, T. C., 2011, "An enhanced multi-term harmonic balance solution for nonlinear period-one dynamic motions in right-angle gear pairs," Nonlinear Dyn., 67(2), pp. 1053–1065.

[29] Yavuz, S. D., Saribay, Z. B., and Cigeroglu, E., 2017, "Nonlinear Dynamic Analysis of a Spiral Bevel Geared System", Proceedings 35th IMAC, A Conference and Exposition on Structural Dynamics, Garden Grove, LA, USA.

[30] Yavuz, S. D., Saribay, Z. B., and Cigeroglu, E., 2018, "Nonlinear time-varying dynamic analysis of a spiral bevel geared system", Nonlinear Dyn., 92(4), pp. 1901-1919, doi:https://doi.org/10.1007/s11071-018-4170-9

[31] Gleason Works, Understanding tooth contact analysis, Gleason Works Publication SD. 3139B, 1981

[32] Vijayakar, S., Contact analysis program package: Calyx, Advanced Numerical Solutions.

[33] Stadtfeld, H.J. Good Basic Design or Sophisticated Flank Optimizations? Each at the Right Time, Gear Technology, Jan/Feb 2005, Randall Publishing Inc., Elk Grove Village, Illinois

[34] Peng, T., Coupled Multi-body Dynamic and Vibration Analysis of Hypoid and Bevel Geared Rotor System. Dissertation, University of Cincinnati, 2010,

[35] Yavuz, S. D., Saribay, Z. B., and Cigeroglu, E., 2016, "Nonlinear Time-Varying Dynamic Analysis of a Multi-Mesh Spur Gear Train," Proceedings 34th

IMAC, A Conference and Exposition on Structural Dynamics, Orlando, Florida, USA.

[36] Cigeroglu, E., and Samandari, H., 2012, "Nonlinear free vibration of double walled carbon nanotubes by using describing function method with multiple trial functions," Phys. E Low-dimensional Syst. Nanostructures, 46, pp. 160–173.

[37] Yümer, M. E., Ciğeroglu, E., and Özgüven, H. N., 2010, "Non-linear Forced Response Analysis of Mistuned Bladed Disk Assemblies," Proceedings of ASME Turbo Expo 2010: Power for Land, Sea and Air, Glascow, UK.

[38] Von Groll, G., and Ewins, D. J., 2001, "The Harmonic Balance Method With Arc-Length Continuation in Rotor/Stator Contact Problems," J. Sound Vib., 241(2), pp. 223–233.

[39] Kahraman, A., and Blankenship, G. W., 1995, "Steady state forced response of a mechanical oscillator with combined parametric excitation and clearance type non-linearity," J. Sound Vib., 185(5), pp. 743–765.

[40] Cardona, A., Lerusse, A., and Ge, M., 1998, "Fast Fourier nonlinear vibration analysis," 22.